Shape Memory and Superelasticity (2021) 7:109–165
https://doi.org/10.1007/s40830-020-00306-x

TECHNICAL ARTICLE

Processing and Scalability of NiTiHf High-Temperature Shape Memory Alloys

O. Benafan[1] · G. S. Bigelow[1] · A. Garg[1,2] · R. D. Noebe[1] · D. J. Gaydosh[3] · R. B. Rogers[1]

Received: 26 August 2020 / Revised: 21 November 2020 / Accepted: 23 November 2020 / Published online: 9 February 2021

Abstract

Development of melting and processing techniques for NiTiHf high-temperature shape memory alloys at the laboratory scale has resulted in pronounced success and repeatability for actuation purposes. Even the Ni-rich NiTiHf formulations, which are more challenging from a compositional control standpoint since small changes in chemistry can result in large transformation temperature variations, are reproducibly processed at the laboratory scale. Since properties of the slightly Ni-rich NiTiHf alloys have proved promising, large-scale production of such alloys now requires renewed attention. In this work, several melting techniques were used to process NiTi-20Hf (at.%), ranging from vacuum induction melting to plasma arc melting, with heats ranging in size from 0.4 to 250 kg with a target composition of $Ni_{50.3}Ti_{29.7}Hf_{20}$ (at.%). All cast ingots were subsequently hot extruded into bar. The resulting chemistries, microstructures, and inclusion types and sizes were evaluated as a function of melting technique. Finally, the thermophysical, mechanical and functional properties were measured for a number of material heats that varied in size and primary processing technique. The results indicated that various melting techniques could result in alloys with slightly different end compositions that can affect the mechanical and functional properties. Some of the compositional changes are inherent to the melting process, such as formation of carbides, Ni loss, and other attributes that can be adjusted or minimized by optimizing melting practices. Finally, alloy properties were correlated to the actual compositions of each heat, through corrections based on differential scanning calorimetry measurements, indicating that most scatter in properties can be explained by slight chemistry variations.

Keywords NiTiHf · High-temperature shape memory alloy · Martensitic transformation · H-phase · Actuation · Melt processing

Introduction

Since their discovery in the early 1990s, NiTiHf shape memory alloys (SMAs) have been broadly investigated. The foremost characteristic, relatively high martensitic transformation temperatures (> 100 °C), has been the impetus behind the persistent development of these alloys, primarily as a lower cost alternative to NiTiPt, NiTiPd or NiTiAu counterparts [1]. It is generally accepted that the higher transformation temperatures make NiTiHf alloys particularly relevant to aerospace, automotive, and energy fields, among others. In aerospace, these active materials can meet the increasing demands of reducing system weight, improving fuel efficiency and structural adaptability without adversely affecting performance or safety of the operation [2, 3]. In addition to their high-temperature capability, these materials can also generate very high energy densities in excess of 30 J/cm^3 [4]. Moreover, given that the material itself is the fundamental actuation element (i.e., the material changes shape in response to heat), compact actuation forms can be realized, permitting new design concepts unattainable via conventional methods [5].

Although the advantageous properties and end applications may seem obvious, selecting the precise alloy for a specific application is not. As with most SMAs, alloy chemistry plays a predominant role in influencing the martensitic transformation and shape memory properties. The initial focus on NiTiHf alloys was targeted toward Ti(Hf)-rich

✉ O. Benafan
othmane.benafan@nasa.gov

[1] Materials and Structures Division, NASA Glenn Research Center, Cleveland, OH 44135, USA

[2] University of Toledo, Toledo, OH 43606, USA

[3] Ohio Aerospace Institute, Cleveland, OH 44142, USA

formulations, due to manageable control over composition with low transformation temperature sensitivity to small chemistry changes. These formulations resulted in maximum transformation temperatures near 600 °C [6], showing for the first time the potential of the Hf elemental addition in raising martensitic transformation temperatures. However, with this transformation temperature improvement came other challenges, such as poor mechanical strength (e.g., lack of ductility and low critical resolved shear stress) and very poor functional stability (e.g., significant accumulation of plastic deformation during thermal or stress-induced transformation) [7–9]. As a result, the Ti(Hf)-rich alloys suffer from large dimensional/thermal stability issues, making them impractical for any actuator application where repeatability and durability are required.

The Ni-rich counterpart, in contrast, is more sensitive to chemistry changes, but offers a powerful mechanism to strengthen the matrix and improve the mechanical strength and functional stability [10]. Precipitation strengthening has been shown to be an effective method for improving the shape memory properties of the Ni-rich NiTiHf alloys [11–13]. The nucleation of nanoscale precipitates, termed the H-phase [14–16], improves the yield strength and the shape memory behavior [13]. While there is minimal effect from precipitation reported for the Ti-rich NiTiHf alloys [17], the H-phase precipitation in a Ni-rich matrix is used to tune the transformation temperatures by removing excess Ni (or regulating the overall Ni content within the matrix) during aging at different times and temperatures [18–20].

Based on this latter realization, Ni-rich formulations have become the focus of research and development pertinent to high-temperature NiTiHf SMAs. Among several compositions studied, the $Ni_{50.3}Ti_{29.7}Hf_{20}$ (at.%) formulation is a widely examined alloy exhibiting transformation temperatures > 150 °C and transformation strains of ~ 2, 4, and 6% in compression, tension, and torsion, respectively [11, 12, 18, 19, 21, 22]. This alloy was also shown to withstand high stresses (> 1 GPa) with fully reversible deformation [23] and to generate extremely high forces in excess of 1.3 GPa (during constrained transformation) [24]. It has been successfully used in a number of prototype components in the form of torque tubes as part of the NASA Spanwise Adaptive Wing project [2, 25], and in the form of expansion elements as part of the static rock breaker [24]. A low-temperature variant of this alloy was also successfully validated on Boeing's 2019 EcoDemonstrator program as the driving force in SMA-actuated vortex generators [3].

Initial development of melting and processing techniques for NiTiHf at a small, laboratory scale (small vacuum induction melts and arc-melted buttons of < 1 kg) resulted in pronounced success and repeatability for actuation purposes. Based on these positive results, larger melts were pursued, with melt size progressing from a few kilograms to heats of > 30 kg. However, while properties of the Ni-rich NiTiHf alloys proved promising, larger scale production of such alloys required additional effort. Transition to larger production runs entails several challenges, ranging from cost, processability, and manufacturability to recycling and supply chain logistics. In order for this material to become a commodity, these challenges must be addressed.

Thus, the goal of this work was to evaluate the scale-up potential of the $Ni_{50.3}Ti_{29.7}Hf_{20}$ (at.%) target composition. Several melting techniques were used, including various forms of vacuum induction melting and plasma arc melting, with heat sizes ranging from 0.4 to > 250 kg. Multiple heats were produced using different suppliers to assess heat-to-heat variability and the effect of the various melting practices. Microstructural characteristics such as phase structure, grain size, precipitates, and inclusions were evaluated using optical and electron microscopy, and X-ray diffraction (XRD), while metallic composition and impurities were determined by inductively coupled plasma atomic emission spectrometry (ICP-AES). Mechanical and functional behavior were determined using differential scanning calorimetry (DSC), hardness measurements, isothermal mechanical testing, and uniaxial constant force thermal cycling (UCFTC).

Melting, Processing and Experimental Methods

Melting Methods

The $Ni_{50.3}Ti_{29.7}Hf_{20}$ (at.%) alloy was the target composition in this study across all heats and melt sizes (except alloy H11, which will be discussed later). The NASA Glenn Research Center Materials Processing Laboratory (MPL), and four commercial vendors were used to produce heats of the target alloy. Altogether, six different melting processes were used. These consisted of vacuum induction melting (VIM), vacuum induction skull melting (VISM), and combinations including VIM plus vacuum arc remelting (VAR), VISM plus VAR, and plasma arc melting (PAM) plus VAR. Table 1 illustrates the typical heat sizes along with the starting purity of the elemental components of Ni, Ti, and Hf (along with inherent residual Zr, which is an unavoidable impurity in Hf). The perceptible variation in the starting material purity is deliberate, as no qualifications were provided on the level of purity or the starting form (e.g., pellets, sponge, electrolytic crystal bars, etc.). Zr is present because Hf is the major by-product of Zr refining. Based on current research, it is not believed that Zr presents any issues and in nearly all respects acts the same as Hf when alloyed with NiTi. However, for completeness we track the level of Zr in each alloy. Other trace constituents were present but not

Table 1 Processing specifications including melting technique, heat size, and elemental purity of starting Ni, Ti, and Hf (with residual Zr level in the Hf starting material)

No. of process	Process type	Heat size (kg)	Purity (%)		
			Ni	Ti	Hf (Zr)[a]
1	VIM	0.4	99.995	99.995	99.9 (0.7)
2	VISM	27.2			> 99.5 (0.19)
3	VISM + VAR	54.4			99 (< 1)
4	VIM + VAR	18.1	99.988	99.6	99.9 (0.19)
5	PAM + VAR	250	99.997	99.7	99 (< 1)

The melting processes are vacuum induction melting (VIM), vacuum induction skull melting (VISM), VISM plus vacuum arc remelting (VAR), VIM plus VAR, and plasma arc melting (PAM) plus VAR

[a]Purity not including residual Zr, which is included in the parentheses

detailed here due to their very low percentages, less than a few hundred ppm.

In this work, VIM was performed in a vacuum furnace with an inductively heated graphite crucible under a partial pressure of argon. The molten metal was poured into cylindrical molds with a hot top to ensure metal flow and avoid shrinkage pipes within the castings.

VISM was performed using a segmented water-cooled copper hearth. In addition to heating, the induction coils were also used for stirring the molten metal to yield homogenous castings, particularly for the dense Hf. The very first heats were produced without an existing skull; "skull" refers to a thin layer of metal that remains frozen against the bottom and walls of the crucible. The following heats were created using the skull from previous melts. Having an equilibrated skull at the beginning of a melt reduces segregation of elements (especially high density elements like Hf) to the skull by promoting better thermal insulation from the cooling effect of the crucible and ultimately achieving a more uniform temperature distribution throughout the melt. Also, because the skull is already equilibrated, any interaction of the melt with the skull will not result in a change in chemistry. This is critical for the NiTiHf alloys since any deviation in Ni content can change the resulting transformation temperatures and mechanical properties, and the dense Hf pieces can travel to the bottom of the crucible and solidify, resulting in a Hf-lean ingot composition. Another important aspect of the NiTiHf VISM was the modification of the gaps between the copper fingers. The gap-filling dielectric material was a source of ceramic contamination for the initial heats, which was then changed to graphite to mitigate the contamination. Finally, the molten metal was poured into steel molds of varying diameters.

PAM was performed using a helium plasma torch system. The torch was directed at the elemental NiTiHf compacts, which were placed on a water-cooled, copper hearth using a feed system. The first compact melt included a sacrificial run to produce a skull for the successive melts. The next compact was then melted and poured into a copper mold mounted on a withdrawal mechanism. This process was repeated by melting one compact at a time and pouring it into the mold along with progressively withdrawing the solidified ingot (the top of the ingot in the mold was reheated/melted before pouring). The ingot was fully formed after all the compacts were melted and poured in series into the mold. Given the size of the target PAM melt (> 250 kg), the PAM melt was produced as two separate ingots. VAR was used in this work as a secondary meting process after VIM, VISM, and PAM to further promote homogeneity or combine multiple ingots. It should be noted that throughout the melting process, the ingots were tested for baseline chemistry and transformation temperatures.

Secondary Processing Techniques

Homogenization

Prior to any hot working, as-cast ingots were homogenized in vacuum at 1050 °C. The VIM and VISM ingots were homogenized for 72 h, while the PAM + VAR heats were homogenized for 120 h due to the much larger ingot size (see Table 2). This step was essential to remove potential chemical inhomogeneity and circumvent, or at least reduce, likely segregation. The homogenization treatment temperature was chosen below the solidus temperature (approx. 1230 °C) to avoid any incipient melting and to preserve the casting's shape.

After homogenization, as-cast ingots were surface cleaned and prepared for extrusion by canning/packing in mild steel containers. The ingots were then hot extruded at temperatures between 900 and 1015 °C with varying reduction ratios, as summarized in Table 2. Finally, steel cans were removed by acid pickling or machining and the resulting bars were subject to centerless grinding and straightening to a final diameter.

Machined specimens were characterized in the as-extruded and aged conditions. Aging was accomplished at 550 °C for 3 h under argon, followed by air cooling. This aging heat treatment was selected based on prior work that provided the best overall thermomechanical properties [11–13].

Hot Working (Extrusion)

Hot working in this study was performed using a direct hot extrusion process. Homogenized billets of various weights and sizes (Fig. 1a, b) were surface cleaned, the nose chamfered, and placed into mild steel cans, which were then evacuated and sealed. The assembled billet was then heated

Table 2 Alloy identification and process parameters including heat sizes, dimensions of the ingot before and after extrusion, and other processing details such as heat treatments and extrusion conditions

No. of process	Images (before extrusion)	Process type	No. of heat	Heat size kg (lbs)	Initial diameter cm (in)	Final diameter cm (in)	Processing parameters
1		VIM	H1 H2	0.4 (0.9)	2.54 (1)	1.016 (0.4)	VIM: Graphite crucible Mold: Copper with conical hot top section Homogenization: 1050 °C/72 h/FC Extrusion: steel can, 900 °C
2		VISM	H3 H4 H5 H6 H7 H8 H9 H10 H11	27.2 (60)	3.048 (1.2)	1.016 (0.4)	VISM: Water-cooled copper hearth Mold: Steel Homogenization: 1050 °C/72 h/FC Extrusion: steel can, 930 °C
3		VISM + VAR	H12 H13 H14	54.4 (120)	17.018 (6.7) 6.35 (2.5)	Pass 1: 8.382 (3.3) Pass 2: 2.79 (1.1) Pass 3: 1.016 (0.4) 1.016 (0.4)	VISM: Water-cooled copper hearth VAR: Copper mold Homogenization: 1050 °C/72 h/FC Extrusion: steel can, 920 °C
4		VIM + VAR	H15 H16	18.1 (40)	10.16 (4)	Pass 1: 2.794 (1.1) Pass 2: 1.016 (0.4)	VIM: Graphite Crucible VAR: Copper mold Homogenization: 1050 °C/72 h/Ar quench Extrusion: steel can, 933 °C
5		PAM + VAR	H17 H18	250 (551)	22.86 (9) 29.972 (11.8)	Pass 1: 17.526 (6.9) Pass 2: 1.016 (0.4) Pass 1: 14.986 (5.9) Pass 2: 6.604 (2.6) Pass 3: 2.857 (1.125) Pass 4: 1.27 (0.5)	PAM: Water-cooled copper hearth VAR: Copper mold Homogenization: 1050 °C/120 h/FC Extrusion: steel can, 1015 °C PAM: Water-cooled copper hearth VAR: Copper mold Homogenization: 1050 °C/120 h/FC Extrusion: steel can, 912–952 °C

The process types are (1) vacuum induction melting (VIM), (2) vacuum induction skull melting (VISM), (3) VISM + vacuum arc remelting (VAR), (4) VIM + VAR, and (5) plasma arc melting (PAM) + VAR

FC furnace cooled to room temperature

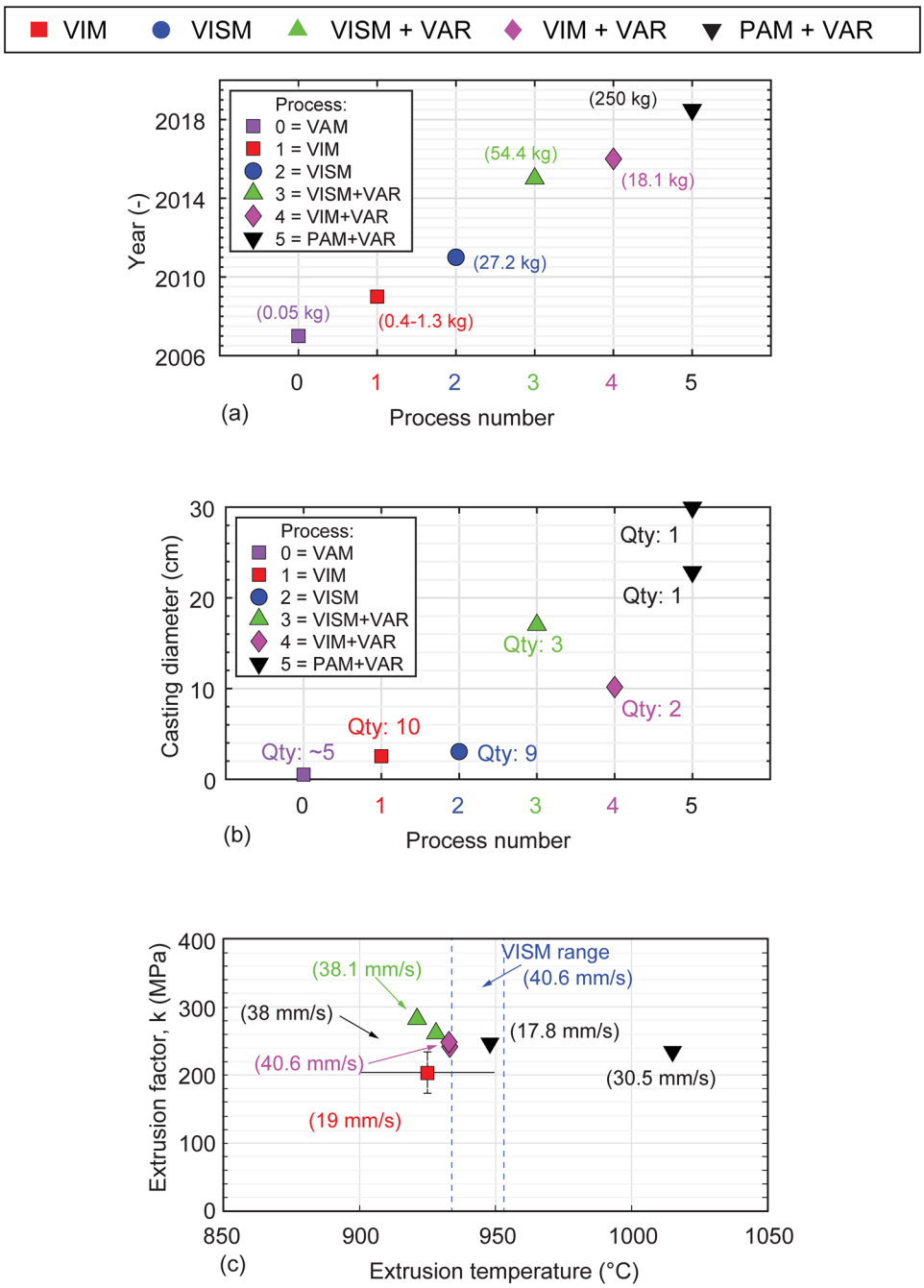

Fig. 1 Hot extrusion parameters for the NiTiHf alloy showing **a** ingot sizes and development year, **b** casting diameters and quantities of castings investigated, and **c** extrusion parameters including extrusion temperature, ram speed, and extrusion factors. The process types are *1* vacuum induction melting (VIM *filled red square*), *2* vacuum induction skull melting (VISM *filled blue circle*), *3* vacuum induction skull melting + vacuum arc remelting (VISM + VAR *filled green triangle*), *4* VIM + VAR *filled pink diamond*, and *5* plasma arc melting + vacuum arc remelting (PAM + VAR *filled inverted black triangle*) (Color figure online)

and soaked in a furnace at a given extrusion temperature, shown in Fig. 1c. Given that the approximate melting point of these alloys is expected to be between 1200 and 1300 °C, extrusion temperatures were selected to be greater than 60% of the melting point, as commonly practiced in metal extrusion processes [26]. Moreover, binary NiTi and NiTiHf have been routinely extruded at temperatures between 900 and 1050 °C [11, 13, 18, 27], and this was used as a starting baseline in this work.

Once at temperature for sufficient time, the canned billet was removed from the furnace and immediately lubricated using graphite and glass-based lubricants. The billet was rolled over a bed of powdered glass and then placed on the preheated container for extrusion, and the die stack was lubricated using graphite. The combined canning and lubrication proved to be very essential in hot working these alloys. Canning was primarily used to maintain core material temperature once transferred from the furnace to the press, to provide a thermal barrier from die-chilling effects during extrusion, and to reduce oxidation of the NiTiHf material during heating prior to extrusion. The softer can material and the glass also provided lubrication and reduced friction

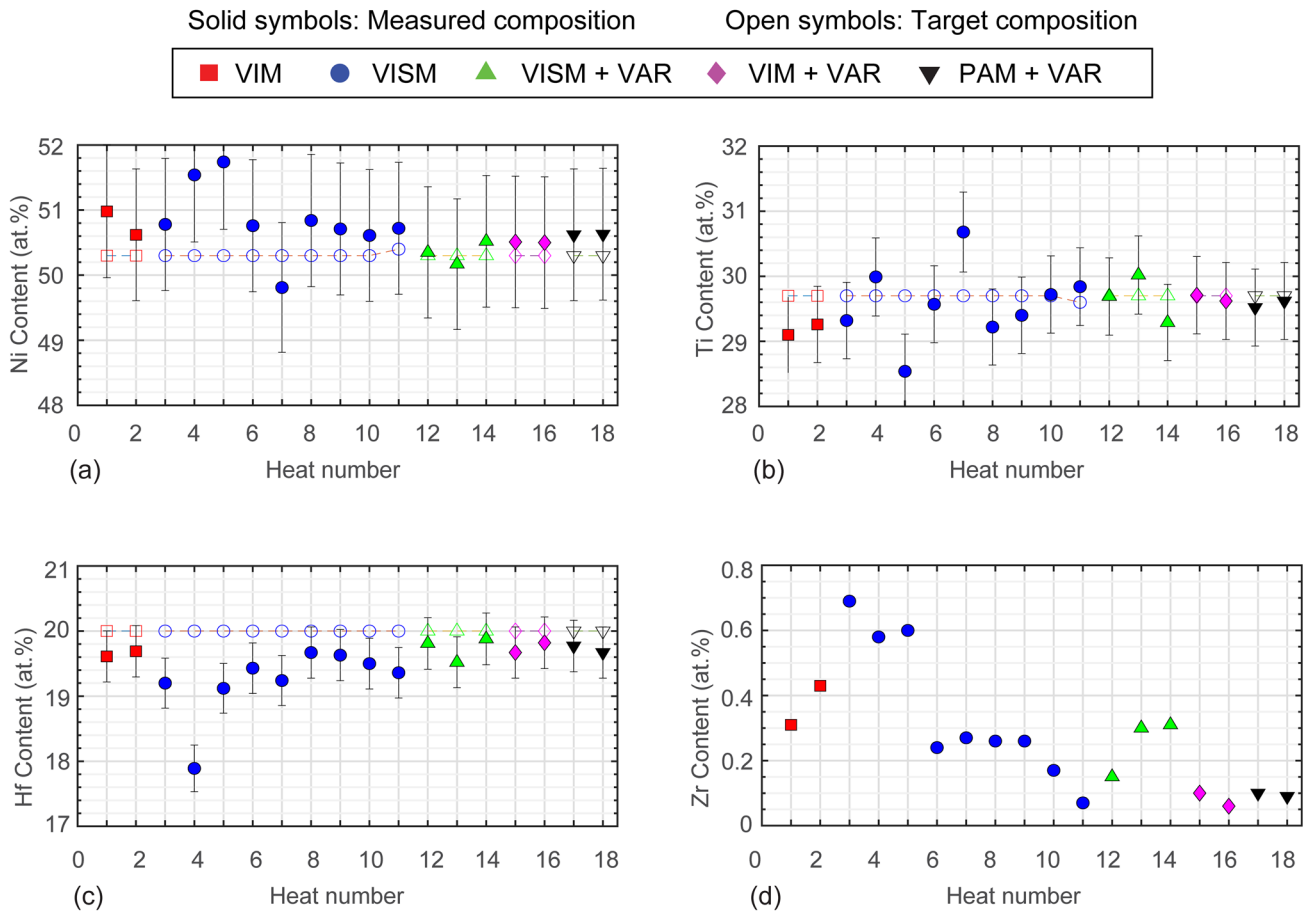

Fig. 2 Chemical compositions determined by the ICP method for **a** nickel, **b** titanium, **c** hafnium and **d** zirconium in the bulk castings. The target compositions are shown by the "*open*" symbols, and the actual measurements are shown by the *solid* symbols. The process types are *1* vacuum induction melting (VIM), *2* vacuum induction skull melting (VISM), *3* vacuum induction skull melting + vacuum arc remelting (VISM + VAR), *4* VIM + VAR, and *5* plasma arc melting + vacuum arc remelting (PAM + VAR)

when in contact with the die. In addition, glass plays an important role in insulating the billet from the tooling, hence maintaining better temperature control.

The canned and lubricated billet was then upset and extruded with the proper ram force and speed, set according to the billet size and material as shown in Fig. 1c. The listed extrusion factors, which are a function of reduction ratio, ram force, and friction, are in line with the factors used to extrude binary NiTi, mainly in the 230–280 MPa range [28]. Depending on the starting billet diameters, some materials were co-extruded (multiple ingots in one can) while others underwent single extrusion (one ingot in one can) using a standard, nearest diameter liner. For any alloy, if additional extrusion passes were required, the abovementioned procedure was repeated. It is noted that the extrusion factors (k) were provided by each vendor that performed the extrusion, to properly account for the frictional loads associated with each extrusion press.

After extrusion, the steel cans were removed either chemically (pickled in nitric acid) or mechanically (cut and stripped), and rods were centerless ground to a final diameter.

Characterization

Optical and electron microscopy were performed at room temperature in the as-extruded and aged conditions. Small disks, 5 mm in diameter, were mounted, polished, and etched using a solution of 10% HF, 40% HNO_3, and 50% H_2O (by volume) to reveal the underlying microstructure (i.e., grain size, inclusions and any other defects). An Hitachi 4700 scanning electron microscope (SEM) equipped with an IXRF energy-dispersive X-ray spectroscopy (EDS) detector was used for imaging and compositional analysis. Samples for transmission electron microscopy (TEM) consisted of disks 3 mm in diameter that were mechanically ground to ~ 130 µm thickness, and then electropolished using a

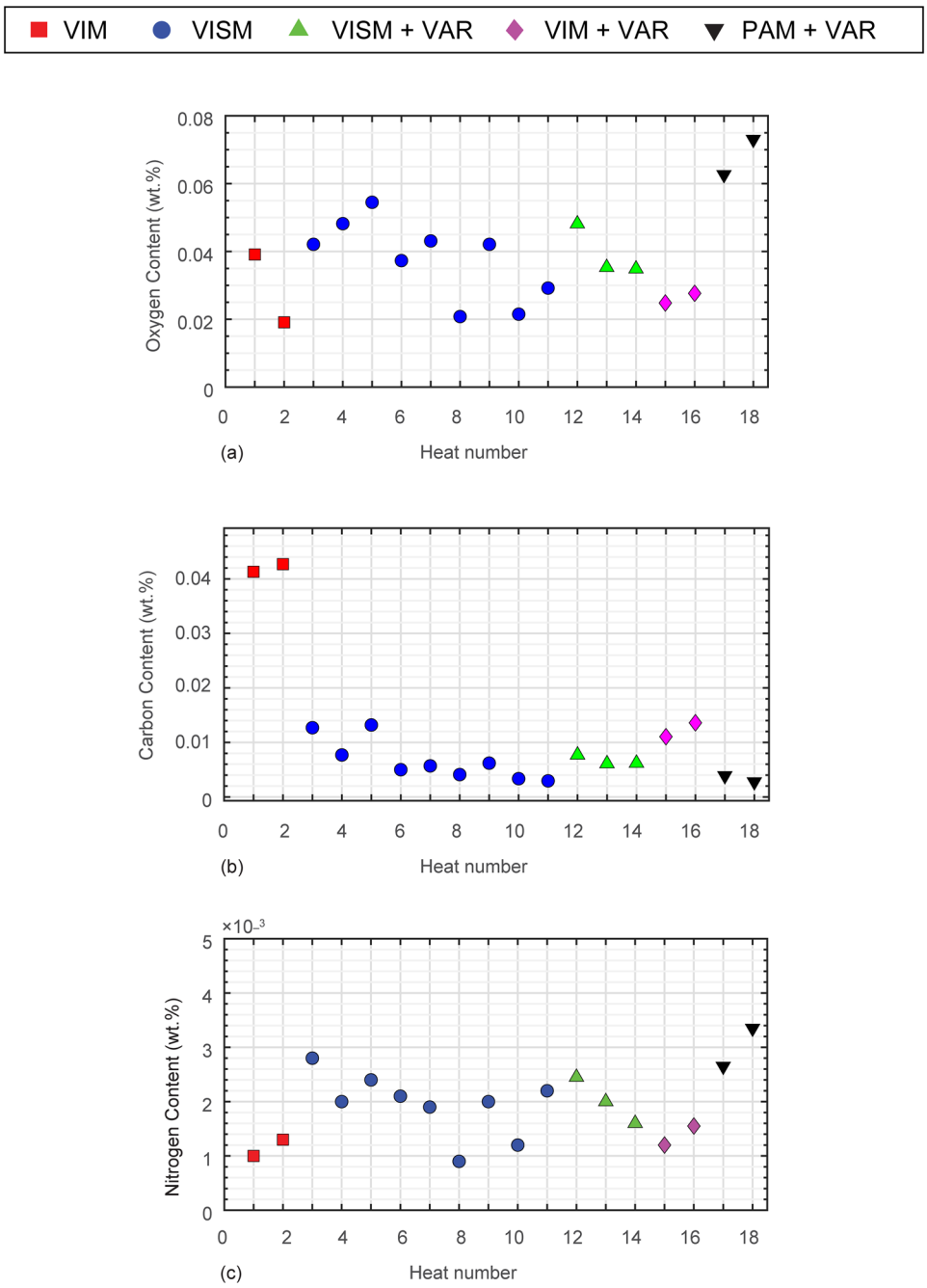

Fig. 3 Measured interstitial levels using **a** inert gas fusion method for oxygen determination, **b** combustion method for carbon determination, and **c** inert gas fusion method for nitrogen determination. The process types are *1* vacuum induction melting (VIM *filled red square*), *2* vacuum induction skull melting (VISM *filled blue circle*), *3* vacuum induction skull melting + vacuum arc remelting (VISM + VAR *filled green triangle*), *4* VIM + VAR *filled pink diamond*, and *5* plasma arc melting + vacuum arc remelting (PAM + VAR *filled inverted black triangle*) (Color figure online)

solution of 20% H_2SO_4 and 80% methanol (by volume) cooled to − 5 °C in a Struers Tenupol-5 twin-jet electropolisher. TEM high angle annular dark field (HAADF) images and diffraction patterns were collected at room temperature using a double-tilt holder in an FEI Talos F200S transmission electron microscope operating at 200 kV, fitted with STEM and EDS detectors. An open-source image processing software (ImageJ) https://imagej.nih.gov/ij/docs/faqs.html was used to calculate the inclusion particle sizes and area fractions.

XRD data collection and analysis were conducted on the alloys to identify the lattice parameters and phases present in each material heat. XRD scans were collected at both room temperature and at 300 °C from 5 mm diameter disks. Room-temperature data were gathered on a Bruker D8 Advance diffractometer with Cu Kα radiation using Bragg–Brentano geometry with variable slits and the samples were rotated during data acquisition. High-temperature data were gathered on a Bruker D8 Discover instrument using Cu Kα radiation, a 0.5 mm diameter monocapillary collimator, and a Vantec 500 area detector. For each sample,

a series of six overlapping 2D frames was gathered covering a 2θ range of 16°–164°. Separate calibration constants (beam X/Y center and detector distance) were determined for each frame position using the materials analysis using diffraction (MAUD) program [29] with the National Institute of Standards and Technology (NIST) 660a (LaB6) reference standard. The samples were heated to 300 °C using a strip heater and a custom-made sample holder to ensure temperature uniformity between samples, which was verified with multiple runs on several samples instrumented with a thermocouple. The 2D frames were integrated into 1D scans using the Bruker general area detector diffraction system (GADDS) program.

Elemental compositions were determined using inductively coupled plasma atomic emission spectroscopy (ICP-AES) for metallic elements, and the LECO® nitrogen/oxygen and carbon/sulfur determinators for nitrogen, oxygen, and carbon contents. Nitrogen and oxygen were measured using the inert gas fusion method by melting samples in a resistance furnace in a stream of helium according to ASTM E1409 [30]. The carbon was measured using combustion, where the sample was melted in an induction furnace in a stream of oxygen according to ASTM E1019 [31].

Transformation temperatures were determined by differential scanning calorimetry (DSC) using a TA Instruments Q1000. Small disks, 5 mm in diameter by 1 mm thick, were thermally cycled ten times between 0 and 350 °C using a heating/cooling rate of 10 °C/min.

Thermophysical properties were determined for a representative set of alloys. Density (ρ) was measured using a Micromeritics Accupyc 1340 helium pycnometer. Thermal diffusivity (α) measurements were performed at the Thermophysical Properties Research Laboratory using the laser flash method as outlined in ASTM E1461 [32]. Specific heats (c_p) were measured using a Perkin Elmer DSC-2 differential scanning calorimeter as outlined in ASTM E1269 [33]. Thermal conductivity, k, was determined as the product of the measurements given by:

$$k = \alpha \times c_p \times \rho \tag{1}$$

Electrical resistivity was determined using a standard four-probe technique per ASTM B84 [34]. Two voltage probe wires and two thermocouples were attached to a sample holder in the furnace. A constant Argon gas flow was transmitted into the test chamber while the sample was heated and cooled at a rate of 2 °C/min. Direct current was passed through the sample in one direction, while recording

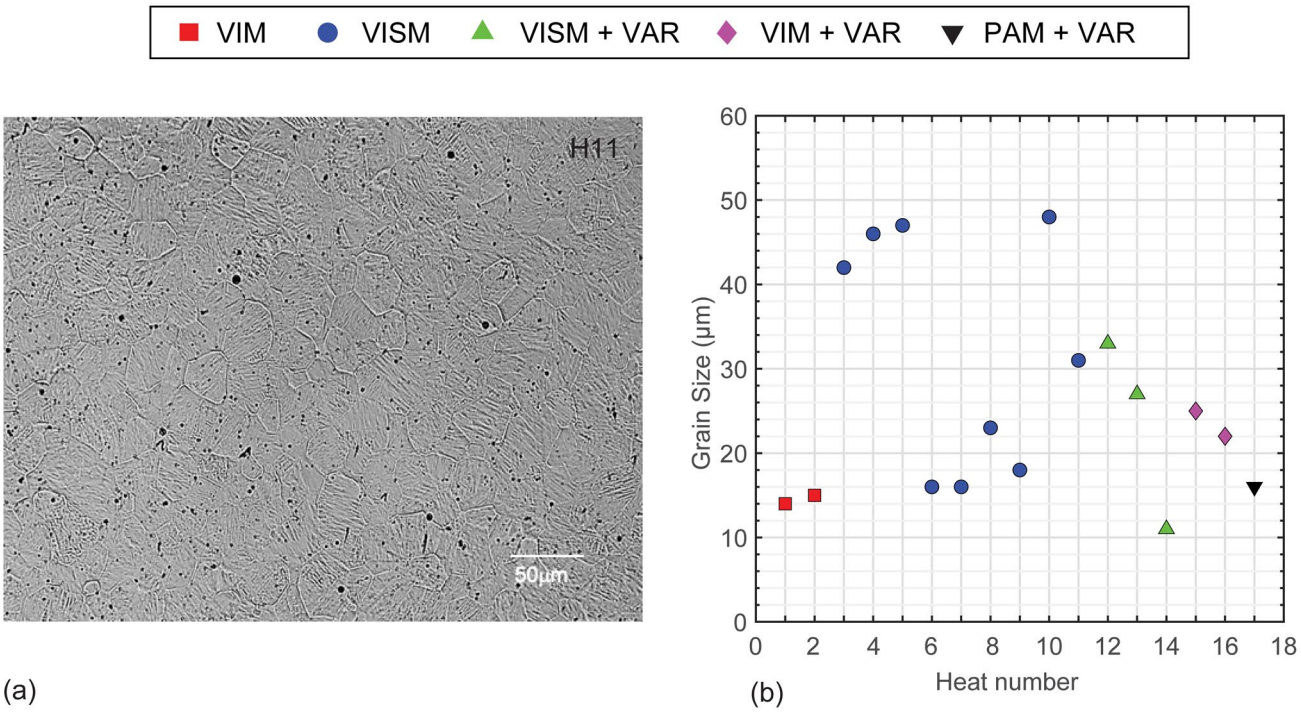

Fig. 4 **a** An optical micrograph of an etched sample revealing the grain structure and **b** a summary of the average grain size for each heat. The process types are *1* vacuum induction melting (VIM *filled red square*), *2* vacuum induction skull melting (VISM *filled blue circle*), *3* vacuum induction skull melting + vacuum arc remelting (VISM + VAR *filled green triangle*), *4* VIM + VAR *filled pink diamond*, and *5* plasma arc melting + vacuum arc remelting (PAM + VAR *filled inverted black triangle*) (Color figure online)

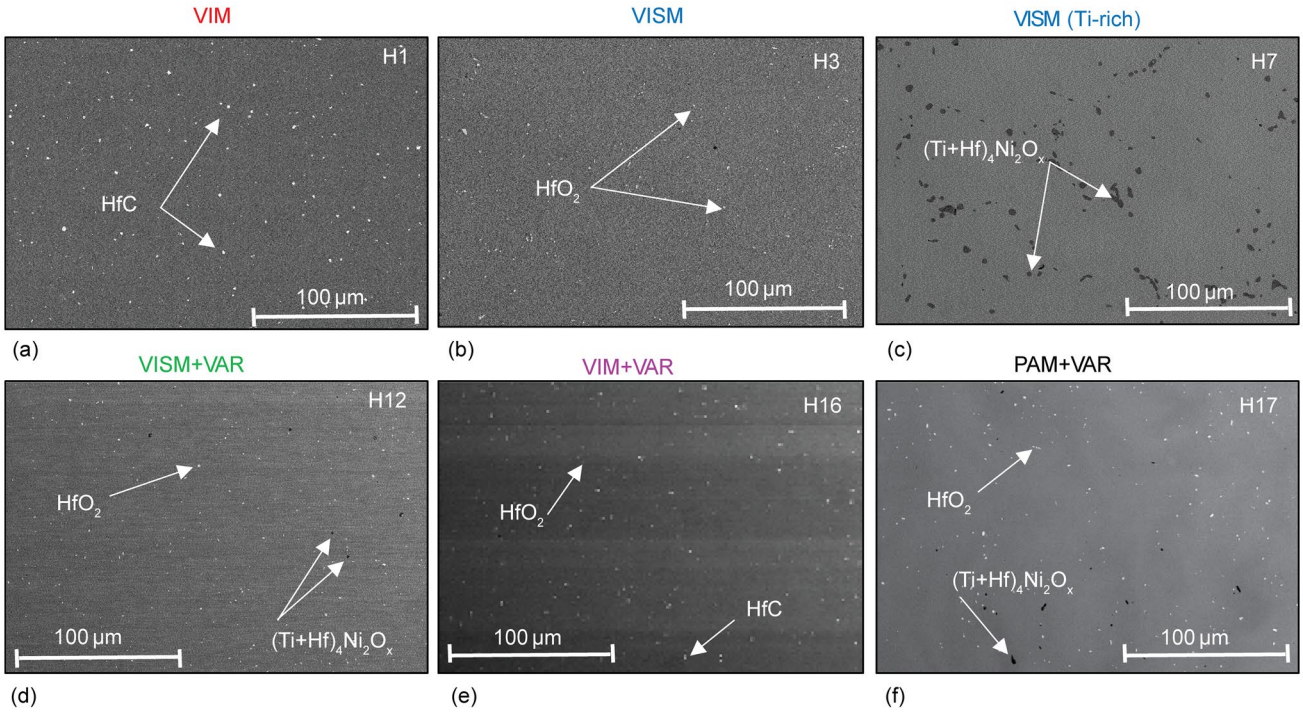

Fig. 5 Representative SEM micrographs of select alloys in the aged condition obtained from samples' cross sections. **a** Alloy H1 with hafnium carbides (HfC) present, **b** alloy H3 containing hafnium oxides (HfO_2), **c** alloy H7 with $(Ti+Hf)_4Ni_2O_x$ type oxides, **d** alloy H12 with both HfO_2 and $(Ti+Hf)_4Ni_2O_x$ type oxides, **e** alloy H16 with both HfO_2 and HfC, and **f** alloy H17 with both HfO_2 and $(Ti+Hf)_4Ni_2O_x$ type oxides. The process types are *1* vacuum induction melting (VIM), *2* vacuum induction skull melting (VISM), *3* vacuum induction skull melting + vacuum arc remelting (VISM + VAR), *4* VIM + VAR, and *5* plasma arc melting + vacuum arc remelting (PAM + VAR)

measurements of current, voltage drop, and temperature from the two thermocouples. The current was then reversed and the measurements repeated. Finally, linear thermal expansion was measured using a Theta Dilatronics II dual push-rod dilatometer following ASTM standard testing procedure E228 [35]. The heating and cooling rate was 2 °C/min in a helium environment.

Hardness measurements were performed using a Struers DuraScan automated Vickers microhardness tester. Mechanically polished samples were indented in 10 locations (in a cross pattern) with 1 kgf applied load for 13 s.

Thermomechanical testing was conducted using MTS 810 servohydraulic load frames equipped with Ameritherm NovaStar 7.5 kW induction heaters. Temperature was measured using Eurotherm temperature controllers and type-K thermocouples spot-welded onto the sample's gage section. Strain was measured using a high-temperature, 12.7 mm gauge length extensometer. Isothermal tension and compression tests were performed in strain control at a rate of 1×10^{-4}/s. Room-temperature testing followed ASTM E3098 (Uniaxial Pre-strain and Thermal Free Recovery) [36] and consisted of loading at room temperature to a target engineering stress of ± 1 GPa or to failure, whichever occurred first, unloading to 0 MPa, and then thermal cycling at 20 °C/min to 300 or 350 °C and returning to room temperature. High-temperature isothermal testing consisted of mechanically cycling the sample between 0 MPa and an engineering strain of 3% at temperatures above the austenite finish temperature in nominally 20 °C increments to observe the superelastic effect, if any. The second set of experiments consisted of uniaxial constant force thermal cycling tests following a modification of ASTM E3097 [37] with loading performed at the lower cycle temperature (LCT). Stresses from 0 to ± 500 MPa were applied in series with two thermal cycles at each stress level using a LCT of 35 °C and upper cycle temperatures up to 450 °C. Sample geometry consisted of cylindrical dogbone specimens (designed for reverse-load testing) with gage dimensions of 5.08 mm in diameter and 12.7 mm in length and threaded on both ends. This sample geometry was used for both tensile and compression testing. Data parsing were performed using NASA's custom SMA analysis tools implemented in MATLAB® software.

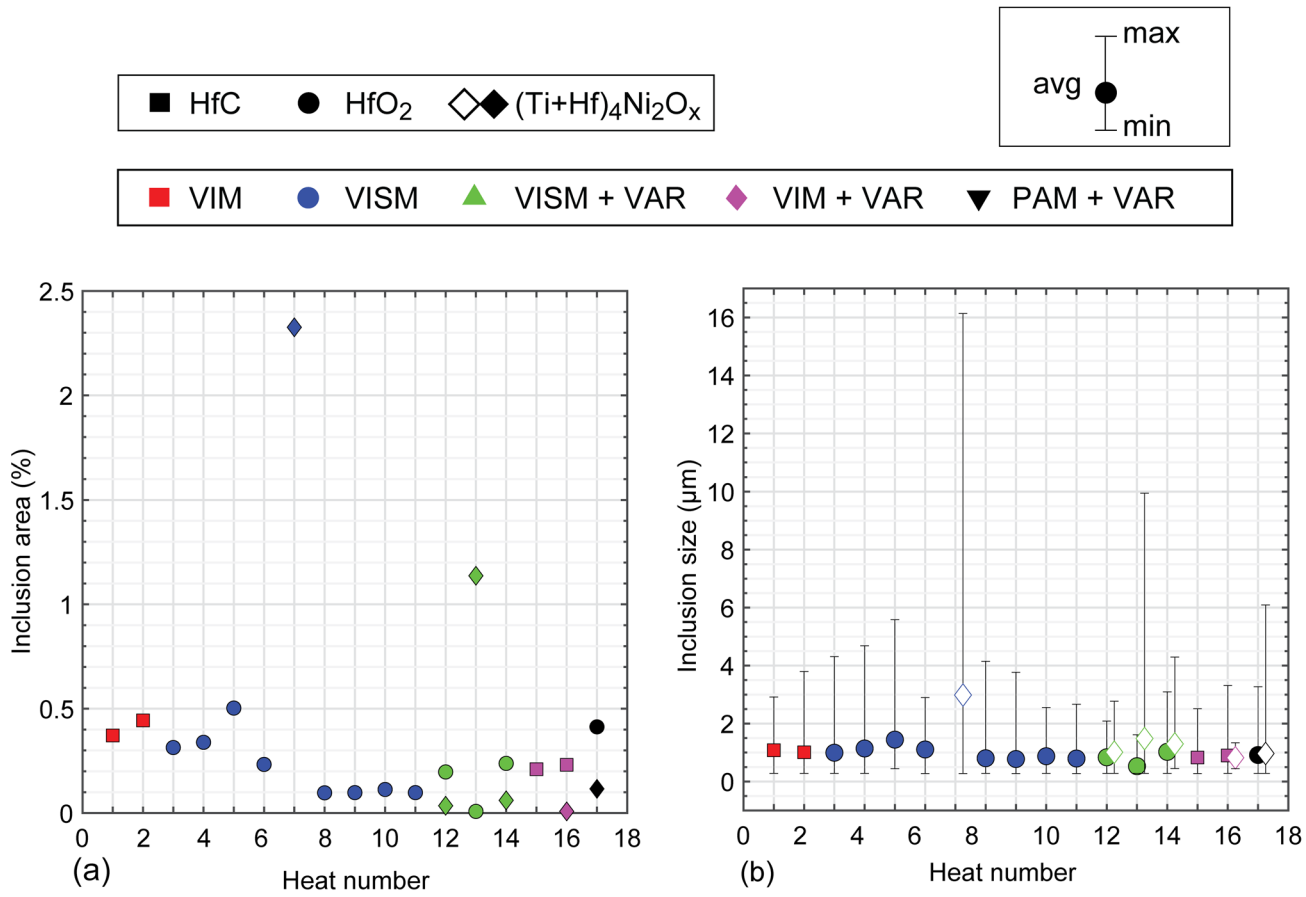

Fig. 6 Summary of inclusion types detected in each alloy. **a** Inclusion area fraction and **b** inclusion size shown as the average Feret diameter with error bars used to denote the maximum and minimum sizes. Data were measured using ImageJ image processing software. The process types are *1* vacuum induction melting (VIM *filled red square*), *2* vacuum induction skull melting (VISM *filled blue circle*), *3* vacuum induction skull melting + vacuum arc remelting (VISM + VAR *filled green triangle*), *4* VIM + VAR *filled pink diamond*, and *5* plasma arc melting + vacuum arc remelting (PAM + VAR *filled inverted black triangle*) (Color figure online)

Results and Discussion

Chemistry and Impurities

The chemical compositions as determined by the ICP method are shown in Fig. 2 for nickel (Ni), titanium (Ti), hafnium (Hf), and zirconium (Zr). The target composition, represented by the open symbols, was 50.3Ni, 29.7Ti, and 20Hf (at.%), except for heat H11, which had a target composition slightly more Ni-rich at 50.4 at.%. The actual measurements are represented by the solid symbols and exhibit some scatter. Inherent to this measurement technique, the measured values may vary based on the levels of analytes, element type, or material matrix, and are limited to an accuracy of ± 2% relative to the amount reported. Despite this, a general trend can be observed where a narrower scatter is obtained for the later heats. This is attributed to a combination of the melting conditions and the choice of elemental constituents used. A tighter control over the melting practice, such as vacuum levels, starting raw stock, and the materials in contact with the melt pool, all play an important role in the ensuing product. VIM heats (Heat H1 and H2) were melted in graphite crucibles and were expected to yield the largest deviation in Ti due to the strong affinity of Ti for carbon, producing TiC. It is noted that heat H1 was used as a reference, as this material was part of the first report of the outstanding functional properties in this target composition [13], upon which all other studies were based. VISM heats (heats H3 through H11) show the largest variation, particularly for the early trials, as the melting process was still being optimized. Heat H3 yielded comparable chemical compositions to prior melts, but with a slightly larger variance in the Hf component. Referring back to Table 1, this heat was produced using a relativity lower Hf purity of ≥ 99.5% as compared to the 99.9% of prior heats, and with

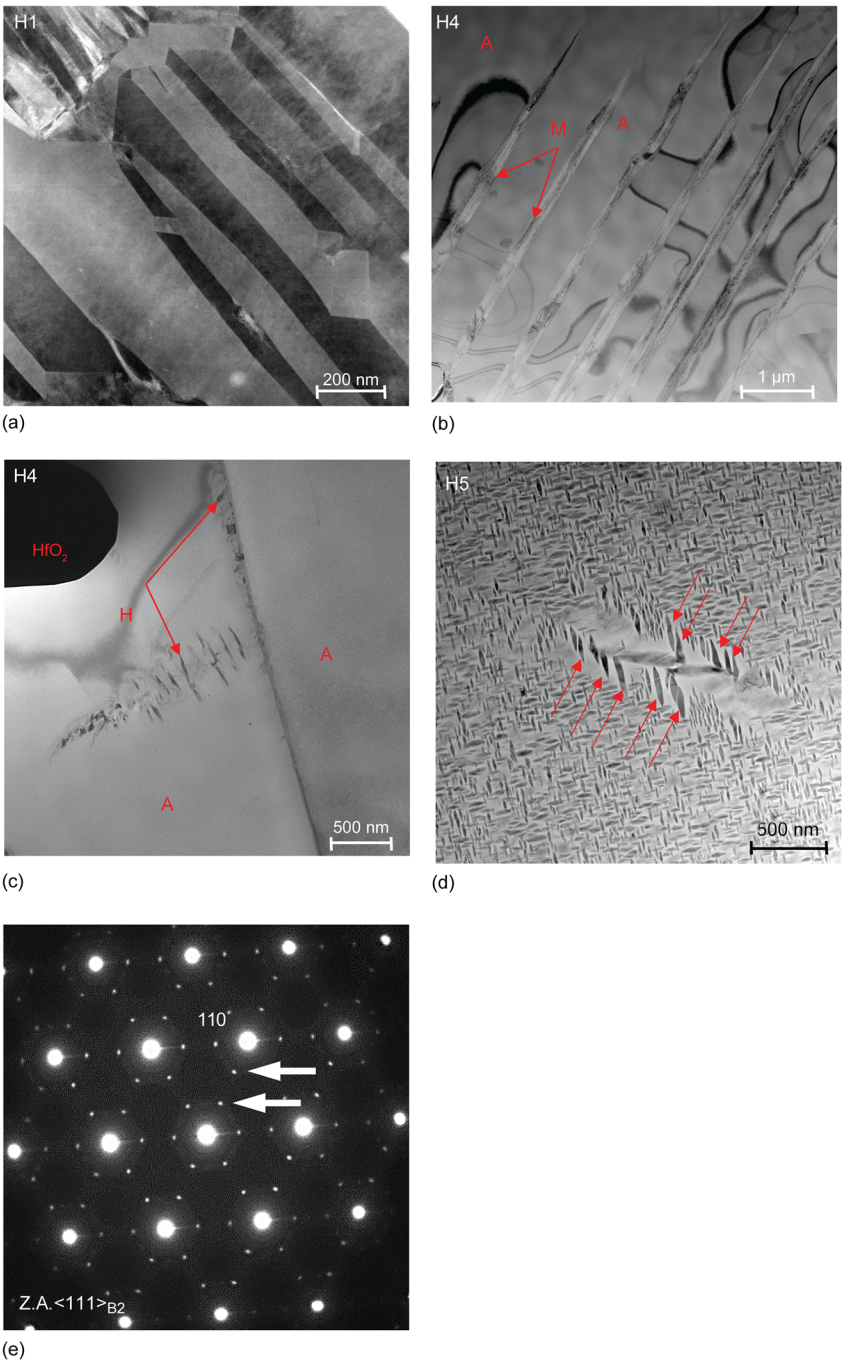

Fig. 7 Representative TEM micrographs of select alloys in the as-extruded condition. **a** Alloy H1 with single-phase microstructure showing martensite twins, **b** alloy H4 showing dual microstructure composed of martensite (denoted by "*M*") and austenite (denoted by "*A*"), **c** alloy H4 with secondary phases at substructures (denoted by "*H*"), **d** alloy H5 with a large distribution of precipitates, and **e** selected area diffraction pattern (SADP) confirming the precipitates are the H-phase as indicated by the 1/3, 2/3 $<110>_{B2}$ extra spots (*arrows*) in the $<111>_{B2}$ zone axis

higher Zr content, as shown in Fig. 2. Nonetheless, Ni and Ti and Hf + Zr were analogous and the heat was expected to exhibit similar behavior.

Chemical composition of heat H4 indicates a very large deviation in all elements, with a significant loss in Hf. In this heat, the charge was placed directly on the segmented crucible (i.e., no skull), and it is believed to have pulled the denser element (Hf) to the bottom and to the walls of the crucible. Thus, the resulting melt deviated largely from the target formulation. In an effort to correct the missed target, the resulting ingot was remelted with an estimated element adjustment, based on the initial chemical analysis, by adding more Hf, but that effort resulted in even larger deviations in chemistries as shown by heat H5. Moreover, it was found that this heat contained 2.5 at.% Fe (compared with < 80 ppm in other heats), which was inadvertently introduced during this remedial trial. This was the only heat in which an attempt was made to try to correct the missed target composition, as it did not yield a positive outcome.

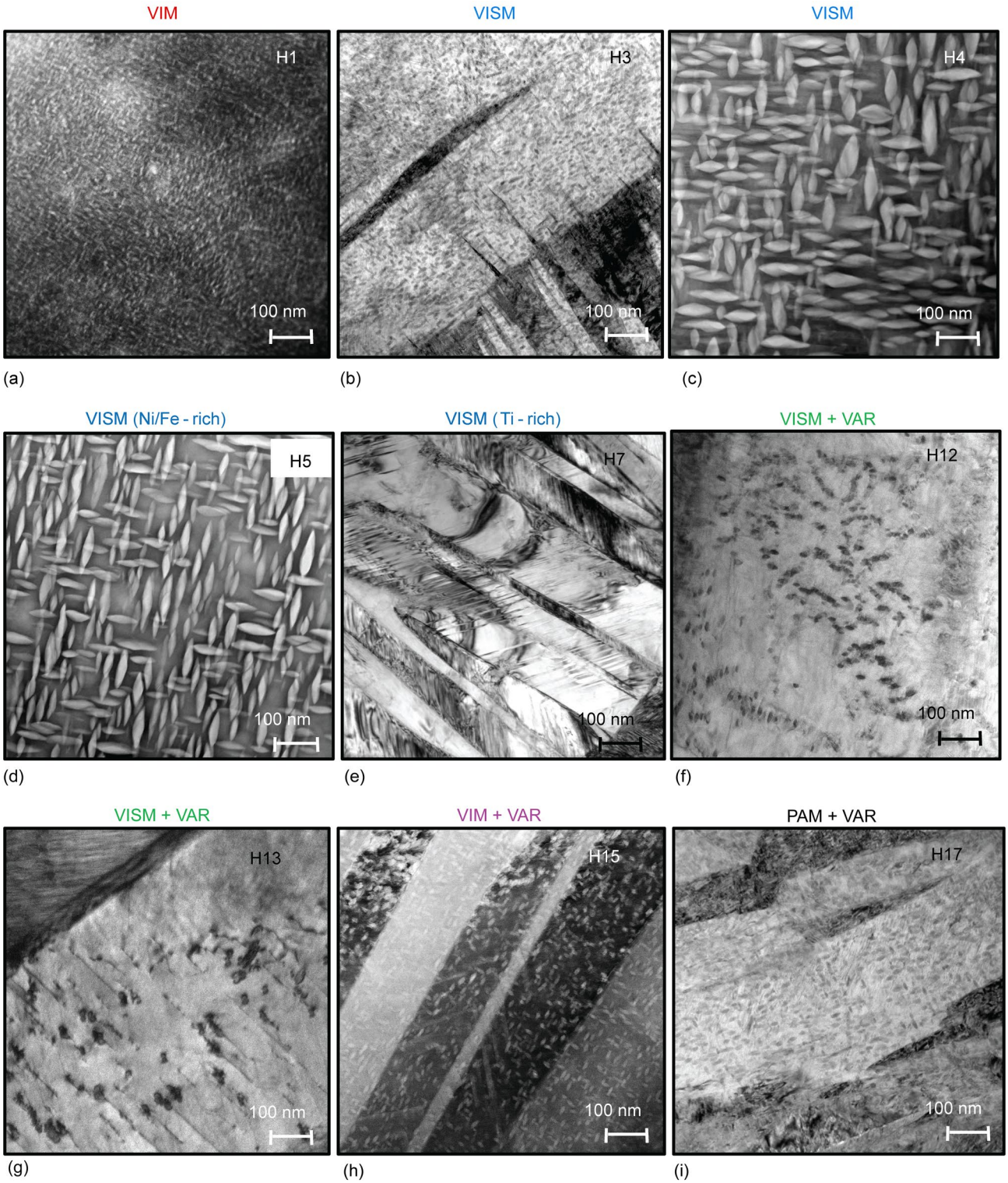

Fig. 8 Representative TEM micrographs of select alloys aged at 550 °C for 3 h and air cooled. All micrographs are at the same magnification and demonstrate the qualitative size and area fraction of H-phase precipitates in each alloy after undergoing the same aging heat treatment. Note that alloy H7 **e** has no precipitates. **a** Alloy H1, **b** alloy H3, **c** alloy H4, **d** alloy H5, **e** alloy H7, **f** alloy H12, **g** alloy H13, **h** alloy H15, and **i** alloy H17

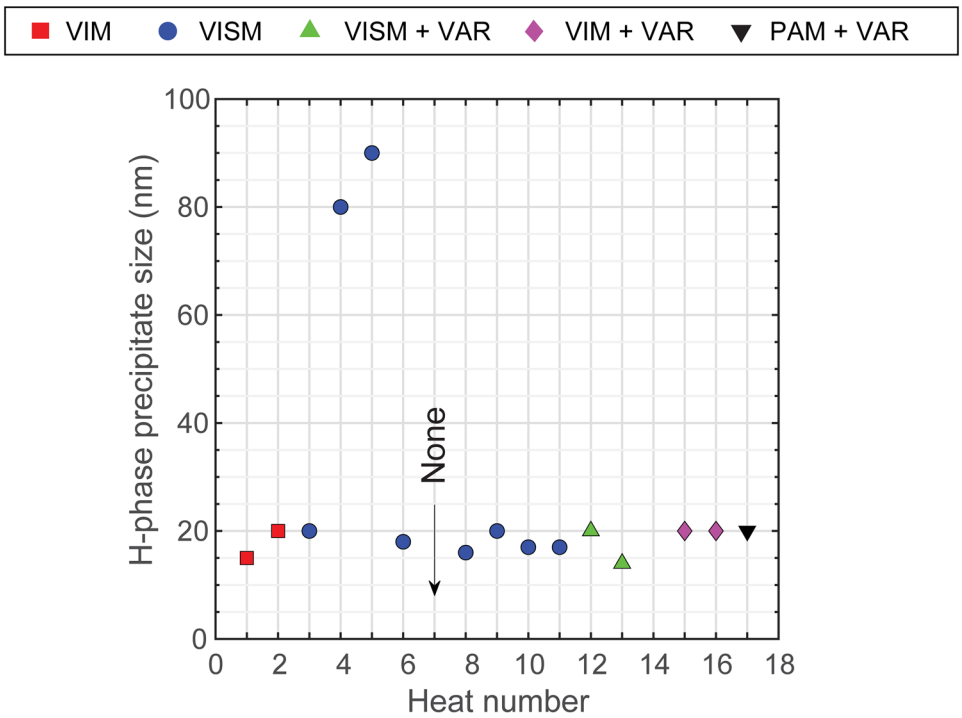

Fig. 9 Average H-phase precipitate size corresponding to each alloy aged at 550 °C for 3 h and air cooled. The process types are *1* vacuum induction melting (VIM *filled red square*), *2* vacuum induction skull melting (VISM *filled blue circle*), *3* vacuum induction skull melting + vacuum arc remelting (VISM + VAR *filled green triangle*), *4* VIM + VAR *filled pink diamond*, and *5* plasma arc melting + vacuum arc remelting (PAM + VAR *filled inverted black triangle*) (Color figure online)

On successive VISM heats, a skull from the previous melts was used to act as a protective layer. Heats H6 and H8–H11 were all within the expected values (based on heat H1 with respect to target) and were all produced with the same starting skull. However, heat H7 was not only off-target but also had a Ni-lean matrix. The root cause was not fully identified, but it is speculated that the starting charge weight was off-target before melting. The VISM + VAR heats (12–14) were all produced with no pre-existing skull and show closer results in the Ni values, but with a notable scatter in the Ti measurements. The succeeding VIM + VAR (heats H15 and H16) and PAM + VAR (heats H17 and H18) trials show the closest results to the target compositions.

Figure 2d illustrates the measured Zr content of each bulk alloy as a function of heat number. The Hf is a by-product of the Zr refining process, and because the two elements are very similar, it is extremely difficult to remove all the Zr [38]. The Zr levels are shown to range from ~ 0.7 at.% to less than ~ 0.2 at.% in the latter heats by substituting purer Hf sponge and/or crystal bars. This comes at a higher cost as purer Hf crystal bar milled chips of 99.7% with Zr nominal 3% can cost on order of $5000/kg, compared with ~ $3000/kg for Hf sponge with a 99.6% purity, or upwards of ~ $8000/kg for a 99.9% purity.

Bulk carbon (C), oxygen (O) and nitrogen (N) impurities were also measured as shown in Fig. 3. It is known that these impurities, particularly in large volume, may affect the martensitic transformation temperatures of NiTi-based alloys by forming compounds with Ti and thereby changing the matrix composition [39]. In addition, they can also render the cold/hot working more challenging due to embrittlement and changes in other microstructural features (e.g., stringer formation in cold drawn wire [40, 41]). The oxygen content (Fig. 3a) varied between 200 and 750 ppm, with the highest value recorded when using the PAM + VAR process. In this latter, relatively new melting technique for NiTiHf alloys, it is believed that vacuum levels may not have been high enough, resulting in higher oxygen levels. Otherwise, oxygen content appeared to fluctuate (0.02–0.055 wt.%) irrespective of the process used, and this is attributed to the varying oxygen content of the starting raw materials. Carbon content (Fig. 3b) ranged from 427 to as low as 28 ppm. As expected, the VIM processes represented by heat H1–H2 and heats H15–H16 incurred the highest levels of carbon, which comes from the use of graphite crucibles. Unlike oxygen sources originating mostly from the raw materials, the carbon levels can be highly influenced by the purity and porosity of the crucible [42]. Heats H1 and H2 contained the highest levels of carbon at an average of 420 ppm, while heats H15 and H16 contained on average 123 ppm. It is also noted that the heat sizes were different, contributing to the changes in ratio between the wall apparent contact surface area and the liquid volume. The decrease in carbon levels can be attributed to this effect in addition to the use of higher density crucibles. The lower carbon content could also be from the melt stock charging method, as outlined in [43]. Frenzel et al. showed that the placement of the Ni and Ti in the crucible can play a large role in the final carbon

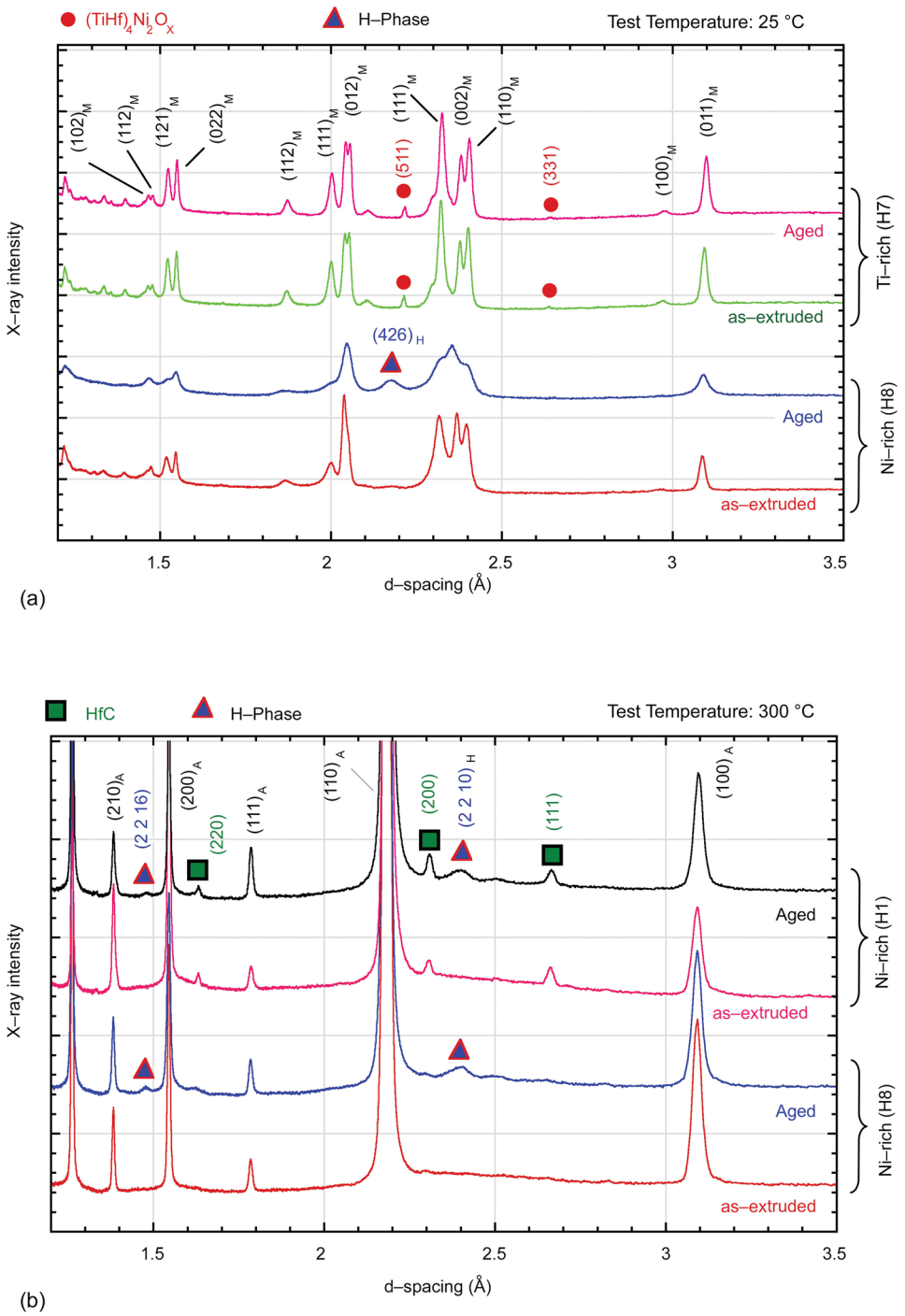

Fig. 10 Representative x-ray diffraction spectra. **a** B19′ martensite phase measured at room temperature for alloy H8 (Ni-rich) and H7 (Ti–rich) before and after aging. Alloy H8 shows a distinct $(426)_H$ H-phase peak after aging (labeled with a *blue triangle*), while alloy H7 does not form any H-phase, but shows the $(Ti+Hf)_4Ni_2O_x$ type oxides before and after aging (labeled with *red circles*). **b** B2 austenite measured at 300 °C for alloy H8 (Ni-rich) and H1 (Ni-rich) before and after aging. Both alloys show distinct H-phase peaks after aging (labeled with *blue triangles*), in addition to some HfC in alloy H1 (labeled with *green squares*) (Color figure online)

content of the ingot. In addition, multiple uses of a crucible for melts of the same composition can lower the carbon content of the ingot given the presence of a layer of material coating the crucible. For the other processing methods (VISM, VISM + VAR and PAM + VAR), the carbon levels were below 150 ppm, as melting was performed in a copper hearth (and using previous skulls). Lastly, nitrogen content was in a range between 10 and 35 ppm for all processes, and no consistent trend was observed.

Inclusions and Microstructural Analysis

Optical microscopy was conducted on the etched cross sections of each extrusion run to estimate the grain size. Due to different extrusion ratios and temperatures (Table 2), the grain size in different bars varied from 10 to 50 µm. In all cases, the grains were roughly equiaxed in shape, indicative of a recrystallized microstructure. An optical micrograph of an etched sample revealing the grain structure (average

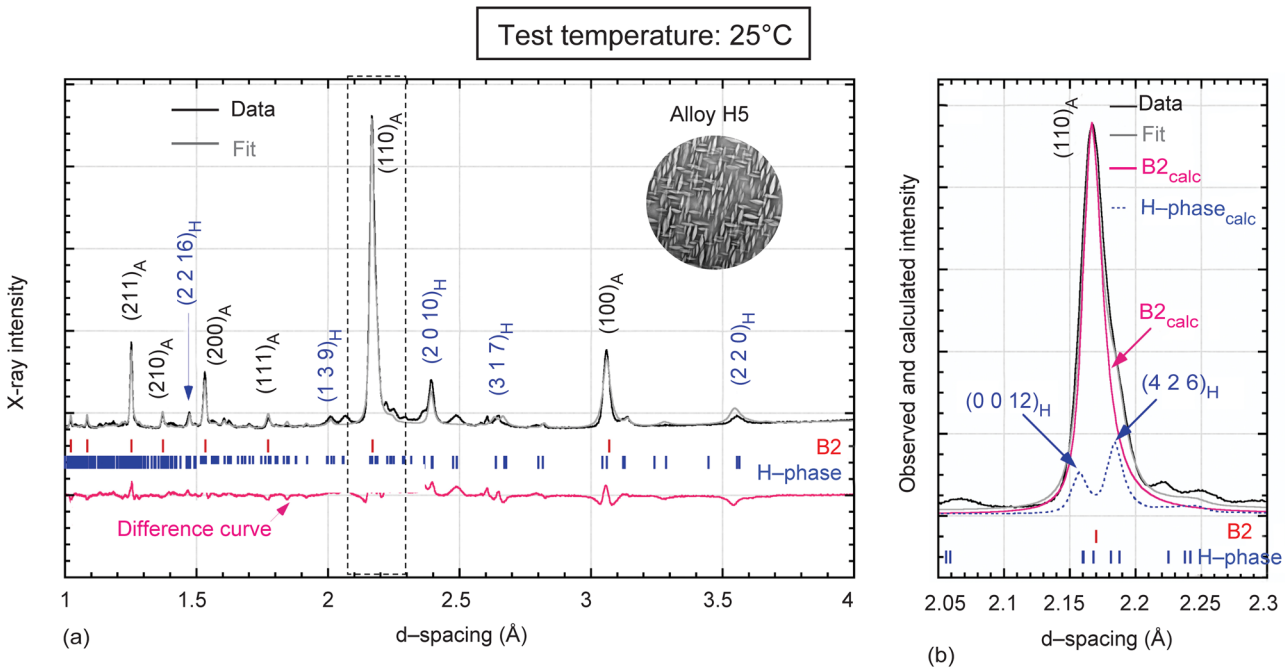

Fig. 11 X-ray diffraction pattern corresponding to alloy H5 aged at 550 °C for 3 h and air cooled. Included are the raw data, Rietveld refinement fit, peak positions, and the difference curve. **a** The spectrum is austenitic at room temperature with a large amount of the H-phase precipitates. **b** Observed and calculated intensity showing the overlapped $(4\ 2\ 6)_H$ and $(0\ 0\ 12)_H$ H-phase reflections with the $(110)_A$ austenite peak

grain size of ~ 30 µm) for heat H11 is shown in Fig. 4a. A summary of the grain sizes for each heat is shown in Fig. 4b.

Representative SEM micrographs corresponding to the aged samples taken from the cross section of the rods are shown in Fig. 5. It is known that inclusions are primarily influenced by the melting technique, and depending on the process used, three types of non-metallic and intermetallic inclusions in the form of oxides or carbides were identified using EDS, as labeled in each figure. HfC inclusions were observed in the VIM processed material (Fig. 5a), as anticipated from the use of graphite crucibles. Using a carbon-free process (VISM) generally resulted in material that contained isolated HfO_2 (Fig. 5b), with the exception of heat H7 (Fig. 5c), which contained large amounts of $(Ti+Hf)_4Ni_2O_x$ distributed mostly along the grain boundaries. These latter inclusions are typically observed in near-stoichiometric or Ti-rich NiTi alloys [44, 45]. The VISM + VAR heats (Fig. 5d) contained both HfO_2 and trace amounts of $(Ti+Hf)_4Ni_2O_x$ with the exception of heat H13, which contained an unusually high amount of the latter (due to the Ti-rich composition). The VIM + VAR process (Fig. 5e) contained two types of Hf-containing inclusions, HfO_2 and HfC. The HfC inclusions were expected in this case. The HfO_2 inclusions were very infrequent and their presence varied from heat-to-heat. Finally, the PAM + VAR process (Fig. 5f) yielded similar results to that of the VISM + VAR process, where both HfO_2 and small amounts of $(Ti+Hf)_4Ni_2O_x$ inclusions were present. The $(Ti+Hf)_4Ni_2O_x$ in this case formed due to the high levels of oxygen in the alloy, as indicated in Fig. 3.

A quantitative analysis was performed using SEM micrographs and the *ImageJ* image processing tool to quantify the inclusion size and area fraction within the matrix. In all instances, the images were taken at a magnification of 500× for a good statistical representation of the microstructure. Figure 6a shows the area percentage of the inclusions for all processes and heats. Generally, the total inclusion content was below 1% (area percent), except for heats H7 and H13 which contained ~ 2.3 and 1.1%, respectively, of $(Ti+Hf)_4Ni_2O_x$ inclusions. It is noted that heat H7 was a Ti-rich alloy, which would have promoted a higher area percentage of this type of inclusion. While heat H13 has a lower Ti content than heat H7, it has the second lowest Ni content and second highest Ti content, with the stoichiometric ratio Ni:(Ti,Hf,Zr) = 1.007, which is most likely responsible for the high level of $(TiHf)_4Ni_2O_x$. Inclusion sizes were measured as the Feret diameter of each particle, and the error bars used to denote the maximum and minimum sizes are shown in Fig. 6b. Most heats contained inclusions with a maximum dimension of < 7 µm; the exceptions were heats H7 and H13, with a maximum inclusion size of 16 and 10 µm, respectively, due to the presence of $(TiHf)_4Ni_2O_x$.

TEM microstructures were obtained at room temperature for each material heat, as shown in Figs. 7 and 8. In

Table 3 Lattice parameters corresponding to each alloy in the as-extruded and aged conditions

Alloy ID	B19′				B2
	a (Å)	*b* (Å)	*c* (Å)	*β* (°)	a_0 (Å)
As-extruded condition					
H1	3.0502	4.0908	4.8694	103.02	3.0947
H2	3.0508	4.0881	4.8774	103.12	3.0944
H3	3.0569	4.0929	4.8806	103.21	3.0941
H4	3.0351	4.1108	4.8483	103.16	3.0814
H5	–	–	–	–	3.0809
H6	3.0500	4.0826	4.8768	103.23	3.0947
H7	3.0536	4.0816	4.8841	103.17	3.0973
H8	3.0480	4.0853	4.8693	103.15	3.0936
H9	3.0495	4.0868	4.8772	103.11	3.0936
H10	3.0468	4.0807	4.8612	103.2	3.0927
H11	3.0441	4.0824	4.8583	103.3	3.0925
H12	3.0539	4.0831	4.8788	103.3	3.0938
H13	3.0592	4.0760	4.8886	103.5	3.0962
H14	3.0565	4.0836	4.8866	103.4	3.0958
H15	3.0478	4.0825	4.8714	103.2	3.0937
H16	3.0528	4.0782	4.8772	103.2	3.0941
H17	3.0466	4.0821	4.8712	103.3	3.0937
Aged at 550 °C for 3 h					
H1 (aged)	3.0529	4.1029	4.8666	103.27	3.0934
H2 (aged)	3.0508	4.1148	4.8666	103.19	3.0937
H3 (aged)	3.0491	4.1172	4.8595	103.15	3.0921
H4 (aged)	3.0282	4.0835	4.8374	102.79	3.0786
H5 (aged)	–	–	–	–	3.0782
H6 (aged)	3.0539	4.0972	4.8658	103.25	3.0934
H7 (aged)	3.0557	4.0759	4.8848	103.35	3.0973
H8 (aged)	3.0485	4.1407	4.8703	103.21	3.0931
H9 (aged)	3.0554	4.1037	4.8685	103.24	3.0935
H10 (aged)	3.0444	4.0959	4.8445	103.2	3.0917
H11 (aged)	3.0427	4.0982	4.8450	103.2	3.0911
H12 (aged)	3.0549	4.0917	4.8721	103.3	3.0957
H13 (aged)	3.0591	4.0791	4.8902	103.5	3.0964
H14 (aged)	3.0565	4.0886	4.8824	103.5	3.0956
H15 (aged)	3.0460	4.0901	4.8568	103.2	3.0924
H16 (aged)	3.0444	4.0876	4.8556	103.2	3.0934
H17 (aged)	3.0457	4.0903	4.8547	103.3	3.0926

Aging was performed at 550 °C for 3 h under argon and then air cooled

the as-extruded condition (Fig. 7), most heats consisted of a precipitate-free B19′ monoclinic matrix consisting of the commonly observed (011)-Type I and (001)-compound twins as the dominant twinning modes [15]. A representative micrograph of this microstructure is shown in Fig. 7a. The exceptions to this trend were heats H4 and H5. Heat H4 consisted of a dual microstructure of B19′ martensite and B2 austenite (Fig. 7b), whereas heat H5 was fully austenitic B2, with no detectable martensite. In addition, in both cases, a precipitate phase was also present. In heat H4, this phase was very fine and detected only at grain boundaries and at dislocations/substructures (Fig. 7c). However, in heat H5 there was a high density of lenticular precipitates distributed uniformly throughout the matrix, and some relatively larger precipitates that had preferentially nucleated and grown at dislocations. An example is shown in Fig. 7d where the same variant of the parallel precipitates (marked by arrows) nucleated first on a set of aligned ordered array of dislocations and then grew larger by pipe diffusion. In both alloys, this precipitate phase was identified as the H-phase by diffraction analysis. A typical selected area diffraction pattern (SADP) in a $<111>_{B2}$ zone axis showing the characteristic 1/3, 2/3 $<110>_{B2}$ extra spots for the H-phase is shown in Fig. 7e. Given that both materials have a higher Ni or Ni/Fe content, it is reasonable to expect that these precipitates formed during cooling after the extrusion process.

After aging at 550 °C for 3 h and air cooling, the H-phase was observed in all the alloys except for heat H7. Representative TEM micrographs are shown in Fig. 8. This optimum aging treatment was chosen based on previous studies [12, 13] because it produced a uniform dispersion of 15–20 nm sized H-phase precipitates in a martensite matrix, and this microstructure produced superior thermomechanical properties. It is clear from Fig. 8 that the size and volume fraction of the H-phase precipitates differ from heat to heat. Bearing in mind that despite having the same target composition, the Ni content of the various heats was not identical, this difference in precipitation behavior is somewhat expected. For both of the VIM heats (H1, H2) and the majority of the VISM heats (H3, H6, and H8–H11), there was a high density of uniformly distributed fine (< 20 nm) H-phase precipitates throughout the matrix after aging. Representative micrographs of this microstructure are shown in Fig. 8a for H1 and Fig. 8b for H3. With this type of microstructure, the precipitates are small enough for the martensite twin boundaries to propagate freely without any hindrance during the transformation and have high enough precipitate volume fraction to provide an obstacle to dislocation motion, resulting in superior strength. In contrast, for VISM heats H4 and H5 (Fig. 8c, d, respectively), precipitation is uniform, but the precipitate size is significantly larger than the optimal size. This may negatively affect the transformation behavior as these relatively larger H-phase precipitates can act as obstacles for martensite propagation, resulting in degraded thermomechanical properties. VISM heat H7, shown in Fig. 8e, is an exception; it turned out to be a Ti-rich composition with a martensite matrix containing no precipitates, as expected. The VISM + VAR heats (Fig. 8f, g) show a

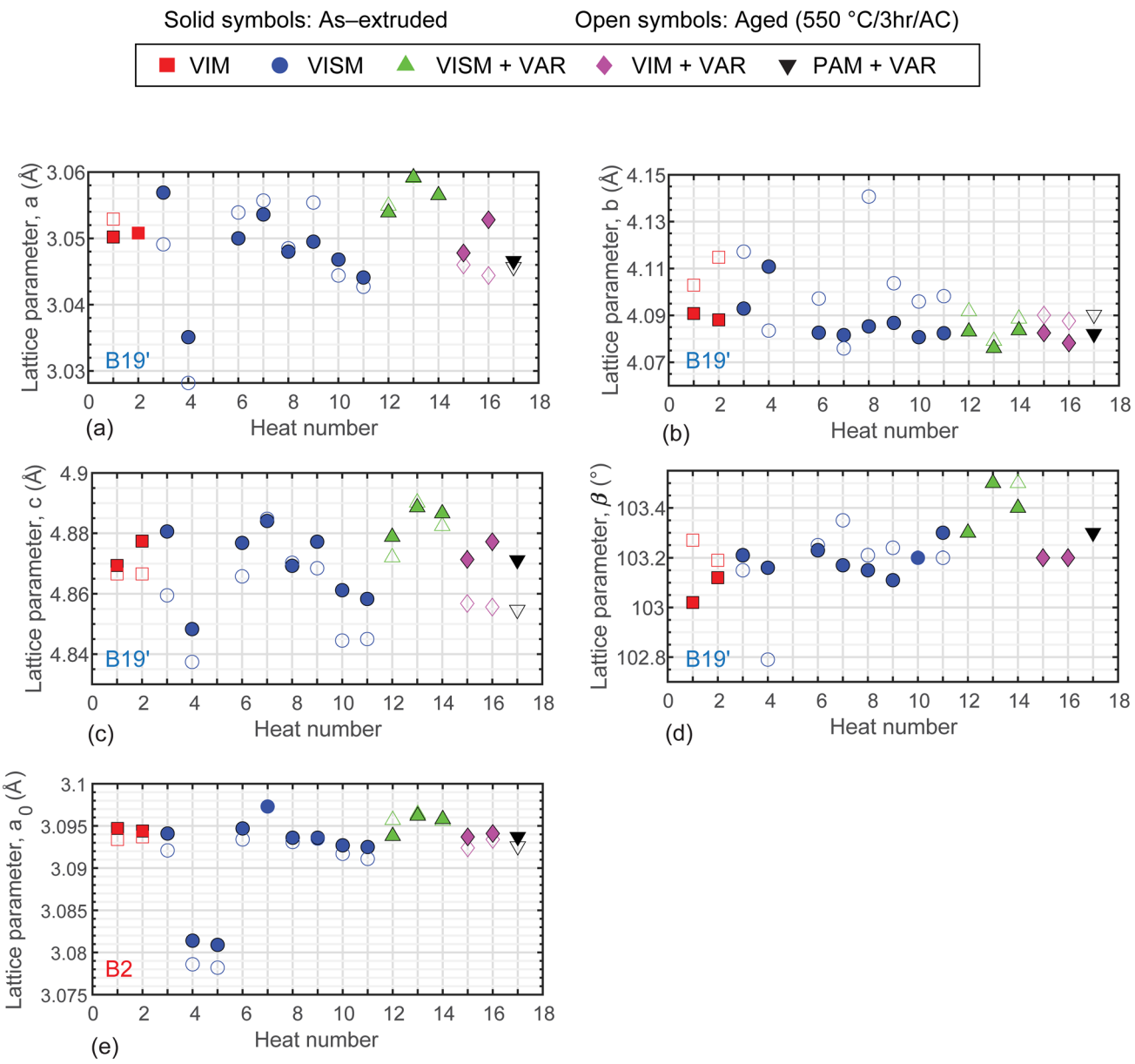

Fig. 12 Lattice parameters corresponding to each alloy in the as-extruded (*solid symbols*) and aged conditions (*open symbols*). **a**–**d** B19′ monoclinic lattice parameters, and **e** B2 cubic lattice parameters. *Error bars* are also included but they are smaller than the marker size. The process types are *1* vacuum induction melting (VIM *filled red square, open red square*), *2* vacuum induction skull melting (VISM *filled blue circle, open blue circle*), *3* vacuum induction skull melting + vacuum arc remelting (VISM + VAR *filled green triangle, open green triangle*), *4* VIM + VAR *filled pink diamond, open pink diamond*, and *5* plasma arc melting + vacuum arc remelting (PAM + VAR *filled inverted black triangle, open black inverted triangle*) (Color figure online)

much lower volume fraction of the H-phase, which did not form uniformly, but formed heterogeneously on dislocations. Finally, both VIM + VAR and PAM + VAR heats show the desired optimum size and distribution of the H-phase precipitates, as shown in Fig. 8h, i, respectively.

The average H-phase precipitate size for all heats was estimated from the TEM images and is shown in Fig. 9. The optimum size of 15–20 nm was achieved in most heats; the exceptions were heats H4 and H5, where the average size was > 80 nm, and heat H7 (Ti-rich), which did not form any precipitate phase after aging. However, the volume fraction appeared to vary, even among heats that had the optimum precipitate size. It should be noted that no attempt was made to measure the volume fraction of precipitates in different heats via TEM, since this measurement depends on several factors and may not provide accurate numbers and comparison. Only a qualitative estimate was made from the

Table 4 Lattice parameters and structures of matrix and secondary phases observed in the studied alloys

Phases	Lattice parameters				Abbreviated space group	Lattice structure
	a (Å)	*b* (Å)	*c* (Å)	*b* (°)		
Austenite	See Table 3				*Pm-3m*	B2 (cubic)
Martensite					$P2_1/m$	B19′ (monoclinic)
HfC	4.62	–	–	–	*Fm-3m*	Cubic
HfO_2[a]	5.12	5.17	5.30	99.2	$P2_1/c$	Monoclinic
$(Ti+Hf)_4Ni_2O_x$	11.51	–	–	–	*Fd-3m*	Cubic
H-phase	12.51	8.67	25.93	–	*Fddd*	Orthorhombic

[a]Lattice parameters not refined (amount present too small). Values are from PDF card 04–004-3850 (2018 PDF-4 +)

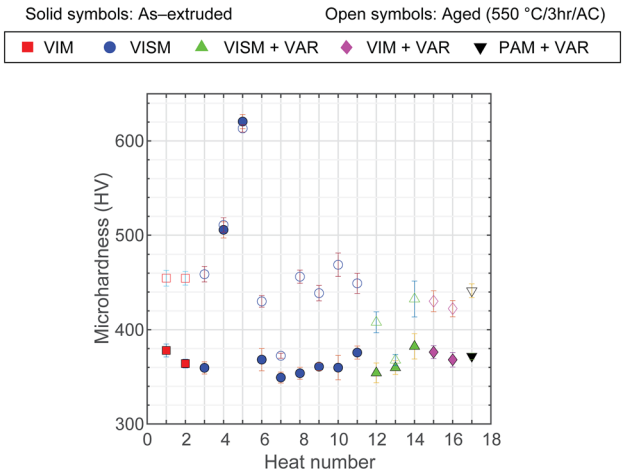

Fig. 13 Vickers micro-hardness corresponding to each alloy in the as-extruded (*solid symbols*) and aged conditions (*open symbols*) as a function of heat number. The process types are *1* vacuum induction melting (VIM *filled red square, open red square*), *2* vacuum induction skull melting (VISM *filled blue circle, open blue circle*), *3* vacuum induction skull melting + vacuum arc remelting (VISM + VAR *filled green triangle, open green triangle*), *4* VIM + VAR *filled pink diamond, open pink diamond*, and *5* plasma arc melting + vacuum arc remelting (PAM + VAR *filled inverted black triangle, open black inverted triangle*) (Color figure online)

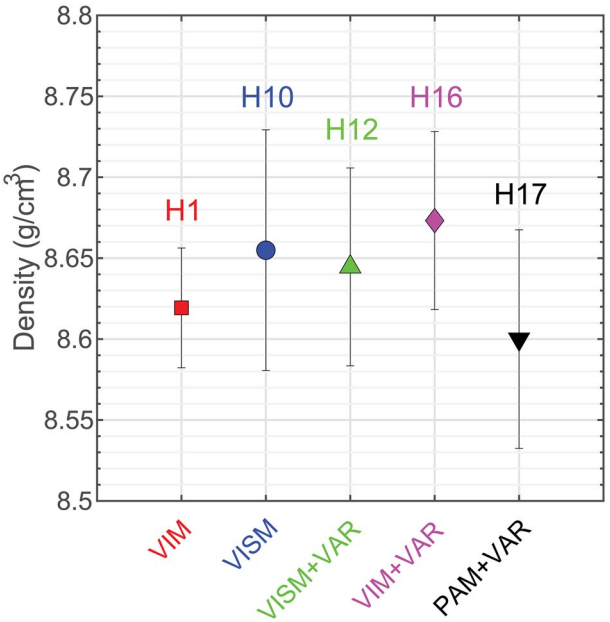

Fig. 14 Representative densities corresponding to alloy groups from each melting technique. The averaged value is shown with the standard deviation from ten measurements. The process types are *1* vacuum induction melting (VIM *filled red square*), *2* vacuum induction skull melting (VISM *filled blue circle*), *3* vacuum induction skull melting + vacuum arc remelting (VISM + VAR *filled green triangle*), *4* VIM + VAR *filled pink diamond*, and *5* plasma arc melting + vacuum arc remelting (PAM + VAR *filled inverted black triangle*) (Color figure online)

examination of various TEM images for each heat, as shown in Fig. 8.

X-ray Diffraction

Representative XRD spectra for both the B19′ phase measured at room temperature and the B2 phase measured at 300 °C are shown in Fig. 10 (except for heat H7, which was measured at 350 °C). For the room-temperature spectra (Fig. 10a) two alloys are shown, one corresponding to the Ni-rich composition (H8) and the other to the Ti-rich composition (H7) in the as-extruded and aged conditions. In the Ni-rich alloy H8, B19′ monoclinic peaks are present in the as-extruded condition, but a distinct new peak corresponding to $(426)_H$ appears around a *d*-spacing of 2.17 Å after aging. In addition, aging also produces peak shape changes around *d*-spacing of 1.55 and 2.4 Å. These observed changes after aging correspond to the precipitation of H-phase as previously discussed and reported in [46–49]. In the Ti-rich alloy H7, the X-ray pattern of as-extruded material shows the distinct B19′ monoclinic peaks with a few small peaks corresponding to the $(TiHf)_4Ni_2O_x$ inclusions. In this alloy, no changes were observed after aging, as expected.

The results of high-temperature X-ray data at 300 °C for the two Ni-rich alloys, H1 and H8, in both the as-extruded and the aged conditions are shown in Fig. 10b. In the as-extruded condition, alloy H1 exhibits typical peaks of the B2

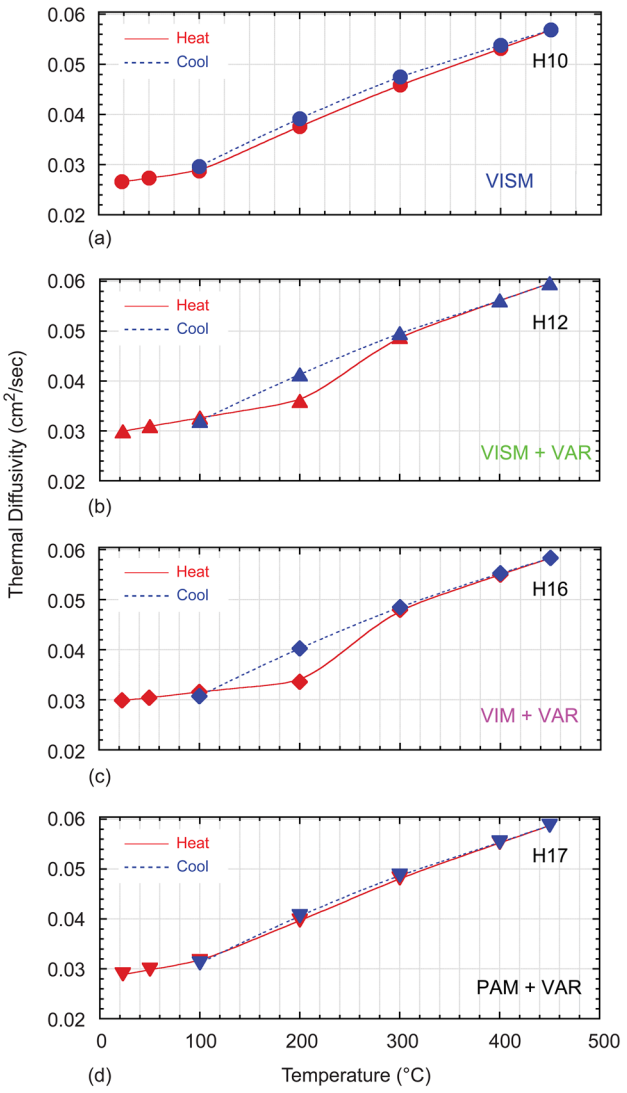

Fig. 15 Thermal diffusivity as a function of temperature for various alloys in the as-extruded condition. **a** Alloy H10, **b** alloy H12, **c** alloy H16, and **d** alloy H17

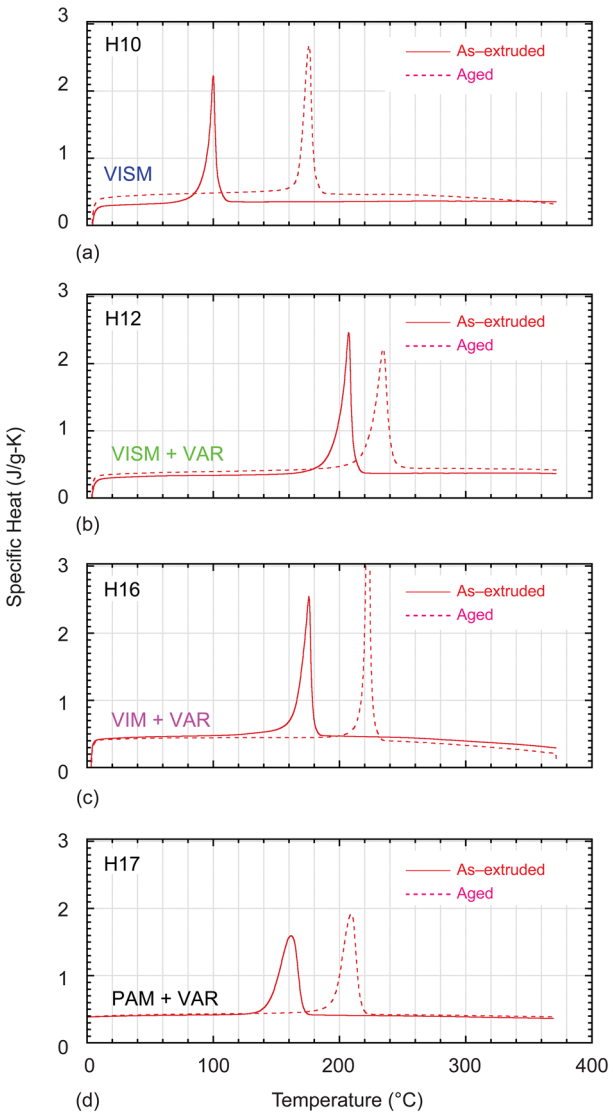

Fig. 16 Specific heat as a function of temperature for various alloys in the as-extruded and aged condition during heating cycle. **a** Alloy H10, **b** alloy H12, **c** alloy H16, and **d** alloy H17

cubic phase in addition to small peaks of HfC, whereas alloy H8 shows only the B2 cubic peaks, since HfO_2 contained in this alloy was too low to be detected. After aging, new peaks appear at *d*-spacing of 2.39 and 1.47 Å corresponding to $(2\ 0\ 10)_H$ and $(2\ 2\ 16)_H$, respectively, in both alloys. These peaks for the H-phase were also observed and reported in similar alloys studied by Prasher et al. [47].

The distinct $(426)_H$ peak close to 2.17 Å at room temperature that was observed in the H8 alloy in Fig. 10a is not visible in the high temperature X-ray pattern (Fig. 10b) due to its overlap with the high-intensity $(110)_A$ peak. Similarly, the $(2\ 0\ 10)_H$ and $(2\ 2\ 16)_H$ peaks observed in the high-temperature scan after aging (Fig. 10b) are not distinctly visible in the room-temperature scan (Fig. 10a) due to their overlap with the $(002)_M$ and $(102)_M$ peaks, respectively. To shed further light into these small, non-distinct precipitate peaks, an XRD pattern of the aged alloy H5 was taken at room temperature, as shown in Fig. 11. This alloy was Ni + Fe rich, austenitic at room temperature, and contained a high volume fraction (~ 26% as determined by XRD) of the relatively large (average size 90 nm) H-phase precipitates. It is clear from Fig. 11a that there are several distinct peaks of the H-phase in addition to the B2 cubic austenite matrix phase. The two small broad peaks $(2\ 0\ 10)_H$ and $(2\ 2\ 16)_H$ identified in Fig. 10b are much sharper and of reasonable intensity. The third peak, $(426)_H$, observed in Fig. 10a is shown to be clearly present when the isolated $(110)_A$ peak is rationalized in terms of $(110)_A$ and $(4\ 2\ 6)_H$ and $(0\ 0\ 12)_H$ reflections, as shown in Fig. 11b. Thus, the indexing of H-phase peaks,

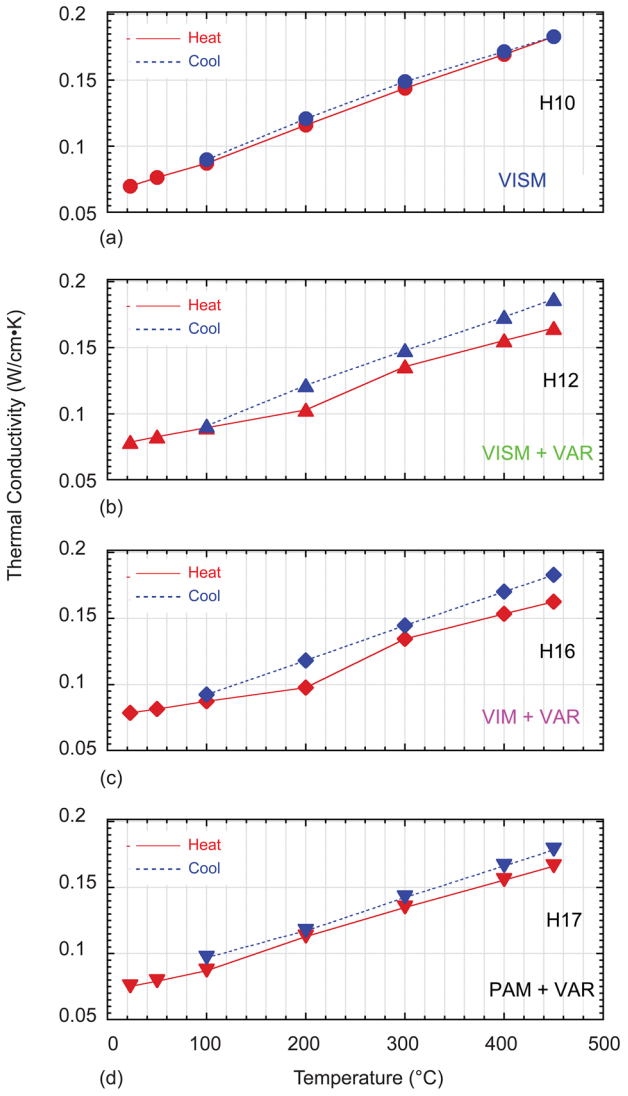

Fig. 17 Thermal conductivity as a function of temperature for various alloys in the as-extruded condition. **a** Alloy H10, **b** alloy H12, **c** alloy H16, and **d** alloy H17

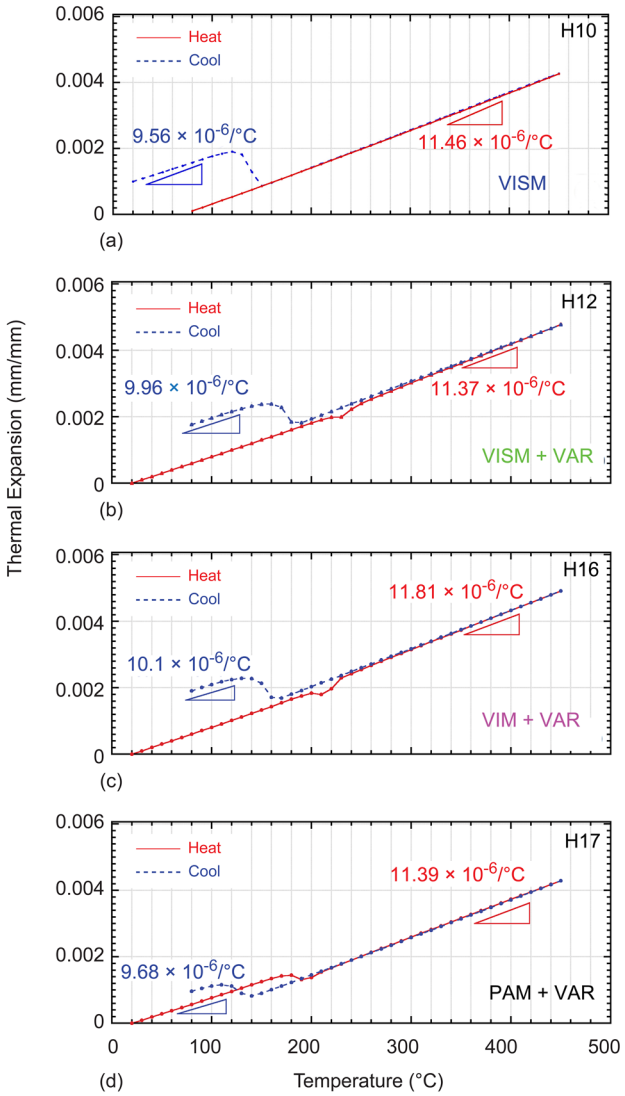

Fig. 18 Thermal expansion as a function of temperature for various alloys in the as-extruded condition. **a** Alloy H10, **b** alloy H12, **c** alloy H16, and **d** alloy H17

although small and broad in Fig. 10a, b, is authentic and confirms the presence of H-phase after aging using X-ray analysis.

Lattice parameters calculated from the X-ray patterns at room and high temperature corresponding to each alloy are shown in Table 3 and plotted in Fig. 12 as a function of heat number. Whole pattern fitting was performed using the Pawley method [50] as implemented in the Bruker TOPAS analysis program using a B19′ and B2 structure with the $P2_1/m$ and $Pm\text{-}3m$ space group, respectively. In room-temperature scans, the H-phase and secondary phases such as oxides and carbides were also accounted for when present. The H-phase was modeled as a single peak, except for the H5 heavily precipitated B2 alloy, which was fitted using the *Fddd* space group with starting lattice parameters from the literature [14]. Lattice parameters corresponding to these secondary phases are also included in Table 4. For high-temperature scans, only the austenite phase was modeled as the peaks for all other phases were very small and well separated from the austenite peaks. Overall, no major correlation between processing path and/or measured composition and lattice parameters was observed except for the H4 and H5 alloys with the highest Ni content, which deviated significantly from the rest of the alloys (for example, smaller a_0 (Fig. 12e)).

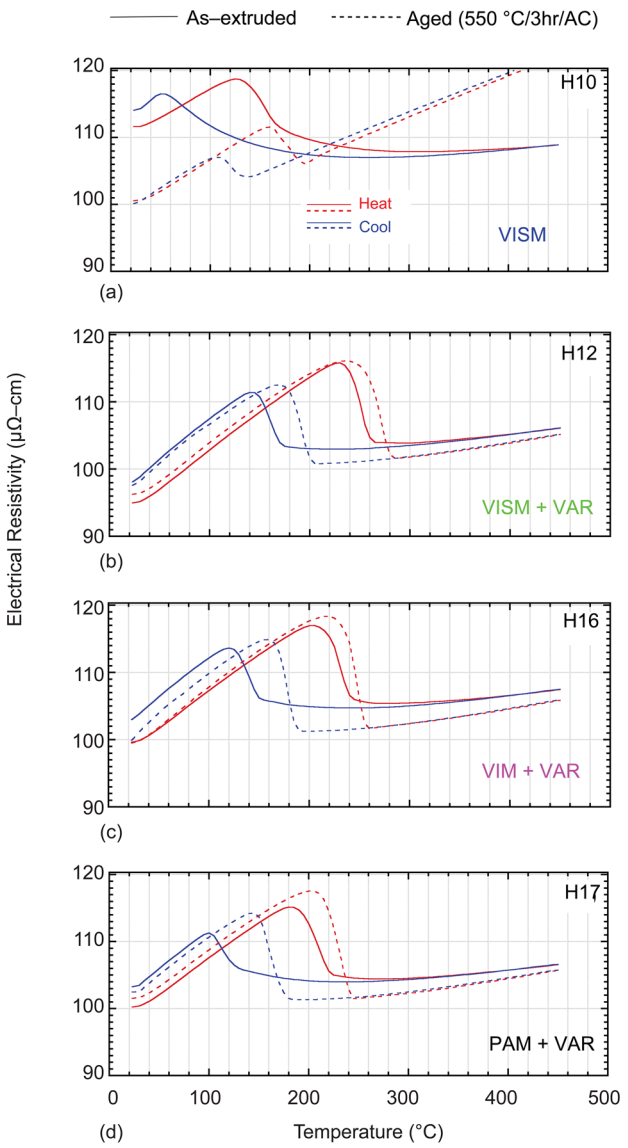

Fig. 19 Electrical resistivity as a function of temperature for various alloys in the as-extruded and aged condition. **a** Alloy H10, **b** alloy H12, **c** alloy H16, and **d** alloy H17

Microindentation Hardness

Figure 13 shows the average Vickers hardness values for the as-extruded and aged alloys as a function of heat number (Fig. 13a). The melting process did not have a discernible influence on the material hardness, showing an average value of ~ 365 HV (max: 382, min: 353) across the as-extruded heats, except for heats H4 and H5. The average hardness values were 505 and 620 for heats H4 and H5, respectively. Because these measurements were conducted at room temperature, all of the other alloys were a single-phase B19′ martensite, whereas heat H4 consisted of multiple phases (B2, B19′, and small amounts of H-phase), and heat H5 consisted of B2 and large amounts of H-phase (refer to Fig. 7). As a result, the higher hardness in these two alloys can be attributed to the presence of B2 and H-phase precipitates.

After aging, an evident increase in hardness was obtained, attributed to precipitation strengthening by the H-phase. Heat H7 did not exhibit similar behavior as this alloy is Ti-rich and did not form the H-phase or any precipitates after aging. Alloy H13 also exhibited essentially no hardness increase with aging, attributed to the very low volume fraction of H-phase in this material (Fig. 8g).

Thermophysical Properties

Density

Representative densities corresponding to alloys from each melting technique are summarized in Fig. 14. For each alloy, the density was measured ten times on the same sample, and the average of these values with the standard deviation are shown along with the corresponding heat number. Taking into account the standard deviation plotted as the error bars, it can be concluded that all the alloys showed comparable densities, and the small differences in the alloy chemistries had negligible effect on density.

Thermal Diffusivity

Thermal diffusivity, which describes the rate of temperature spread through the material, was measured in four different alloys, as shown in Fig. 15. Samples were heated to a given temperature in the range from 23 to 450 °C and held until reaching stabilization at that specific temperature. Similar measurements were also taken during cooling at the matching temperature points. It is shown that thermal diffusivity increased with temperature and the rate of change was different in the austenite phase (7.5×10^{-5} cm^2/s/°C) compared to the martensite phase (3.5×10^{-5} cm^2/s/°C). Thermal diffusivity was 0.026–0.03 and 0.056–0.06 cm^2/s at room temperature and 450 °C, respectively. The small deviation between the samples, seen in Fig. 15, can be attributed to small microstructural changes in the different heats or scatter in the measurements [51].

Specific Heat Capacity

Specific heat capacity results during heating and cooling at a rate of 20 °C/min, for both the as-extruded and aged conditions are shown in Fig. 16. The specific heat was constant in the single-phase martensite, showed a spike when the martensite transformed to austenite due to the absorption of latent heat during the endothermic process, and then returned to approximately the same level in the single-phase

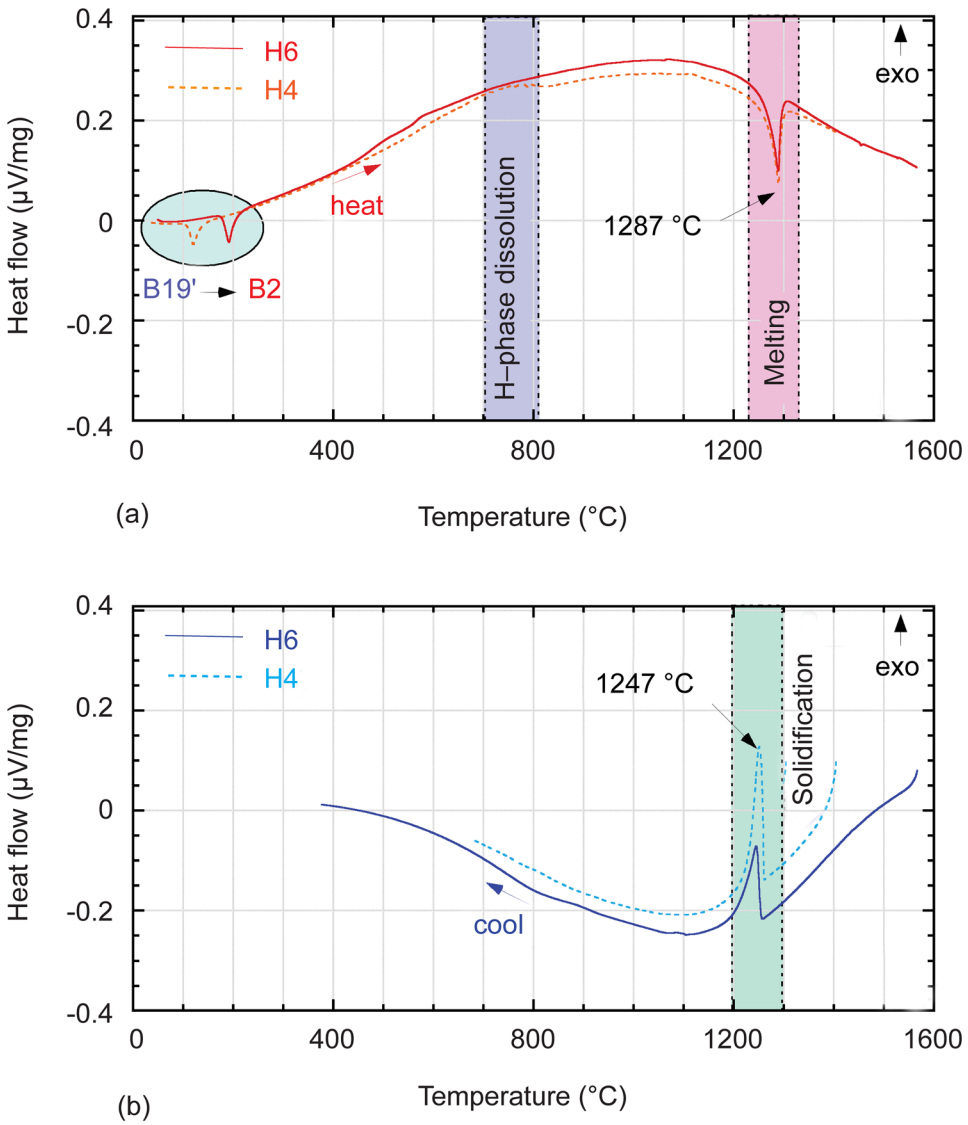

Fig. 20 Differential thermal analysis (DTA) data for alloys H4 and H6 in the as-extruded condition up to ~ 1600 °C. **a** Peaks at 120–200 °C correspond to B19′-to-B2 transition, peak at ~ 770 °C corresponds to H-phase dissolution, and peaks at ~ 1287 °C correspond to melting. **b** Peaks at ~ 1247 °C correspond to solidification

austenite region as it was in the single-phase martensite. Thus, the average heat capacity in the as-extruded condition was essentially constant outside the transformation region, at 0.36 J/g × K and ~ 0.35 J/g × K at 23 °C (martensite) and above 300 °C (austenite), respectively. These values are consistent with other reported values on binary polycrystalline NiTi [52] and single crystal NiTi alloys [53]. Outside of the transformation range, aging did not have a meaningful effect except in the case of the H10 alloy, which showed a difference of 0.1 J/g × K between the as-extruded and aged condition (Fig. 16a).

Thermal Conductivity

Density, thermal diffusivity, and specific heat were used to calculate the thermal conductivity following Eq. 1, and the results are shown in Fig. 17. Heat capacity values were obtained by a linear interpolation between specific heat values measured just before and after the peak. Thermal conductivities, measured on the heating curve, were found to be an average of 0.075 W/cm K at 23 °C (martensite) and 0.169 W/cm K at 450° (austenite) and followed a linear trend with temperature when not in the middle of the transformation. Comparable properties have been observed for binary NiTi [54, 55], NiTi-Cu [56], and high Ni-rich alloys [57].

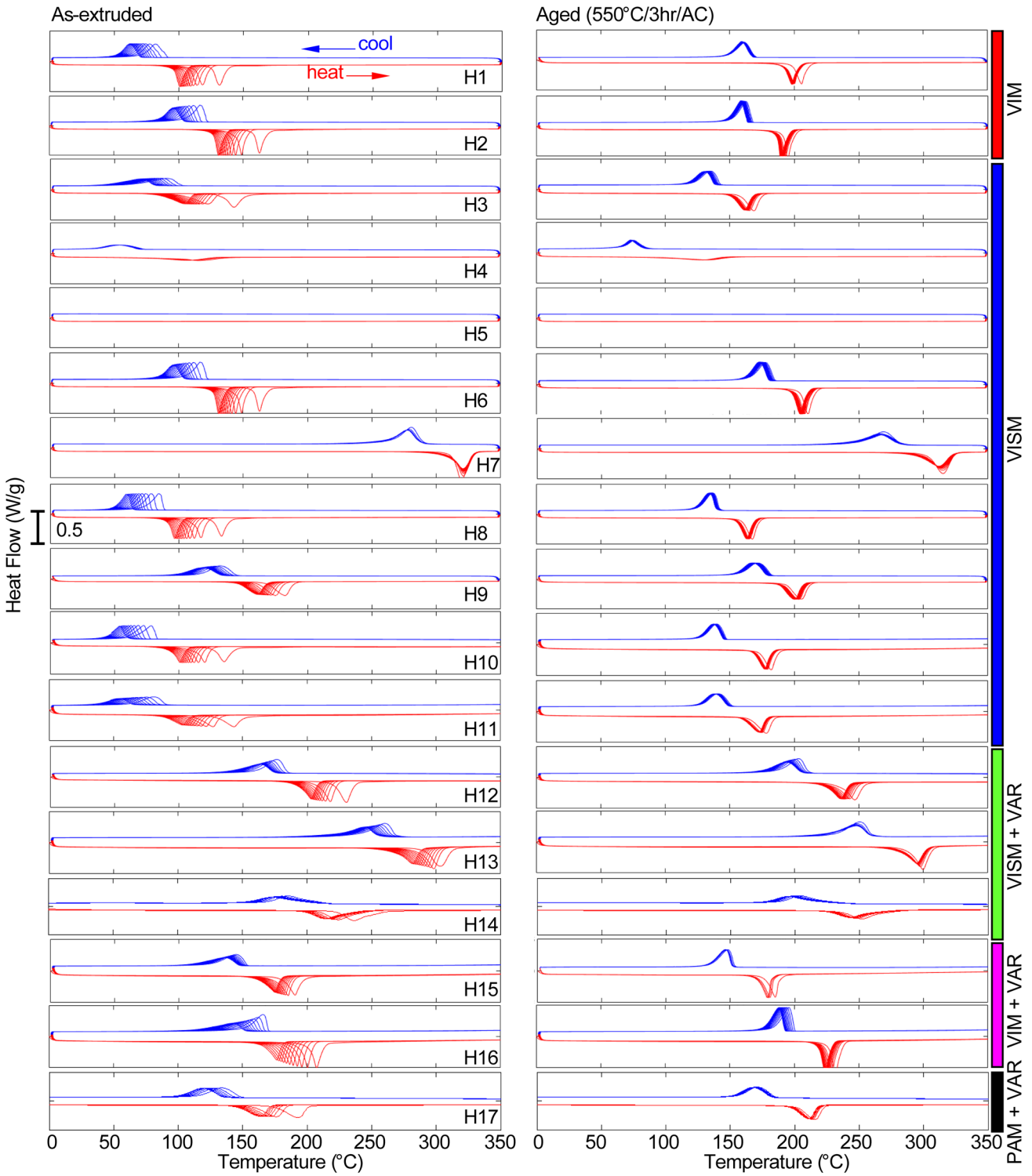

Fig. 21 Differential scanning calorimetry (DSC) measurements for all alloys in the as-extruded (*left*) and aged conditions (*right*). All ten thermal cycles are shown for each alloy

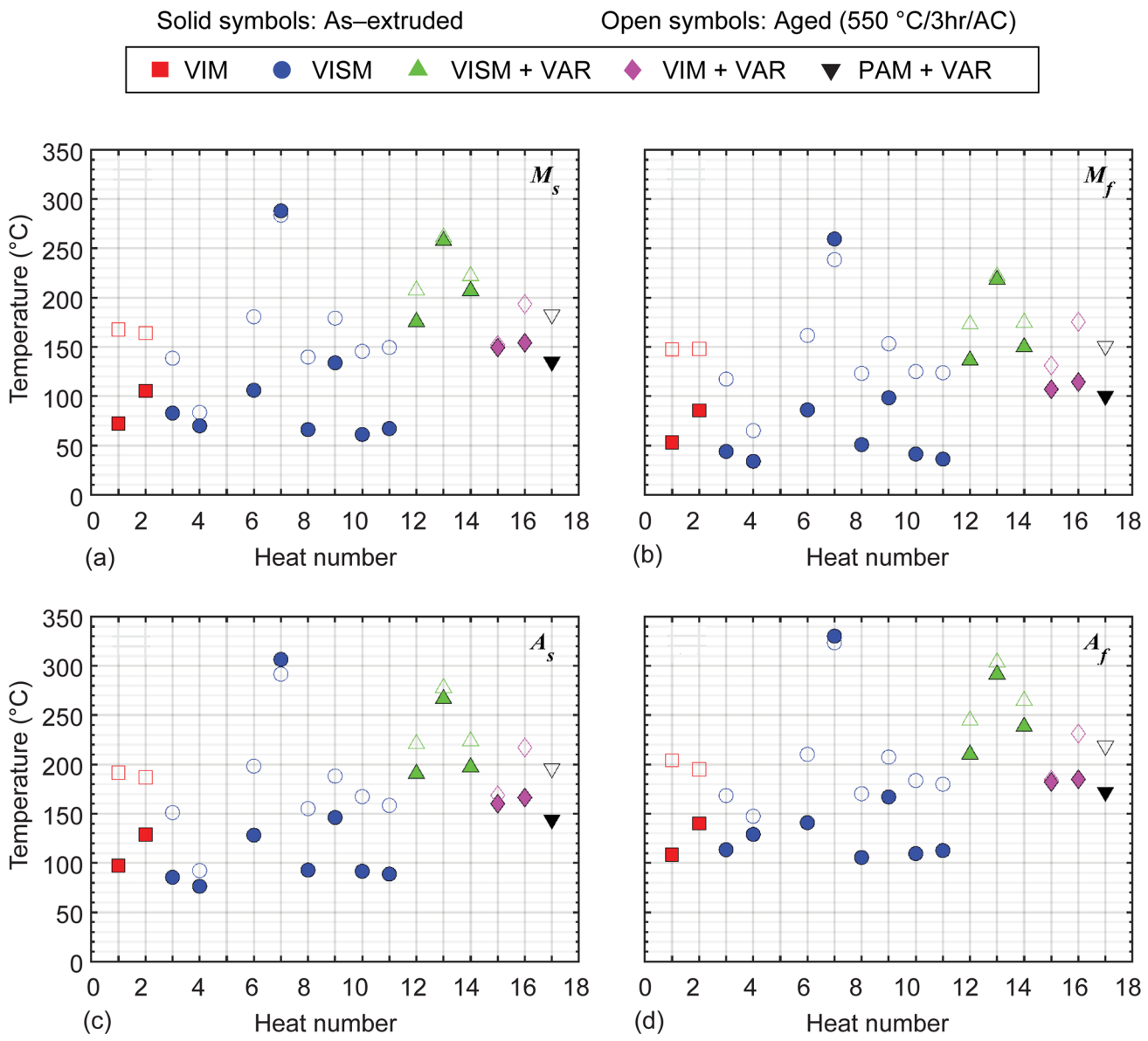

Fig. 22 Characteristic transformation temperatures for **a** martensite start (M_s), **b** martensite finish (M_f), **c** austenite start (A_s), and **d** austenite finish (A_f) corresponding to the last thermal cycle of the differential scanning calorimetry (DSC) data. The as-extruded (*solid symbols*) and aged conditions (*open symbols*) are shown as a function of heat number. The process types are *1* vacuum induction melting (VIM *filled red square, open red square*), *2* vacuum induction skull melting (VISM *filled blue circle, open blue circle*), *3* vacuum induction skull melting + vacuum arc remelting (VISM + VAR *filled green triangle, open green triangle*), *4* VIM + VAR *filled pink diamond, open pink diamond*, and *5* plasma arc melting + vacuum arc remelting (PAM + VAR *filled inverted black triangle, open black inverted triangle*) (Color figure online)

Thermal Expansion

Linear thermal expansion measurements in the as-extruded condition are shown in Fig. 18. The slopes measured in both martensite and austenite regions show a consistent coefficient of thermal expansion (CTE) of 9.5–10.1 × 10^{-6}/°C and 11.4–11.8 × 10^{-6}/°C in the low- and high-temperature regions, respectively. The austenite CTE is consistent with previously reported measurements for $Ni_{50.3}Ti_{29.7}Hf_{20}$ using extensometer data from a stress-free strain-temperature response [23], but the martensite CTE is slightly different from previous works. While the differences in the measurement techniques can play a role in these discrepancies, the more significant contributor is martensite texture that can yield certain directions that have positive, zero, or even negative CTE values [58–60]. In the current study, different melting techniques followed by extrusion resulted in very

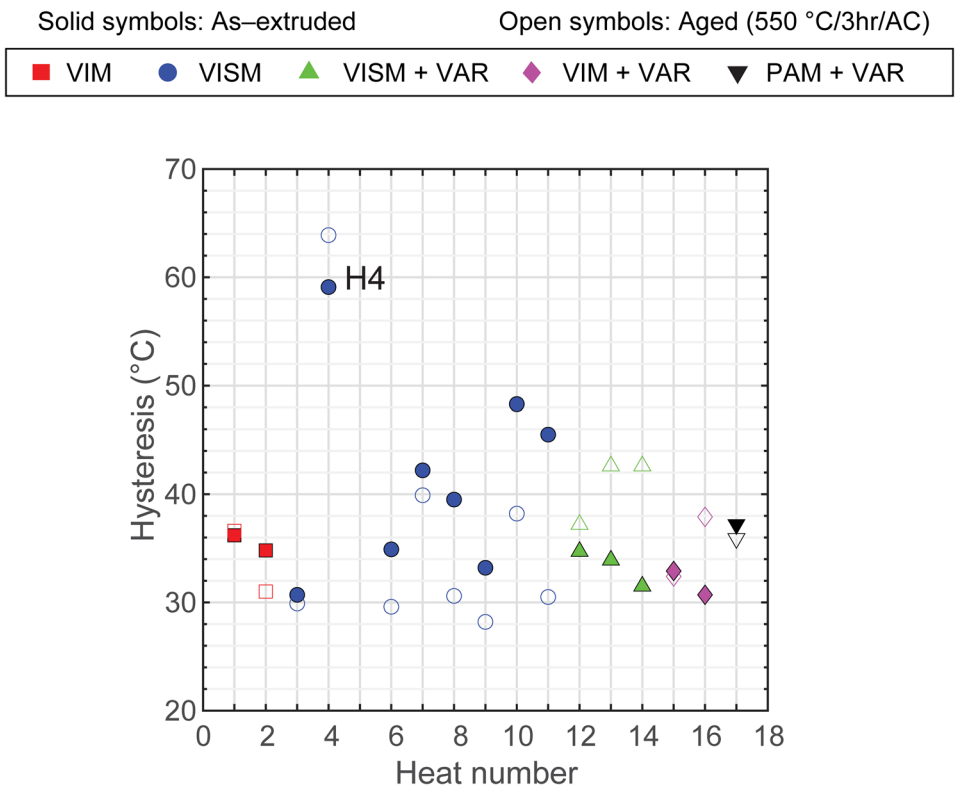

Fig. 23 Thermal hysteresis as a function of heat number defined as the austenite finish minus martensite start ($A_f - M_s$) from differential scanning calorimetry (DSC). The as-extruded (*solid symbols*) and aged conditions (*open symbols*) are shown as a function of no. of heat. The process types are *1* vacuum induction melting (VIM *filled red square, open red square*), *2* vacuum induction skull melting (VISM *filled blue circle, open blue circle*), *3* vacuum induction skull melting + vacuum arc remelting (VISM + VAR *filled green triangle, open green triangle*), *4* VIM + VAR *filled pink diamond, open pink diamond*, and *5* plasma arc melting + vacuum arc remelting (PAM + VAR *filled inverted black triangle, open black inverted triangle*)

comparable outcomes using either the heating or cooling curves.

Electrical Resistivity

Electrical resistivity measurements obtained during heating and cooling are shown in Fig. 19 for the as-extruded and aged conditions. On average, resistivity values were 99 and 105 μΩ-cm measured at 23 and 450 °C, respectively. During transformation, values as high as 118 μΩ-cm were recorded in the two-phase region.

Melting Temperature

The melting point of this alloy composition was measured using a differential thermal analysis technique, as shown in Fig. 20. On initial heating, two peaks were visible around 120 and 200 °C, corresponding to the B19′-to-B2 transition for as-extruded alloys H4 and H6, respectively. At approximately 770 °C, there was a broad peak visible in the H4 alloy but not in the H6. Recalling that alloy H4 contained H-phase precipitates in the as-extruded condition, this peak is attributed to H-phase dissolution, consistent with DSC data from other studies [61]. Finally, the largest peak was observed at 1287 °C for both alloys (and others not shown here), corresponding to the melting point. On cooling, the solidification peak occurred at 1247 °C.

Differential Scanning Calorimetry (DSC)

DSC measurements are shown in Fig. 21 for all the alloys in the as-extruded and aged conditions. As expected from the variation in Ni content, the transformation temperatures vary according to the actual composition of the alloy. For a given alloy in the as-extruded condition, the thermal response was shown to drift to lower temperatures as a function of cycles at a decreasing rate with a tendency to reach stabilization (up to the tenth cycle). In the as-extruded condition, alloys H4 and H7 exhibited the best thermal stability due to the presence of H-phase precipitates and the Ti-rich matrix, respectively.

After aging, two major effects were observed consistent with most alloys. First, the transformation temperatures shifted to higher temperatures. Second, concurrent with the shift to higher transformation temperatures, aging was shown to stabilize the thermal response, where there was little to no drift in the transformation temperature peaks for all ten thermal cycles. Both effects are attributed to the presence of the nanometer-sized H-phase precipitates. The precipitates provide additional strengthening to the alloy, reducing or eliminating the plastic deformation associated with each thermal cycle that contributes to the decreasing peak temperature with cycling. They also account for Ni-depletion in the matrix [14], raising the transformation temperatures over the precipitate-free condition. Hence, the thermal response

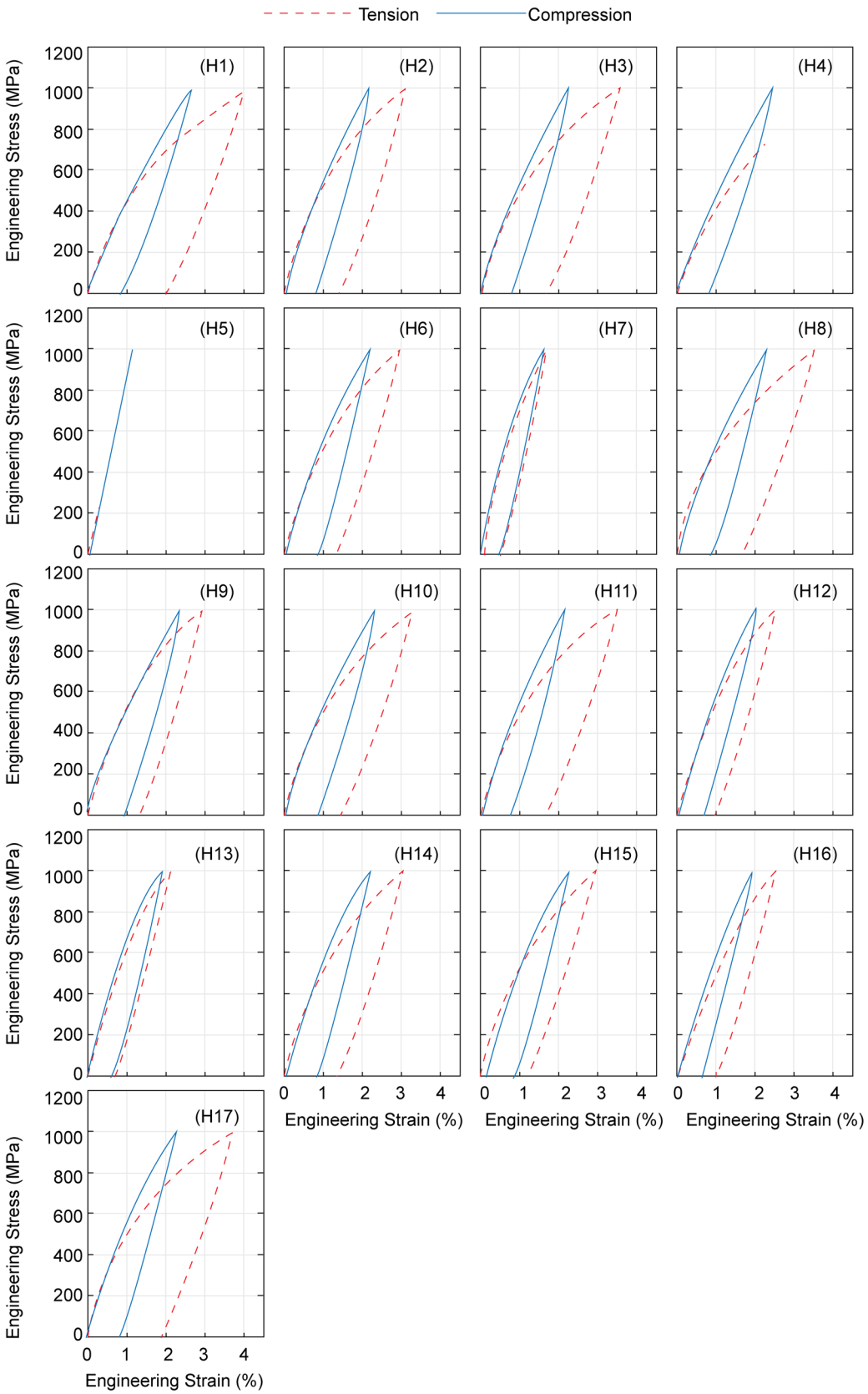

Fig. 24 Room-temperature stress–strain responses in tension and compression for all alloys aged at 550 °C for 3 h and air cooled

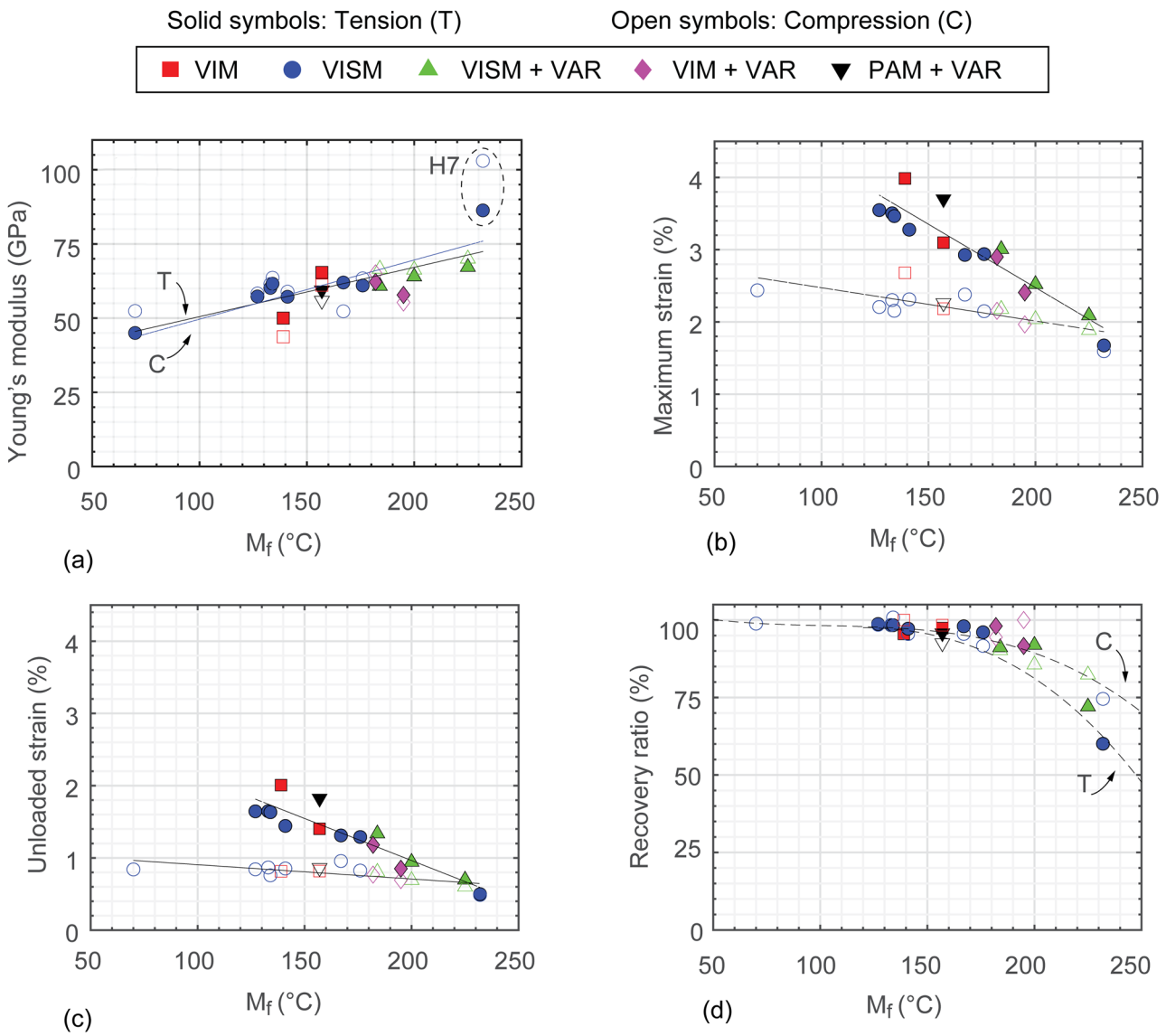

Fig. 25 Room-temperature isothermal data as a function of M_f for alloys aged at 550 °C for 3 h and air cooled in tension (*solid symbols*) and compression (*open symbols*). **a** Young's modulus, **b** the maximum loading strain (strain at the highest stress of 1 GPa or failure), **c** unloaded strain (strain after unloading to 0 MPa), and **d** recovery ratio (percent strain recovered after heating and cooling. The process types are *1* vacuum induction melting (VIM *filled red square, open red square*), *2* vacuum induction skull melting (VISM *filled blue circle, open blue circle*), *3* vacuum induction skull melting + vacuum arc remelting (VISM + VAR *filled green triangle, open green triangle*), *4* VIM + VAR *filled pink diamond, open pink diamond*, and *5* plasma arc melting + vacuum arc remelting (PAM + VAR *filled inverted black triangle, open black inverted triangle*) (Color figure online)

is more stable and the material exhibits higher actuation temperatures. The one exception was alloy H7, where no major differences in the DSC response were observed after heat treatment, as the alloy was Ti-rich and did not form precipitates during aging.

The characteristic transformation temperatures for martensite start (M_s), martensite finish (M_f), austenite start (A_s), and austenite finish (A_f) corresponding to the last thermal cycle are shown in Fig. 22. The thermal hysteresis as a function of heat number is shown in Fig. 23. The hysteresis in this work is defined as the austenite finish minus the martensite start ($A_f - M_s$). It is shown that the lowest hysteresis obtained was 28 °C corresponding to the aged alloy H9, whereas the highest was 64 °C for the aged alloy H4. The majority of the data were clustered around a hysteresis between 30 and 40 °C, and no major trend in hysteresis was clearly delineated between the aged and as-extruded conditions.

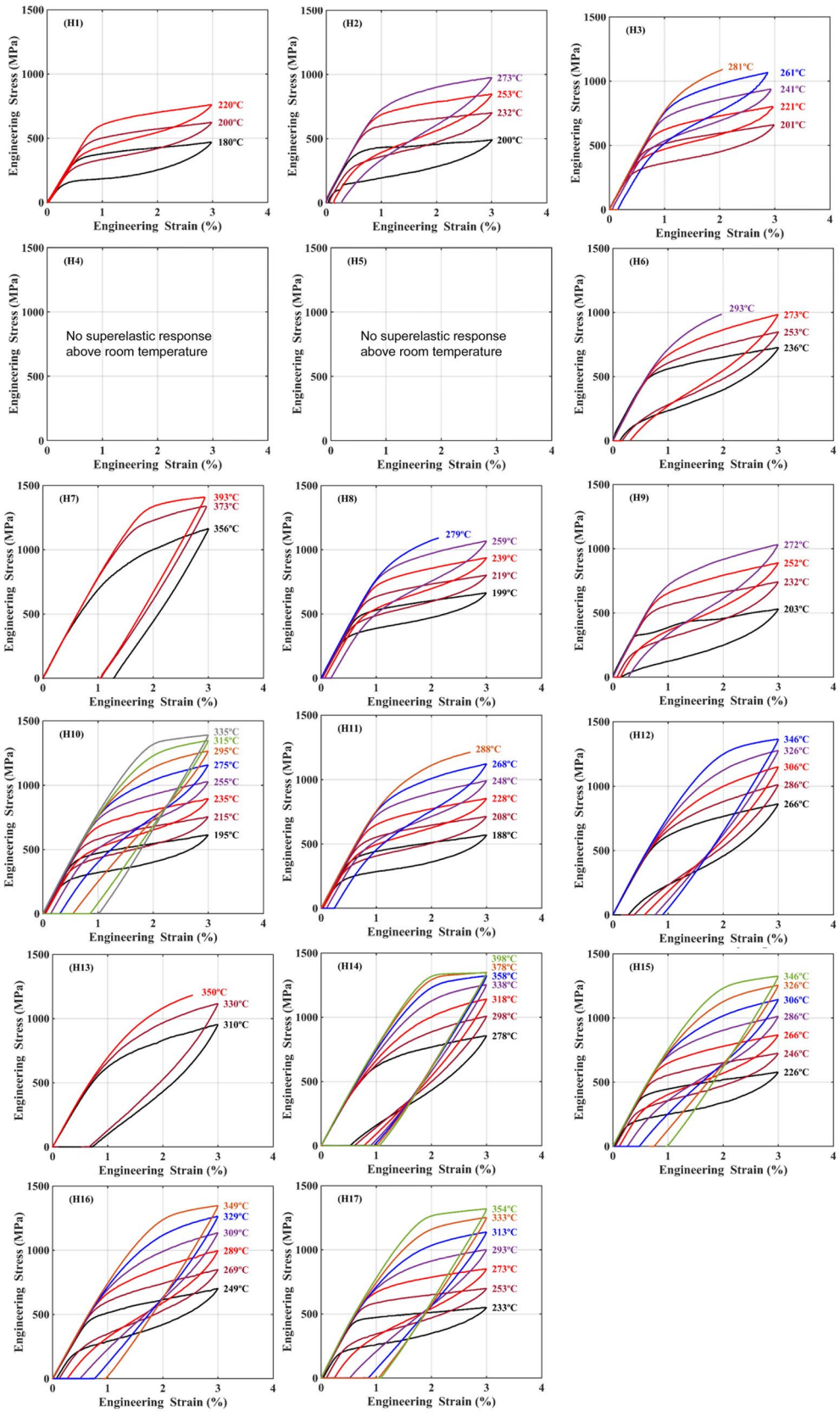

Fig. 26 High-temperature stress–strain responses in tension for alloys aged at 550 °C for 3 h and air cooled. All tests performed at temperatures above A_f

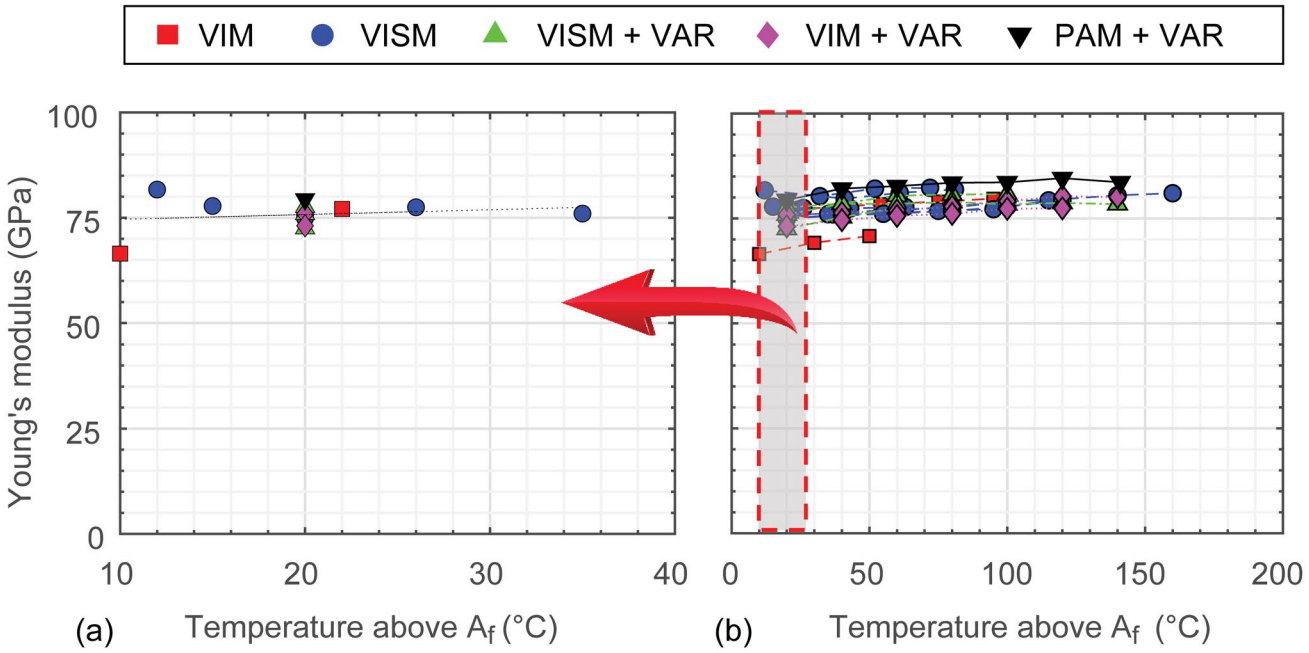

Fig. 27 Young's modulus in tension as a function of test temperature above A_f for alloys aged at 550 °C for 3 h and air cooled. **a** Moduli at test temperatures in the range of 10–35 °C above A_f, and **b** moduli at incremental test temperatures above A_f. The process types are *1* vacuum induction melting (VIM *filled red square*), *2* vacuum induction skull melting (VISM *filled blue circle*), *3* vacuum induction skull melting + vacuum arc remelting (VISM + VAR *filled green triangle*), *4* VIM + VAR *filled pink diamond*, and *5* plasma arc melting + vacuum arc remelting (PAM + VAR *filled inverted black triangle*) (Color figure online)

Isothermal Deformation

The room-temperature stress–strain responses for all heats in the aged condition are shown in Fig. 24. Each alloy was deformed in uniaxial tension and compression to 1 GPa (or, in the case of samples H4 and H5, until failure in tension), followed by unloading to 0 MPa, heating to 350 °C, and finally cooling to room temperature. Additional details about this test procedure can be found in the standard test method for mechanical uniaxial pre-strain and thermal-free recovery of shape memory alloys (ASTM E3098-17) [36]. The accumulated strains are a combination of elastic deformation, martensite variant reorientation, and detwinning, but no clear stress plateau, such as that typically seen in binary NiTi alloys, or demarcation between the two mechanisms can be observed. The hardening behavior differs from alloy to alloy and can be largely attributed to two effects: the compositional differences between alloys, and the test temperature with respect to the martensite start temperature. The compositional difference affects yield stress and the critical resolved shear stress for slip by strengthening of the material through solid solution and precipitation hardening. In the martensite, at a consistent temperature offset from the transformation, a stronger material will have a higher yield stress. However, if the critical resolved shear stress for slip is lower than or close to the critical stress for martensite detwinning or reorientation, the material will tend to yield via plasticity, in addition to recoverable twin processes [62]. Additionally, as in this case, when all the alloys were deformed at room temperature (average of 24 °C), the temperature difference between the M_f and the test temperature can change the hardening behavior, through an increase in Young's modulus and yield stress as the distance below the

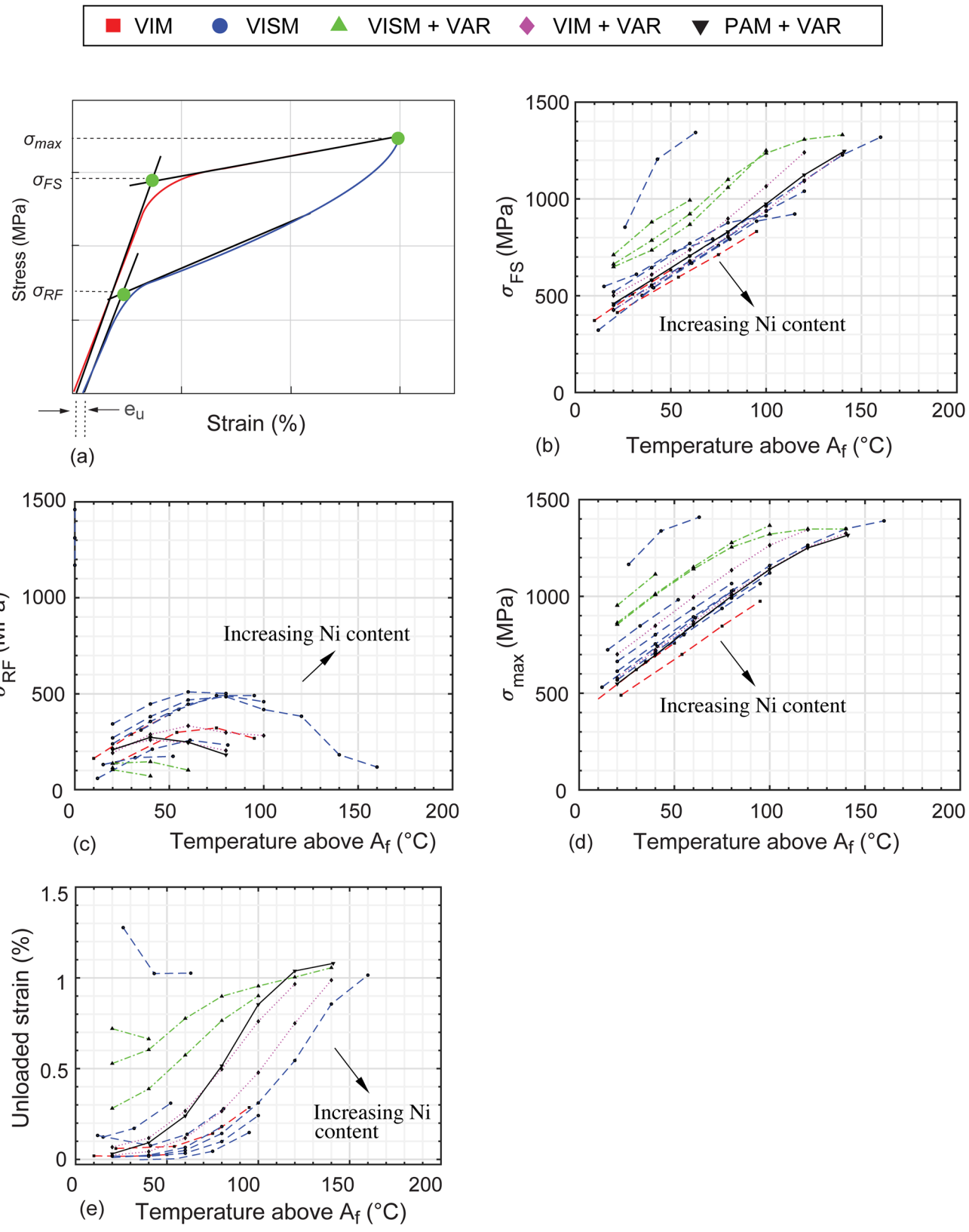

Fig. 28 High-temperature isothermal data as a function of temperatures above A_f for alloys aged at 550 °C for 3 h and air cooled in tension. **a** Graphical representation of the reported variables, **b** the onset stress of the forward transformation start (σ_{FS}), **c** the stress of the reverse transformation finish (σ_{RF}), **d** stress at the maximum loading strain of 3% (σ_{max}), and **e** the unloaded strain (strain after unloading to 0 MPa)

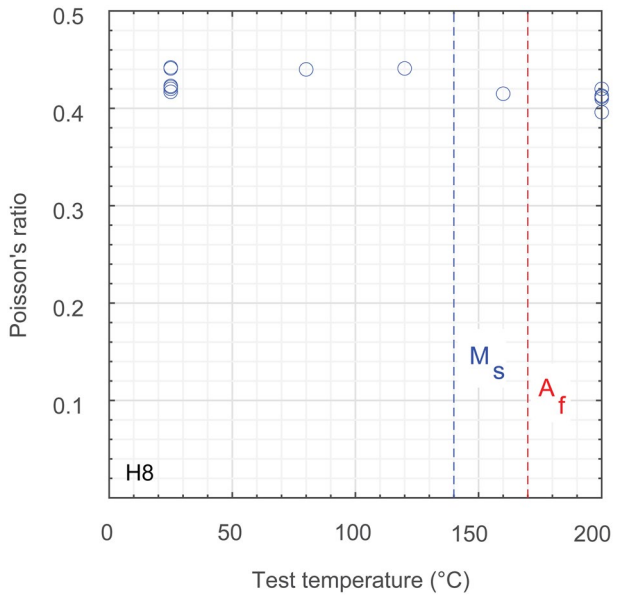

Fig. 29 Poisson's ratio measured at several temperatures with 100 MPa stress applied in tension

transformation temperature increases, as demonstrated in Fig. 25a and as previously shown in [63–65].

The apparent elastic loading portion of the stress–strain curves was linearly fitted up to 300 MPa to obtain the elastic moduli in tension and compression, and the results are shown in Fig. 25a. The reported values are expected to yield a "deflated" modulus, as compared with the true martensite modulus, possibly due to contributions from early detwinning and/or reorientation as seen in similar alloys [66, 67]. In Fig. 25a, the apparent elastic moduli are plotted as a function of martensite finish temperature (M_f) measured from a stress-free thermal cycle performed on the sample in the test frame before room-temperature testing. The moduli range from 45 to 86 GPa, with a weak trend suggesting that the modulus increased with increasing M_f temperature. Or conversely, the modulus decreased as the testing temperature approached the M_f for the alloy [63]. It is noted that the Ti-rich alloy H7 was excluded from the trend line fit, since the material was not comparable to the other alloys microstructurally and does not represent an analogous martensitic modulus. No significant differences were observed in moduli determined in tension and compression, again with the exception of alloy H7.

To shed more light on the isothermal behavior of NiTiHf, particular data pertinent to the isothermal responses are shown in Fig. 25b–d. These data include the maximum loading strain (strain at the highest stress of 1 GPa or failure), unload strain (strain after unloading to 0 MPa), and recovery ratio (percent strain recovered after heating up to 350 °C and cooling to room temperature). Similar to the elastic moduli, the data are plotted as a function of the martensite finish temperature (M_f). For lower M_f, alloys exhibited higher maximum (Fig. 25b) and unloaded strains (Fig. 25c) in both testing modes, as highlighted by the superimposed trend lines. It is noted here that the trend lines are not necessarily the best correlation fits through the data, but merely a linear fit to help visualize the data trends. The higher strains in these alloys are due to easier detwinning and reorientation of the martensite at test temperatures close to the M_f, and to higher resistance to slip from solid solution and precipitation strengthening, which favors reversible twinning modes over plastic deformation. The maximum (Fig. 25b) and unloaded strains (Fig. 25c) are lower in compression compared to tension. This arises from the tension–compression asymmetry, which is attributed to differences in martensitic variant selection in tension versus compression in NiTi alloys [68]. The asymmetry, better discerned from the stress–strain responses of Fig. 24, stems from the higher number of active twinning modes in tension than compression, along with limited strain generation associated with the compressive variants [67]. As a result, the strain hardening behavior manifests differently in the two deformation modes. However, in the alloys with higher transformation temperatures (i.e., lower Ni content), there is less tension–compression anisotropy because these twinning modes are not being activated during the isothermal test. Rather, the deformation is occurring due to dislocation slip, which behaves similarly in tension and compression.

It is also anticipated that slip or deformation twinning can be activated along with the reversible twinning processes [68]. If strains are fully recovered after heating and cooling at nominally zero stress (after unloading), then it is confirmed that only reversible twinning modes (mainly martensite reorientation and detwinning) were activated. If, however, some residual strains exist after the thermal cycle, it is then assumed that some level of plasticity occurred. It can be seen that, while the magnitude of the residual strain (Fig. 25d) was highest in the alloys with lower M_f, these alloys had up to 100% recovery after the unloaded thermal cycle (i.e., all deformation was due to reversible twinning modes), in agreement with similar studies [23]. This is in contrast to the much lower recovery ratios (i.e., higher plastic deformation) for the alloys with higher M_f.

Isothermal tensile tests were performed on the aged materials at temperatures above the austenite finish temperature to assess the superelastic behavior. The stress–strain responses at the indicated test temperatures are shown in Fig. 26. Each alloy was deformed in uniaxial tension to 3% strain (or until failure), followed by unloading to 0 MPa. The same sample was then heated to the next temperature (at increments of 20 °C, nominally) and strained again to 3%. For easier comparison, all the curves were shifted to the plot origin at 0%, 0 MPa. The choice of test temperatures was

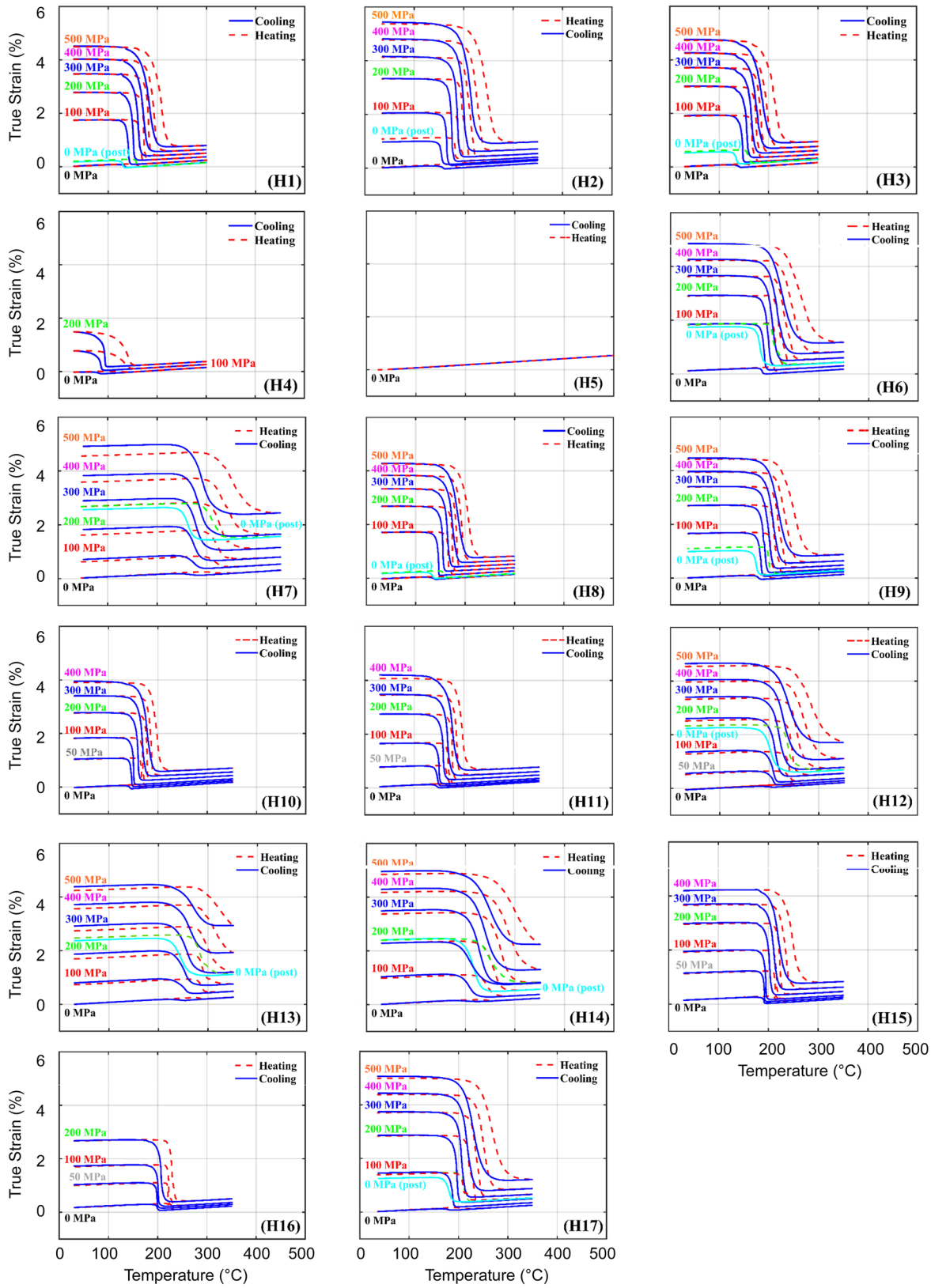

Fig. 30 Tensile constant force thermal cycling responses for alloys aged at 550 °C for 3 h and air cooled. Tests were performed in series and only the second cycle from each stress level is shown

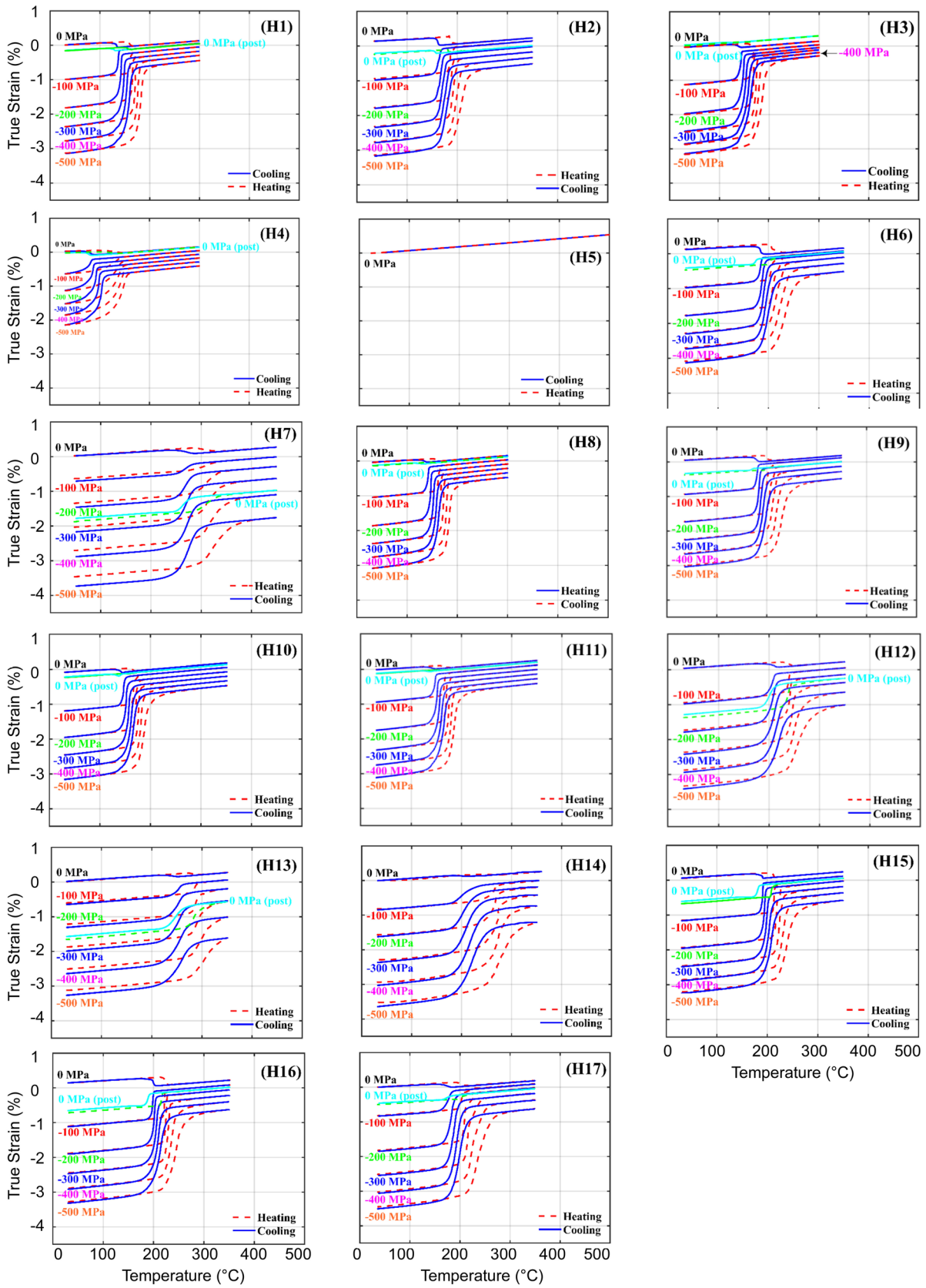

Fig. 31 Compressive constant force thermal cycling responses for alloys aged at 550 °C for 3 h and air cooled. Tests were performed in series and only the second cycle from each stress level is shown

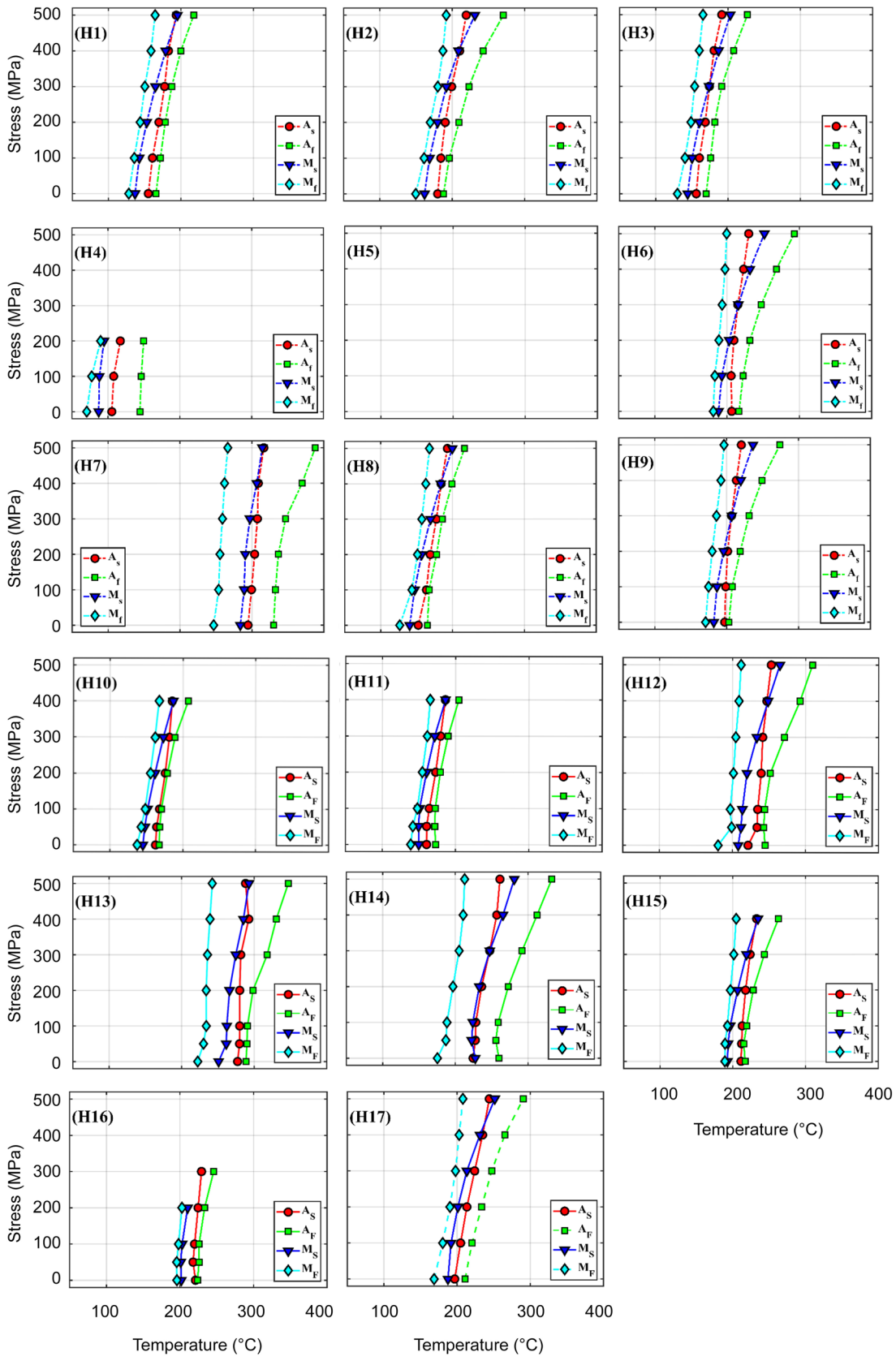

Fig. 32 Tensile characteristic transformation temperatures as a function of stress corresponding to the second thermal cycle from the constant force thermal data. Martensite start (M_s), martensite finish (M_f), austenite start (A_s), and austenite finish (A_f)

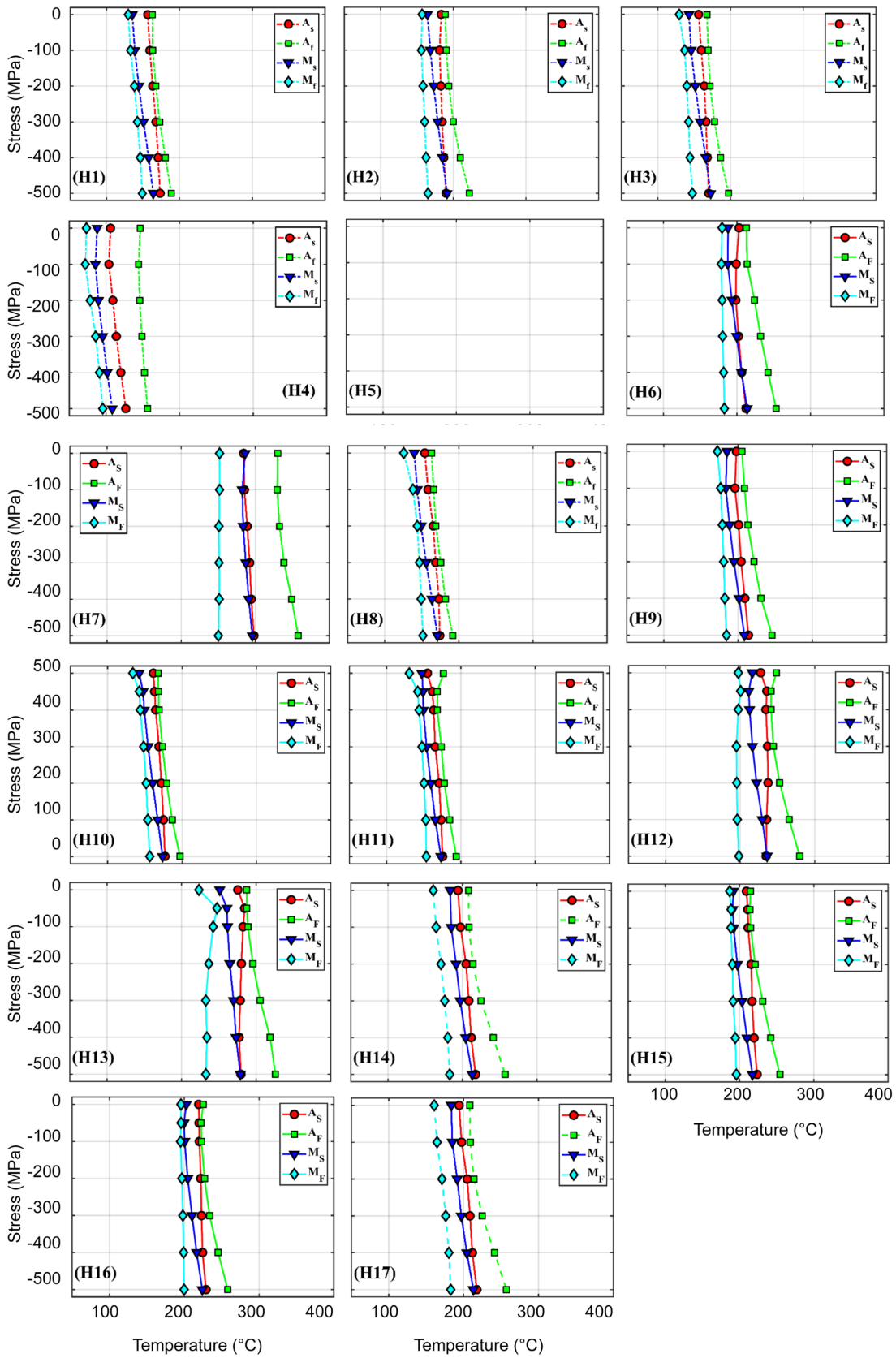

Fig. 33 Compressive characteristic transformation temperatures as a function of stress corresponding to the second thermal cycle from the constant force thermal data. Martensite start (M_s), martensite finish (M_f), austenite start (A_s), and austenite finish (A_f)

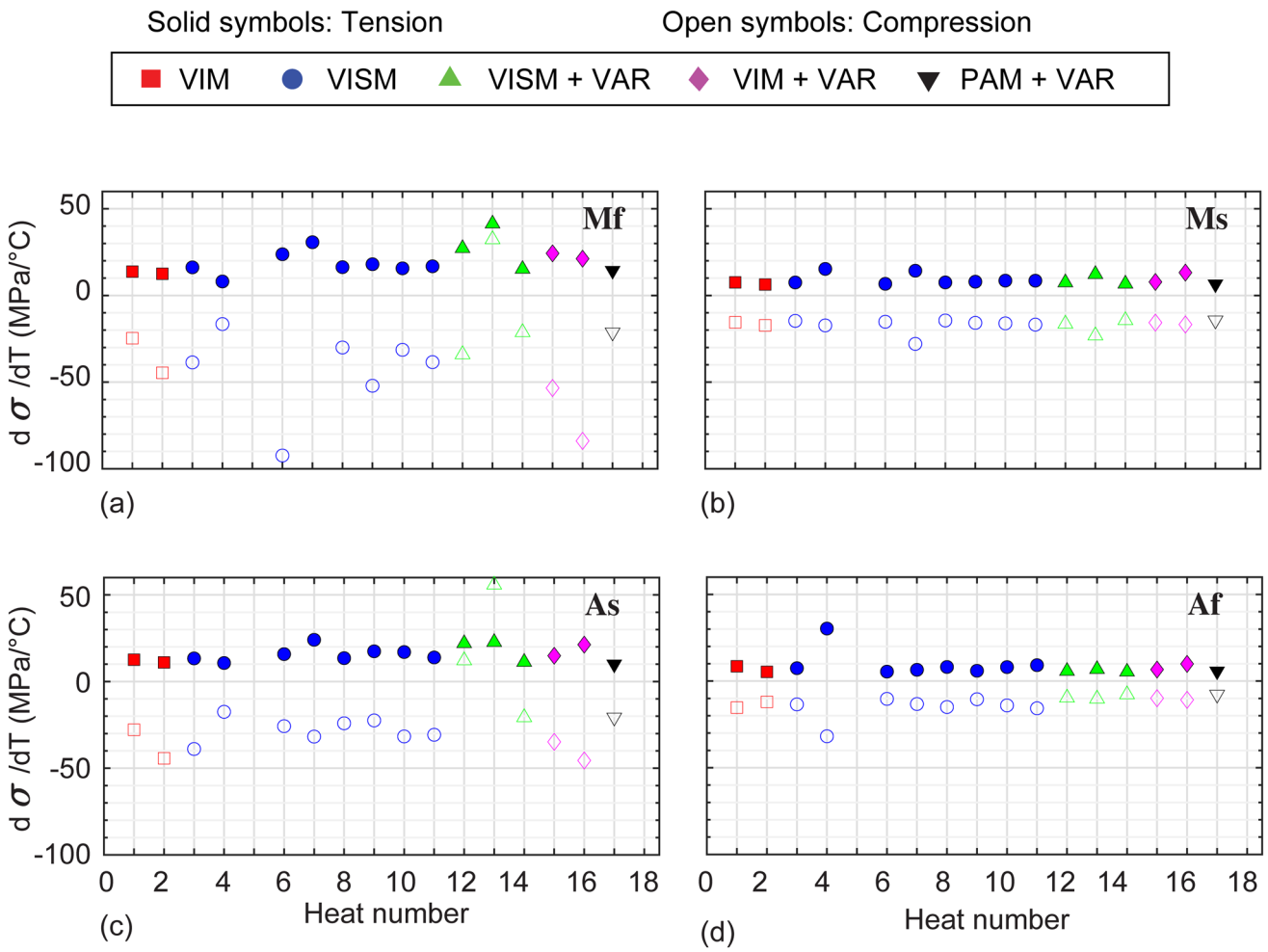

Fig. 34 Clausius–Clapeyron slopes ($d\sigma/dT$) for alloys aged at 550 °C for 3 h and air cooled, tested in tension (*solid symbols*) and compression (*open symbols*). **a** Martensite finish (M_f), **b** martensite start (M_s), **c** austenite start (A_s), and **d** austenite finish (A_f). The process types are *1* vacuum induction melting (VIM *filled red square, open red square*), *2* vacuum induction skull melting (VISM *filled blue circle, open blue circle*), *3* vacuum induction skull melting + vacuum arc remelting (VISM + VAR *filled green triangle, open green triangle*), *4* VIM + VAR *filled pink diamond, open pink diamond*, and *5* plasma arc melting + vacuum arc remelting (PAM + VAR *filled inverted black triangle, open black inverted triangle*) (Color figure online)

not random, but targeted to 10–30 °C above the austenite finish temperature (as measured from the original no-load thermal cycle performed on all samples prior to testing). For example, the lowest test temperature for alloy H17 in Fig. 26, 233 °C, corresponds to $A_f + 20$ °C for that particular alloy, followed by increments of 20 °C.

Unlike the martensite response, the austenite phase exhibited a distinctive linear elastic region, followed by the conventional inelastic "yield" response. For most shape memory alloys, this inelastic response is attributed to the onset of stress-induced martensite (SIM) on the forward transformation during loading, and reversal during the reverse transformation on unloading. In the case of Ti-rich alloy H7, the inelastic response is composed of SIM with significant contributions from plastic deformation mechanisms. The shape and magnitudes of the curves are also alloy dependent, giving rise to different stress plateau magnitudes, stress hysteresis, and residual strains.

The elastic region of each curve was used to compute the austenite elastic moduli, and the data are summarized in Fig. 27. In Fig. 27a, the modulus values were taken from the initial tests at temperatures just above but closest to A_f (10–35 °C above A_f). In Fig. 27b, the modulus of each successive test at higher temperatures is also included. The average modulus just above A_f was 75 GPa (max = 82 GPa, min = 67 GPa). Unlike the martensite phase, the austenite moduli are nearly identical, suggesting isotropic behavior. Thus, the anisotropic elastic response of the B19′ martensite [66] may be the reason for the larger variations in the martensite moduli observed in Fig. 25.

Other characteristic values from these high-temperature tensile tests were extracted from each curve and plotted in

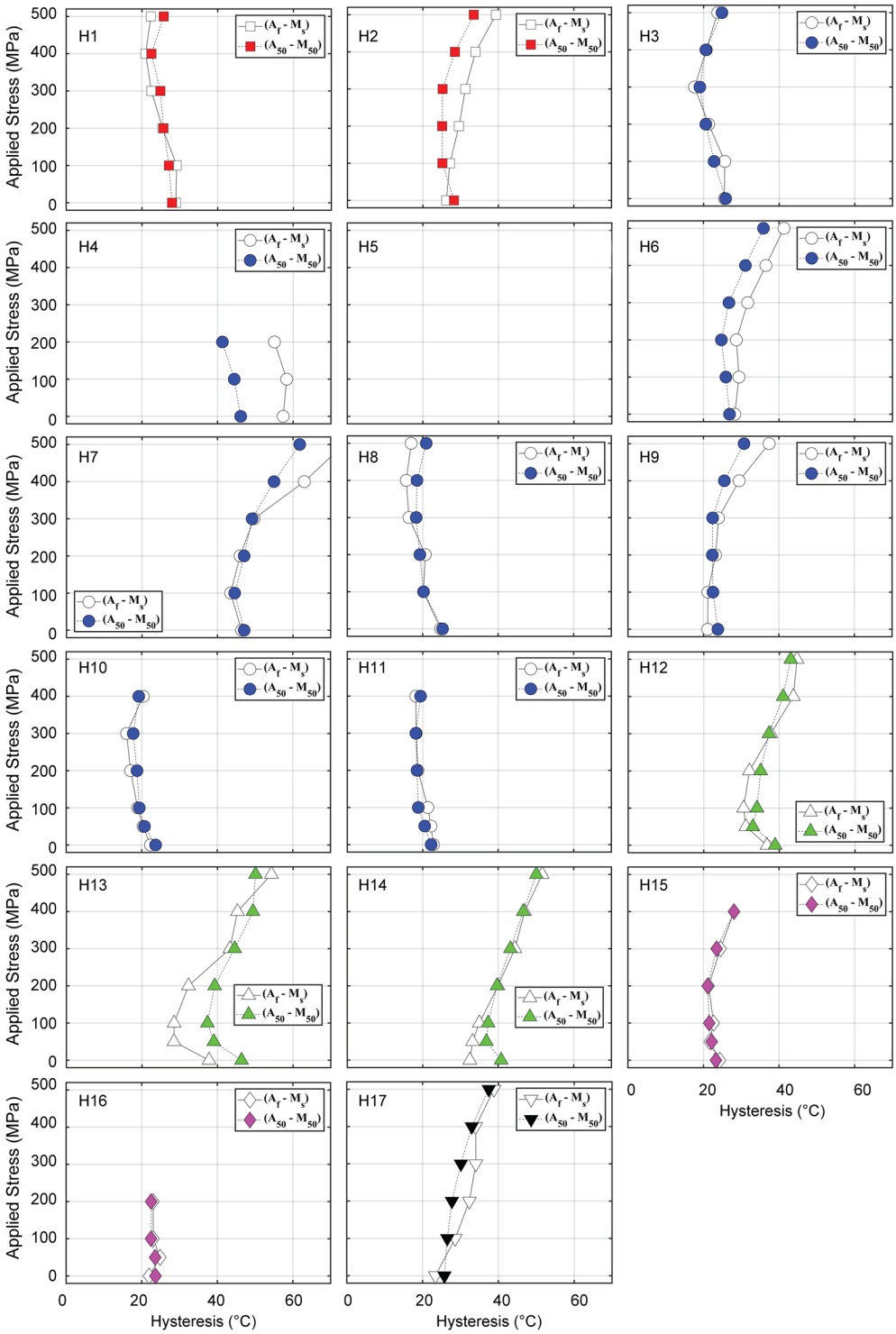

Fig. 35 Thermal hysteresis as a function of stress for alloys aged at 550 °C for 3 h and air cooled, tested in tension. The process types are *1* vacuum induction melting (VIM *filled red square, open red square*), *2* vacuum induction skull melting (VISM *filled blue circle, open blue circle*), *3* vacuum induction skull melting + vacuum arc remelting (VISM + VAR *filled green triangle, open green triangle*), *4* VIM + VAR *filled pink diamond, open pink diamond*, and *5* plasma arc melting + vacuum arc remelting (PAM + VAR *filled inverted black triangle, open black inverted triangle*) (Color figure online)

Fig. 28. The values are defined in Fig. 28a and include the onset stress of the forward transformation start (σ_{FS}), the stress of the reverse transformation finish (σ_{RF}), stress at the maximum loading strain of 3% (σ_{max}), and finally the unloaded strains (strain after unloading to 0 MPa, e_u). While scatter in the data are acknowledged, some trends can still be observed. The most obvious is that σ_{FS} (Fig. 28b) increases as a function of test temperature. It is understood from this observation that critical resolved shear stress for inducing martensitic transformation increases with increasing temperatures, as a higher stress is necessary to stress induce martensite at higher temperatures until the martensite desist temperature (M_d) is reached (i.e., temperature at which no SIM can form). Similarly, the maximum stress (Fig. 28d) follows the same trend.

The temperature dependence of the σ_{RF}, however, is a little more complicated. It generally increases, reaches a peak at 30–80 °C above the A_f temperature, followed by a decrease at higher test temperatures (Fig. 28c). Initially the increase follows the trend of the onset, but once the SIM mechanism is accompanied by plastic deformations, σ_{RF} starts to decrease. Testing at higher temperatures and ultimately approaching or even surpassing the M_d, the inflection point representing the end of martensite conversion back to austenite is less apparent and drops as plasticity becomes the dominant mechanism. A clear example of such effect is shown in Fig. 26 for alloy H17 tested at 354 °C, where the unloading curve is nearly linear until reaching ~ 150 MPa. This is in line with the unloaded strains (Fig. 28e), where at temperatures closest to A_f, the unloaded strains are near zero (i.e., fully reversible), followed by an increase once permanent deformation is imparted during straining at higher temperatures.

Poisson's ratio was measured using two sets of strain gages mounted 90° apart on a square dogbone specimen. Multiple isothermal tests were conducted on alloy H8 in the aged condition and the data are reported in Fig. 29. At room temperature (martensite), the sample was deformed up to 100 MPa (to stay within the pseudolinear portion of the curve), and the Poisson's ratio was 0.42. The same sample was heated to the next test temperature and reloaded again to the same stress level. The austenitic Poisson's ratio (at 200 °C) was 0.41, which is very close to the martensite value, and slightly higher compared to a previous study that reported a value of 0.39 [46]. Singh et al. [69] also reported a value of 0.41 using density functional theory (DFT). It should be noted that there is very limited data on the Poisson's ratio of NiTi [66, 70, 71], and even less data for NiTiHf, given the difficulty in making these measurements when there is interplay between multiple deformation mechanisms. For example, some reorientation is expected to occur even during loading to low stresses in the martensite, which may affect these measurements.

Thermomechanical Response

Strain-temperature responses obtained via uniaxial constant force thermal cycling experiments are shown in Figs. 30, 31 for aged materials in tension and compression, respectively. The data correspond to the second thermal cycle at each stress level indicated. Displaying the entire hysteresis curve aids in visualizing the nature of the actuation response that cannot be fully and clearly described using summarized data. For example, the choice of an upper cycle temperature of 300 °C for alloy H1 seems sufficient for completing the phase transformation. But this same temperature is clearly not adequate for alloy H6 at higher stress levels, especially considering the effect of stress on transformation temperatures. Similarly, slopes, temperature sensitivity, and other features can be better perceived from a complete hysteresis curve.

Depending on the alloy chemistry and microstructure, the alloys are shown to exhibit a diverse range of transformation properties. Figures 32, 33 display the characteristic stress-temperature relationships corresponding to M_s, M_f, A_s, and A_f in tension and compression, respectively. Largely, the transformation temperatures exhibit a pseudolinear correlation, where temperatures shift higher with increasing stress. This dependence is better characterized when expressed in terms of the Clausius–Clapeyron relationship ($d\sigma/dT$) [72] as shown in Fig. 34. The reported slopes were obtained by linearly fitting the data with stresses from 100 MPa and above, given the 0 MPa point typically displays large deviations, based largely on prior history and handling of the sample. The stress dependence of the M_s and A_f temperatures were relatively consistent across all alloys, as seen in Fig. 34b, d. The average values of the stress rate were 8.9 to − 17.2 and 6.9 to − 11.2 MPa/°C (tension to compression), for M_s and A_f, respectively. Much larger scatter was observed for the stress-M_f and stress-A_s relationships across the various alloys, as seen in Fig. 34a, c. However, the average values for both stress rates were relatively similar, 22 to − 18 and 17 to − 18 MPa/°C for M_f and A_s, respectively.

While it is known that these trends are highly dependent on composition, the test parameters can also have a large effect on the results. For example, referring back to the complete hysteresis curves of Fig. 30, the choice of 350 °C UCT for alloy H13 can clearly affect the A_f data fitting as the stress increases, since the transformation does not fully complete by the UCT at the highest stresses. As a result, the Clausius–Clapeyron slopes can also vary depending on this parameter. Additionally, fitting the entire data set from 0 to 500 MPa, or from 100 to 400 MPa, can yield dissimilar results using a simple linear fit. For guidance on the choice of UCT and other test parameters, the reader is referred to the test standard ASTM E3097 [37] and related work [73].

Thermal hysteresis is shown in Figs. 35, 36 in tension and compression, respectively. Hysteresis was calculated using two methods: ($A_f - M_s$) as it is typically reported, and ($A_{50} - M_{50}$) as outlined by the ASTM E3097 test method [37], where A_{50} and M_{50} represent the temperatures at a point halfway through the transformations. When the forward and reverse transformation paths are parallel, such as alloy H1 of Fig. 30, both methods yield similar results. However, when the slopes deviate between the heating and cooling paths, for example alloy H7 of Fig. 30, the results are expected to vary. Moreover, this latter case can be magnified with the application of stress. The hysteresis is found to vary from alloy to alloy, ranging from 20 °C to as high as 60 °C at the 0 MPa stress. Upon the application of stress, hysteresis values increase in some alloys (e.g., alloy H17) while others decrease (e.g., alloy H1), depending on composition. In the Ni-rich formulations, the hysteresis decreases (or remains constant) with stress as the stress rates of the A_f and M_s remain nearly identical, maintaining the width of the hysteresis. Similar behaviors have been observed in NiTiZr alloys [74] and other compositions [75]. On the other hand, the near-stoichiometric or Ti-rich compositions show an increase in hysteresis with the application of stress due to the diverging A_f and M_s temperatures.

Actuation strains, calculated as the full strain recovery from the lower to the upper cycle temperatures, are reported in Fig. 37. Generally, the strains are higher in tension than compression and increase as a function of applied stress. In some alloys, the maximum strain recovery has not been reached at the highest applied stress of 500 MPa, while others, such as alloy H14 show a maximum strain at 400 MPa. In a related approach, the transformation strains, calculated as the strain recovery due to the austenitic transformation on heating, are reported in Fig. 38. The trend is similar, but in compression, the transformation and CTE strains both cause elongation, resulting in higher actuation strains, while in tension, the transformation strain causes contraction, and the CTE strains tend to cause elongation, leading to an actuation strain that is equivalent to or lower than the transformation strain. In addition, while transformation strain is somewhat dependent on UCT [76], there is a direct correlation between actuation strain and the temperature extremes (LCT and UCT), as changing these will result in more or less CTE strain.

The residual strains, measured at the LCTs, are shown in Fig. 39. Noting that these materials were aged to promote strength and stability, most of the Ni-rich alloys exhibit minimal residual strains even at higher stresses. In contrast, higher residual strains are obtained in the stoichiometric or Ti-rich compositions such as alloy H7. In fact, residual strains start to accumulate even at very low stresses due to the lack of precipitation strengthening against plastic deformation that accompanies the transformation process in this alloy.

Chemistry Adjustment

Given the nature of molten metals processing, alloys produced with identical "target compositions" will differ slightly in their "actual compositions." It is well known that in the case of NiTi-based alloys, even minor differences in composition that are within the uncertainty of any measurement technique can have significant consequences on properties. This was expected and to some extent, planned for to highlight the subtleties associated with the various melting methods and processing techniques. For example, it is known that a VIM process introduces carbides due to reactions with the crucible material; hence, some Ti will be apportioned toward forming TiC. As a result, the final matrix chemistry is expected to be slightly Ti-lean compared to the target composition. Similarly, a VISM process does not introduce carbides, but oxides in the form of HfO_2, $(TiHf)_4Ni_2O_x$, or other inclusions can form, which also results in a Ti + Hf lean matrix. Using high power sources with a combination of high vacuum can cause Ni evaporation or material loss due to flashing during exothermic reactions, resulting in a Ni-lean composition compared to the target. Other factors such as vacuum levels, initial charge purity, process variables (e.g., power, melt pool stirring, etc.) also play an important role in the chemistry of the final product.

Irrespective of the melting method, all chemistries reported here were measured using the ICP technique. Although ICP can be accurate to parts per million ranges for low-level constituents, the accuracy can be as low as ± 2% of the absolute value for the major constituents. Therefore, small variations in atomic percentages obtained by ICP may not be a good enough indicator of the true chemistry for NiTiHf alloys or SMAs in general. In fact, due to the high compositional sensitivity of most SMAs, the more accurate parameter to classify the alloys is by transformation temperatures, as implemented by industrial practice. In order to correct the chemistry and better map the transition temperatures to a Ni content, carefully arc-melted buttons were produced and used for this purpose in a previous study [77]. The actual compositions of the arc-melt buttons are better correlated with target compositions, because only buttons with identical charge weight (before melting) and the button weight (after melting) were used, hence confirming no loss of alloying material. Moreover, given the small size of these melts (~ 30 g), there is more control over the melting parameters, resulting in very low oxygen pickup, and no carbon contamination due to the cold crucible melting process. Alloys with a Ni content from 50 to 51 at.% were

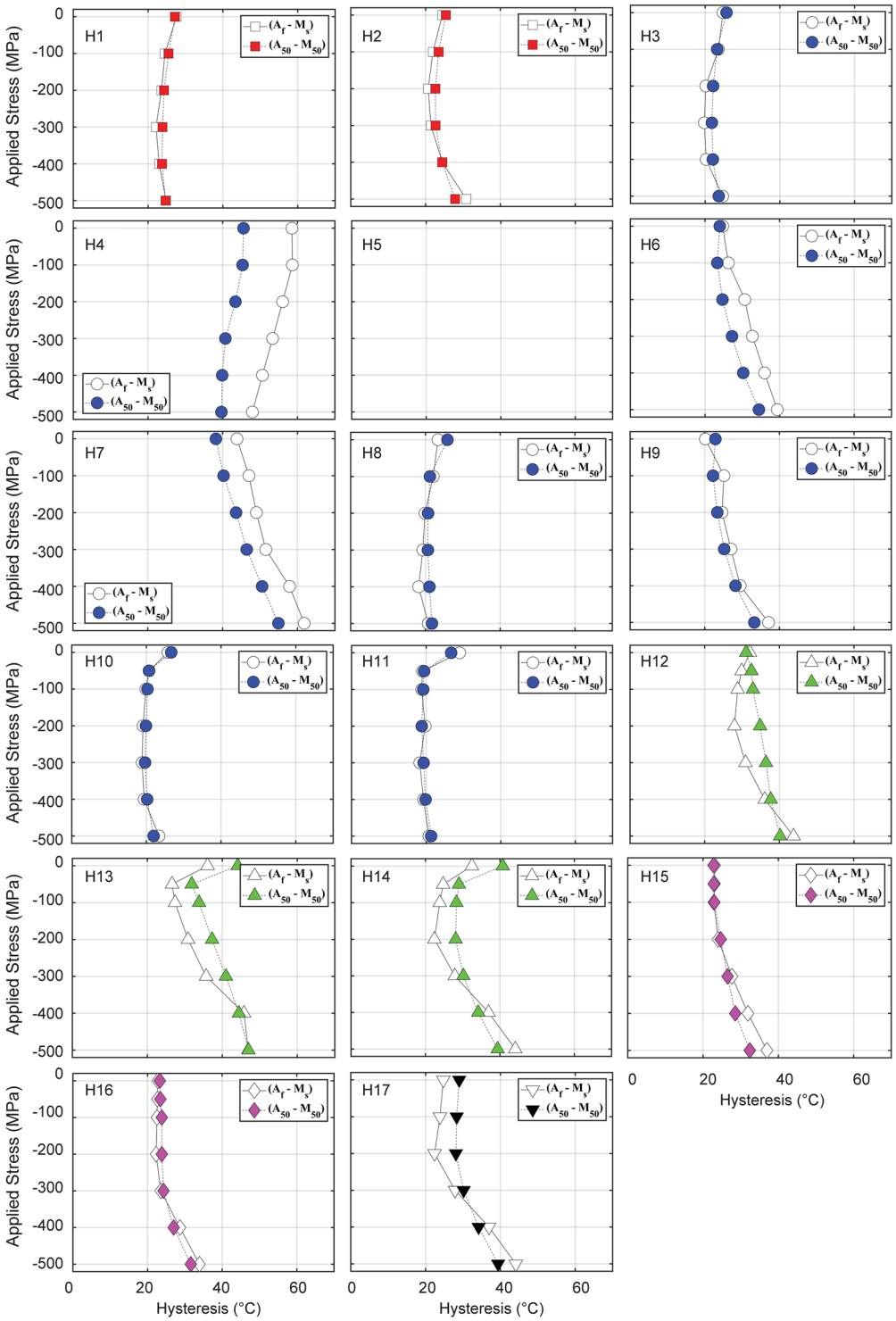

Fig. 36 Thermal hysteresis as a function of stress for alloys aged at 550 °C for 3 h and air cooled, tested in compression. The process types are *1* vacuum induction melting (VIM *filled red square, open red square*), *2* vacuum induction skull melting (VISM *filled blue circle, open blue circle*), *3* vacuum induction skull melting + vacuum arc remelting (VISM + VAR *filled green triangle, open green triangle*), *4* VIM + VAR *filled pink diamond, open pink diamond*, and *5* plasma arc melting + vacuum arc remelting (PAM + VAR *filled inverted black triangle, open black inverted triangle*) (Color figure online)

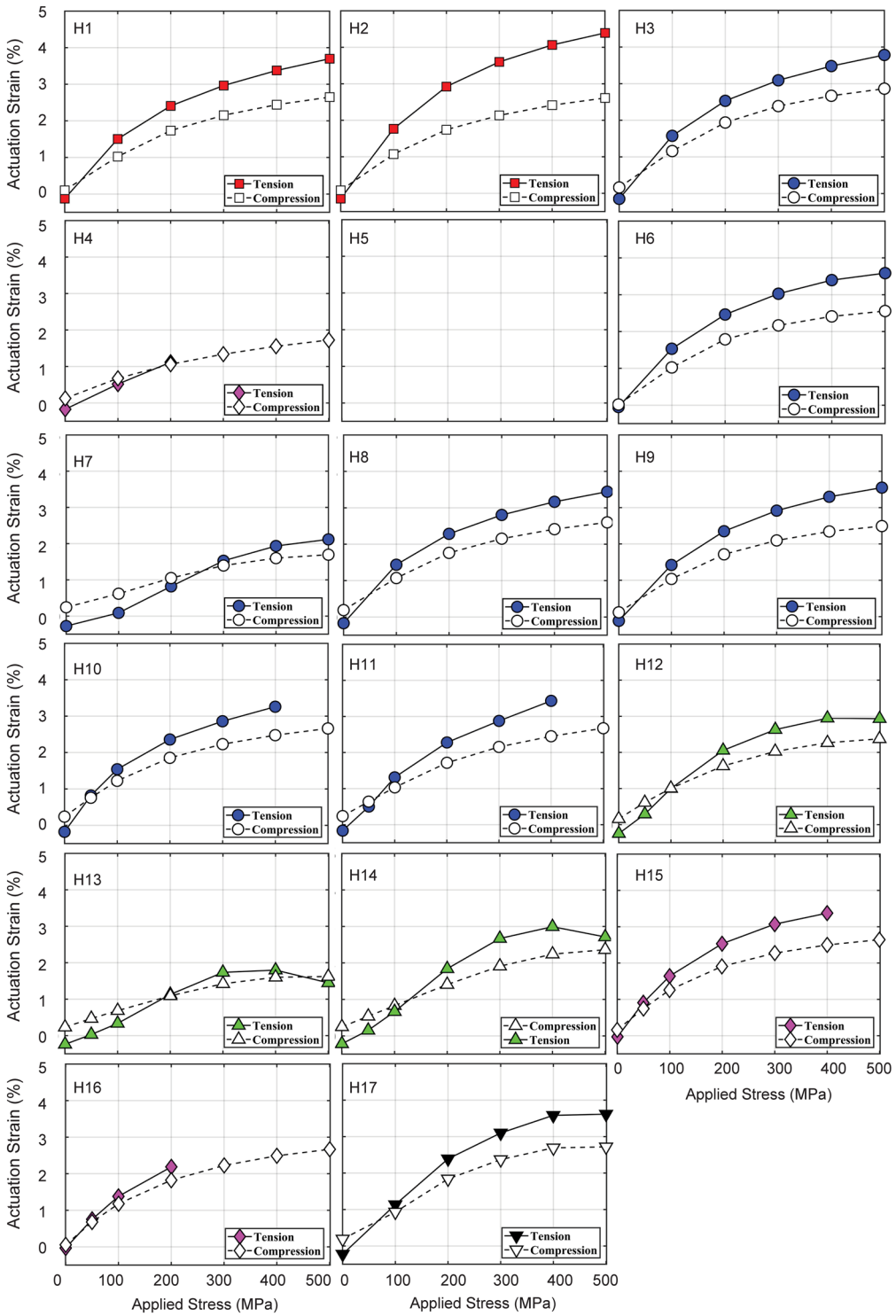

Fig. 37 Actuation strain as a function of stress for alloys aged at 550 °C for 3 h and air cooled, tested in tension (*solid symbols*) and compression (*open symbols*). The process types are *1* vacuum induction melting (VIM *filled red square, open red square*), *2* vacuum induction skull melting (VISM *filled blue circle, open blue circle*), *3* vacuum induction skull melting + vacuum arc remelting (VISM + VAR *filled green triangle, open green triangle*), *4* VIM + VAR *filled pink diamond, open pink diamond*, and *5* plasma arc melting + vacuum arc remelting (PAM + VAR *filled inverted black triangle, open black inverted triangle*) (Color figure online)

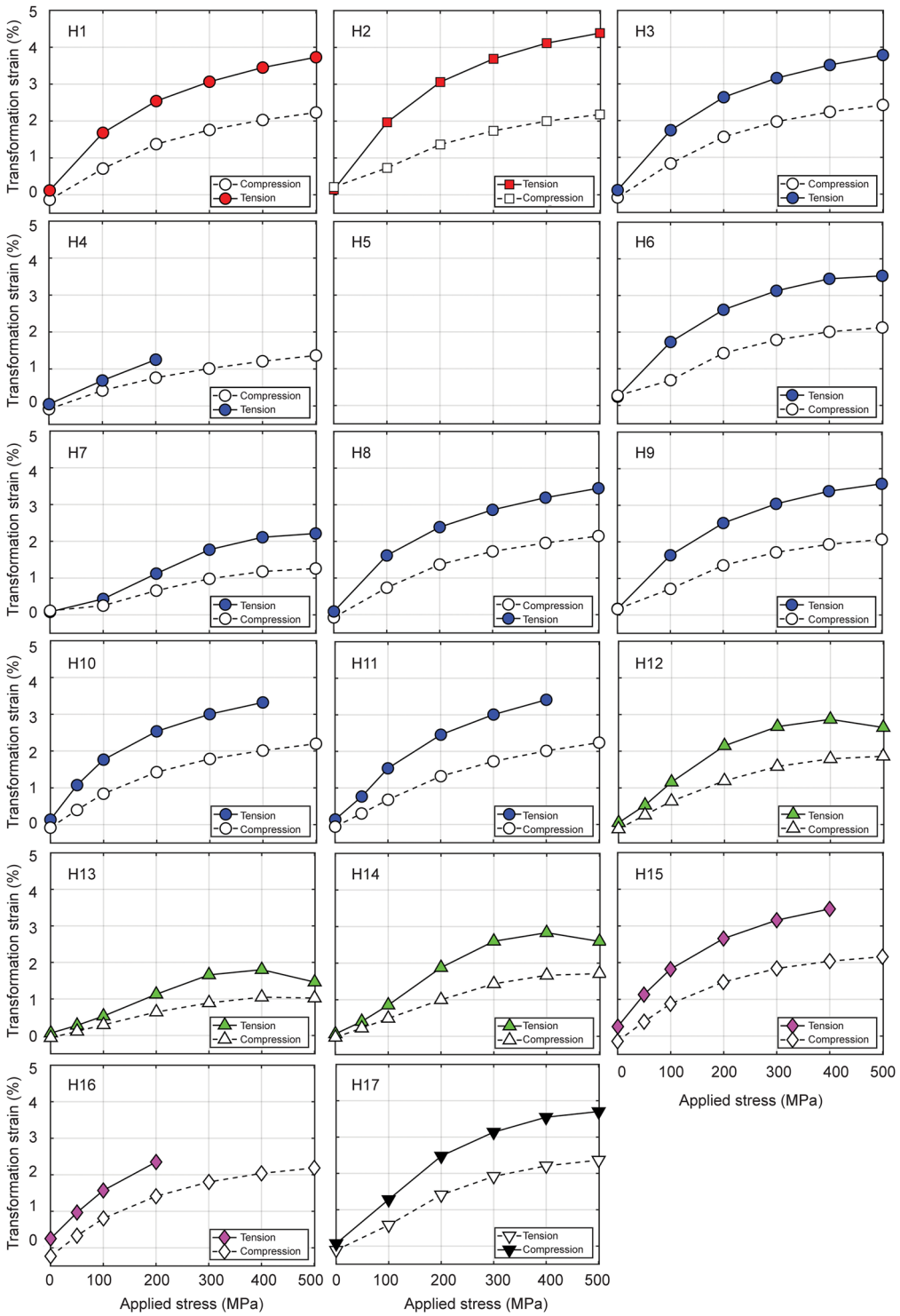

Fig. 38 Transformation strain as a function of stress for alloys aged at 550 °C for 3 h and air cooled, tested in tension (*solid symbols*) and compression (*open symbols*). The process types are *1* vacuum induction melting (VIM *filled red square, open red square*), *2* vacuum induction skull melting (VISM *filled blue circle, open blue circle*), *3* vacuum induction skull melting + vacuum arc remelting (VISM + VAR *filled green triangle, open green triangle*), *4* VIM + VAR *filled pink diamond, open pink diamond*, and *5* plasma arc melting + vacuum arc remelting (PAM + VAR *filled inverted black triangle, open black inverted triangle*) (Color figure online)

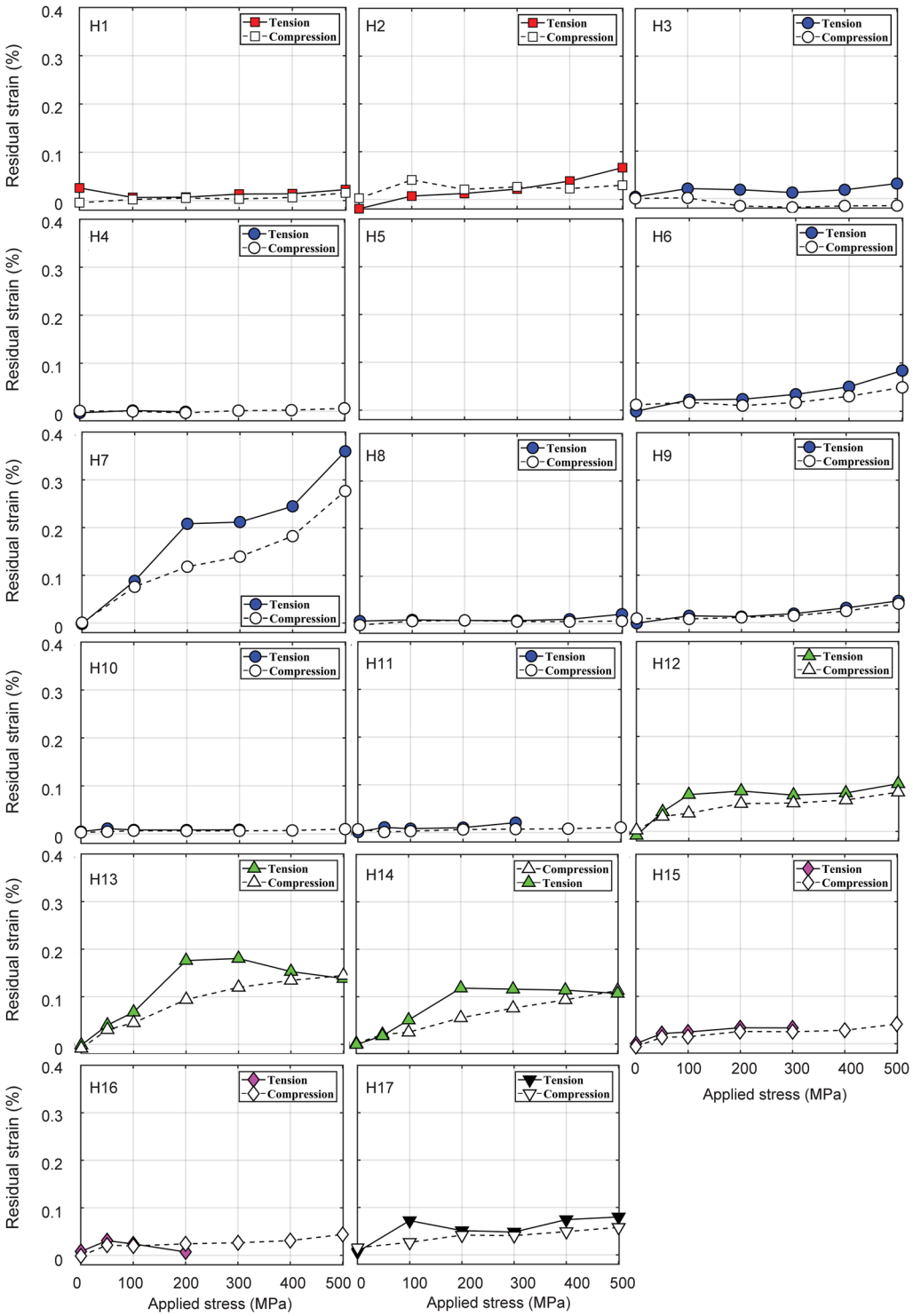

Fig. 39 Residual strain as a function of stress for alloys aged at 550 °C for 3 h and air cooled, tested in tension (*solid symbols*) and compression (*open symbols*). The process types are *1* vacuum induction melting (VIM *filled red square, open red square*), *2* vacuum induction skull melting (VISM *filled blue circle, open blue circle*), *3* vacuum induction skull melting + vacuum arc remelting (VISM + VAR *filled green triangle, open green triangle*), *4* VIM + VAR *filled pink diamond, open pink diamond*, and *5* plasma arc melting + vacuum arc remelting (PAM + VAR *filled inverted black triangle, open black inverted triangle*) (Color figure online)

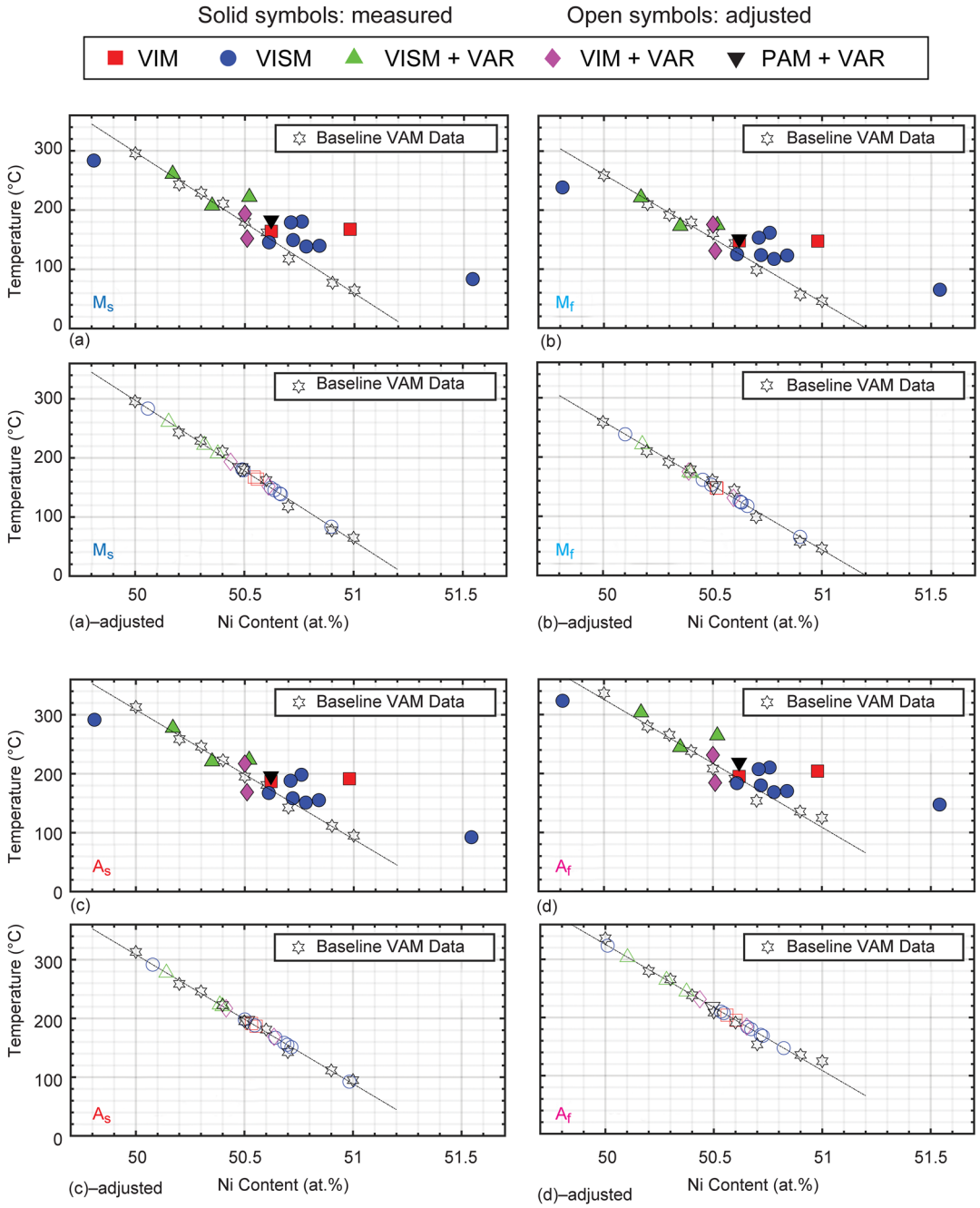

Fig. 40 Baseline transformation temperatures from the vacuum arc-melted (VAM) buttons and DSC measured transformation temperatures as a function of Ni content. **a** Martensite start (M_s), **b** martensite finish (M_f), **c** austenite start (A_s), and **d** austenite finish (A_f). *Solid symbols* (measured using ICP) and *open symbols* (adjusted). The process types are *1* vacuum induction melting (VIM *filled red square, open red square*), *2* vacuum induction skull melting (VISM *filled blue circle, open blue circle*), *3* vacuum induction skull melting + vacuum arc remelting (VISM + VAR *filled green triangle, open green triangle*), *4* VIM + VAR *filled pink diamond, open pink diamond*, and *5* plasma arc melting + vacuum arc remelting (PAM + VAR *filled inverted black triangle, open black inverted triangle*) (Color figure online)

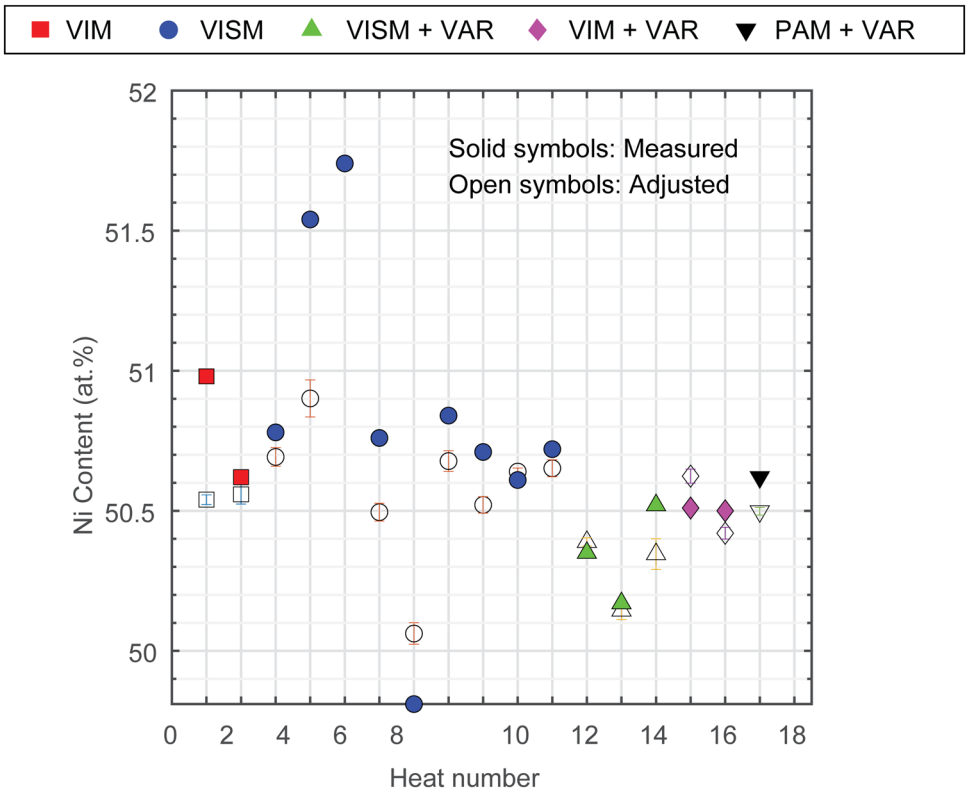

Fig. 41 Measured and adjusted Ni content for alloys aged at 550 °C for 3 h and air cooled. The average value along with standard deviation (plotted as *error bars*) are shown

Table 5 Measured and adjusted Ni content for all alloys aged at 550 °C for 3 h and air cooled

No. of heat	Ni-measured (at.%)	Ni-adjusted (at.%)
H1	50.98	50.54
H2	50.62	50.56
H3	50.78	50.69
H4	51.54	50.90
H5	51.74[a]	–
H6	50.76	50.50
H7	49.81	50.06
H8	50.84	50.68
H9	50.71	50.52
H10	50.61	50.64
H11	50.72	50.65
H12	50.35	50.39
H13	50.17	50.14
H14	50.52	50.35
H15	50.51	50.62
H16	50.50	50.42
H17	50.62	50.50

[a]Includes 2.51 at.% Fe

used while holding the Hf content constant at 20 at.% [77]. The buttons were solutionized and then aged at 550 °C for 3 h and air cooled.

The baseline transformation temperatures from the vacuum arc-melted (VAM) buttons in the aged condition are plotted in Fig. 40 against the aim compositions, which are presumed to be the true chemistries. The transformation temperatures plotted here are from the tenth cycle from DSC measurements. The data were fitted with a linear approximation, although higher order regression fits were also examined, but no discernible difference in accuracy of fit was obtained. Also plotted are the ICP measured Ni values for alloys H1 through H17 in the aged condition and the transformation temperatures, showing the level of scatter in the measurements (Fig. 40a–d). Each alloy composition was then corrected for the Ni content based on transformation temperatures by shifting the temperatures horizontally to intersect with the fit from the established baseline VAM data for each characteristic temperature (Fig. 40a–d, adjusted). Surprisingly, the corrected Ni content was nearly identical using either the M_s, M_f, A_s, or A_f datasets, and the average value along with standard deviation (plotted as error bars) is shown in Fig. 41. For most alloys, the error bar is approximately the symbol size. The measured and adjusted chemistries are also listed in Table 5.

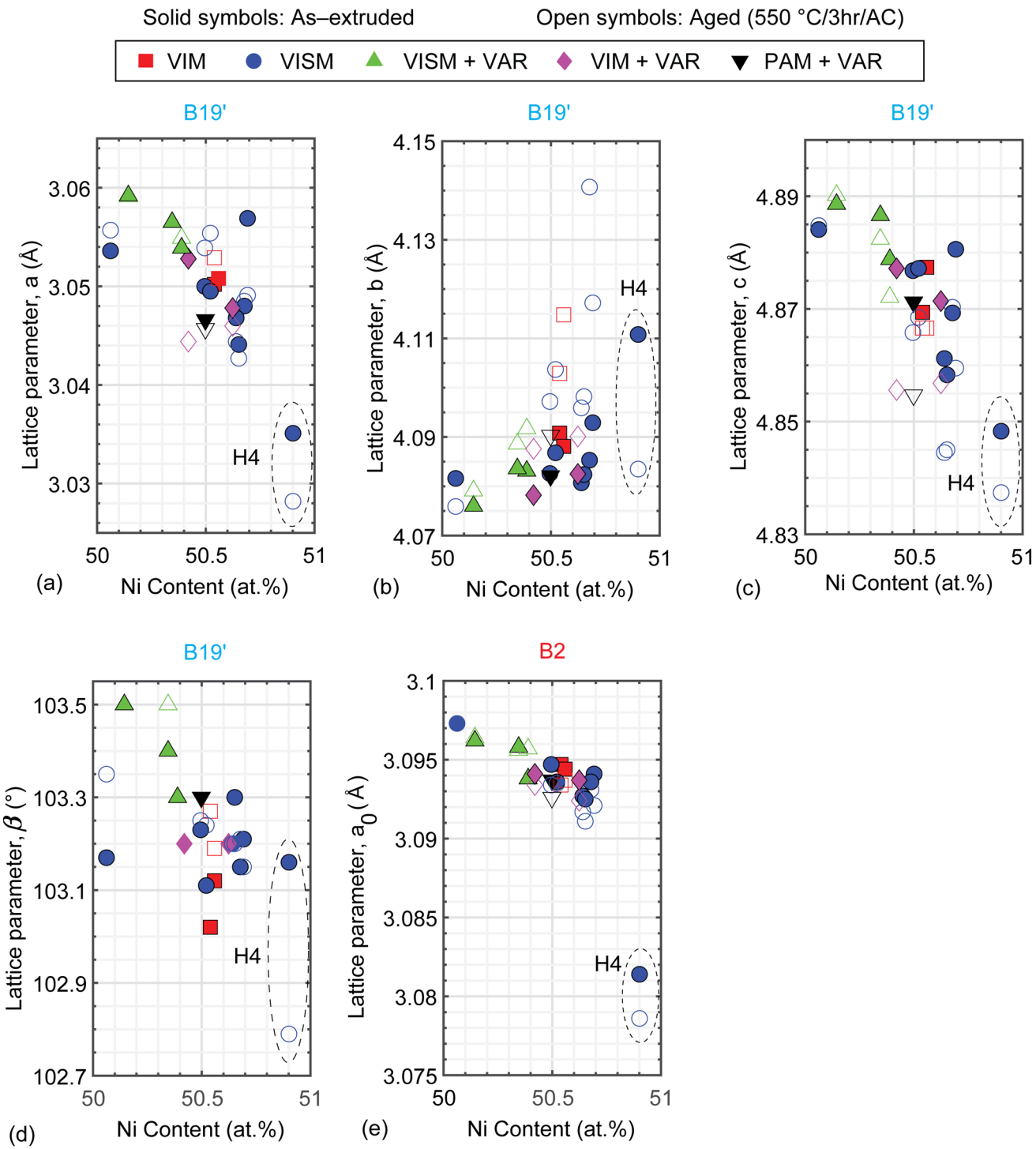

Fig. 42 Lattice parameters as a function of adjusted Ni content for alloys in the as-extruded (*solid symbols*) and aged conditions (*open symbols*). **a**–**d** Monoclinic lattice parameters, and **e** cubic lattice parameters. The process types are *1* vacuum induction melting (VIM *filled red square, open red square*), *2* vacuum induction skull melting (VISM *filled blue circle, open blue circle*), *3* vacuum induction skull melting + vacuum arc remelting (VISM + VAR *filled green triangle, open green triangle*), *4* VIM + VAR *filled pink diamond, open pink diamond*, and *5* plasma arc melting + vacuum arc remelting (PAM + VAR *filled inverted black triangle, open black inverted triangle*) (Color figure online)

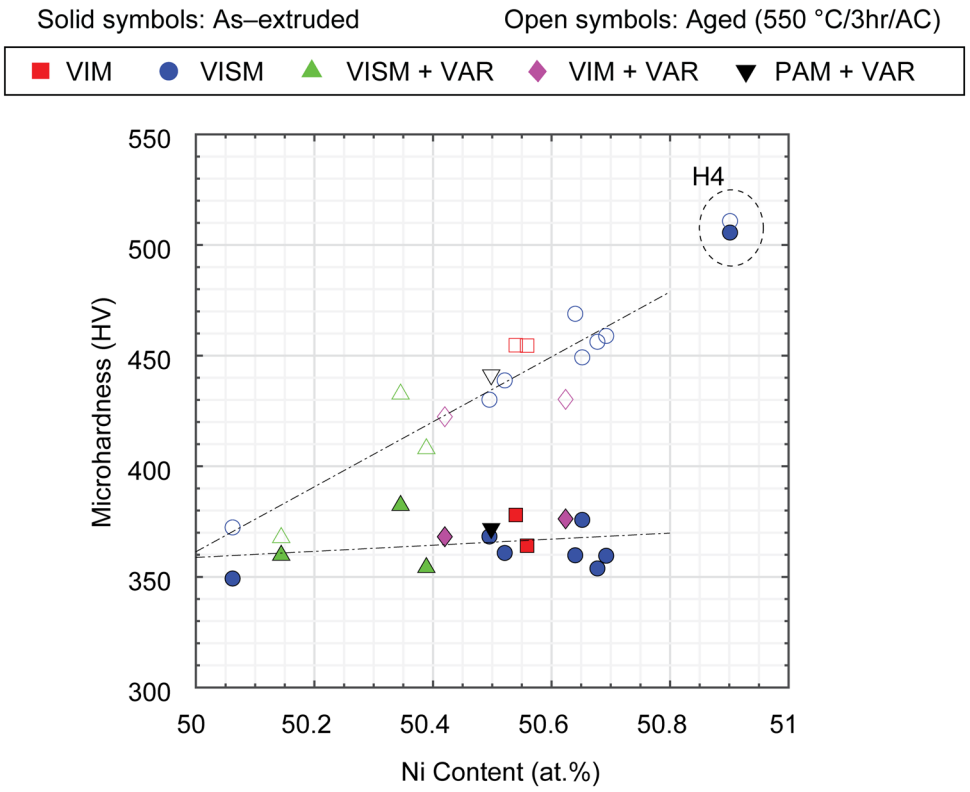

Fig. 43 Vickers micro-hardness as a function of adjusted Ni content for alloys in the as-extruded (*solid symbols*) and aged conditions (*open symbols*). The process types are *1* vacuum induction melting (VIM *filled red square, open red square*), *2* vacuum induction skull melting (VISM *filled blue circle, open blue circle*), *3* vacuum induction skull melting + vacuum arc remelting (VISM + VAR *filled green triangle, open green triangle*), *4* VIM + VAR *filled pink diamond, open pink diamond*, and *5* plasma arc melting + vacuum arc remelting (PAM + VAR *filled inverted black triangle, open black inverted triangle*) (Color figure online)

Based on this correction, several properties were replotted as a function of the adjusted Ni content to better capture correlations. The intent is that these corrected results will be used as a guide for material properties selection and/or design, and a baseline for further optimization of this alloy family. Starting with the X-ray data presented in Table 3 and Fig. 12, the lattice parameters corresponding to each alloy are shown in Fig. 42 as a function of adjusted Ni content. While the data still have some scatter, trends are now much more apparent for the aged samples. The B19′ lattice parameters a, c, and β decrease with increasing Ni content, while the lattice parameter b increases. Similarly, the B2 lattice parameter a_0 decreases with increasing Ni content. Comparable trends have been observed in other NiTi alloys where the unit cell volume changes with the addition of Ni concentration in solution, given Ni has a lower atomic diameter compared to Ti [78]. Although not discussed here, the conjugate effect of Hf addition on the lattice parameters has been studied and reported elsewhere [79–82].

The average Vickers hardness values as a function of adjusted Ni content are shown in Fig. 43 for the as-extruded and aged conditions. A clear trend was observed with continually increasing Ni content. The hardness increased by ~ 9 HV for each 0.1 at.% increase in Ni content in the aged condition, due to the precipitation strengthening, compared to a 1.5 HV increase due to solid-solution hardening alone in the as-extruded case. It is noted that H4 was excluded from the linear regression due to off-composition Hf content, non-ideal microstructure and presence of other phases that resulted in higher hardness.

DSC data presented in Figs. 21, 22 were also plotted as a function of adjusted Ni content as shown in Fig. 44. Generally, transformation temperatures were shown to decrease with increasing Ni content, as is known to occur in NiTi and NiTiHf alloys [6, 77, 83]. While the data indicated linear trends over the studied range of Ni content, it is expected that a nonlinear, steep drop would occur with additional Ni enrichment, as frequently observed in NiTi alloys [84]. It should also be noted that with increasing Ni content, aging produced a larger increase in transformation temperature over the as-extruded condition, offsetting the decrease in transformation temperature with Ni content in the as-extruded (predominantly single-phase) material. The thermal hysteresis, defined as the austenite finish minus martensite start ($A_f - M_s$), is shown clustered around a hysteresis between 30 and 40 °C. No significant trend in hysteresis was delineated between the aged and as-extruded conditions. Yet, it is worth noting that the lowest value of thermal hysteresis was obtained around a Ni content of 50.52 at.% with a value of 28 °C in the aged alloy H9.

The isothermal mechanical responses for the aged materials as a function of adjusted Ni content are shown in Fig. 45 for the room-temperature tests. At room temperature, the apparent Young's moduli (Fig. 45a) decreased as a function

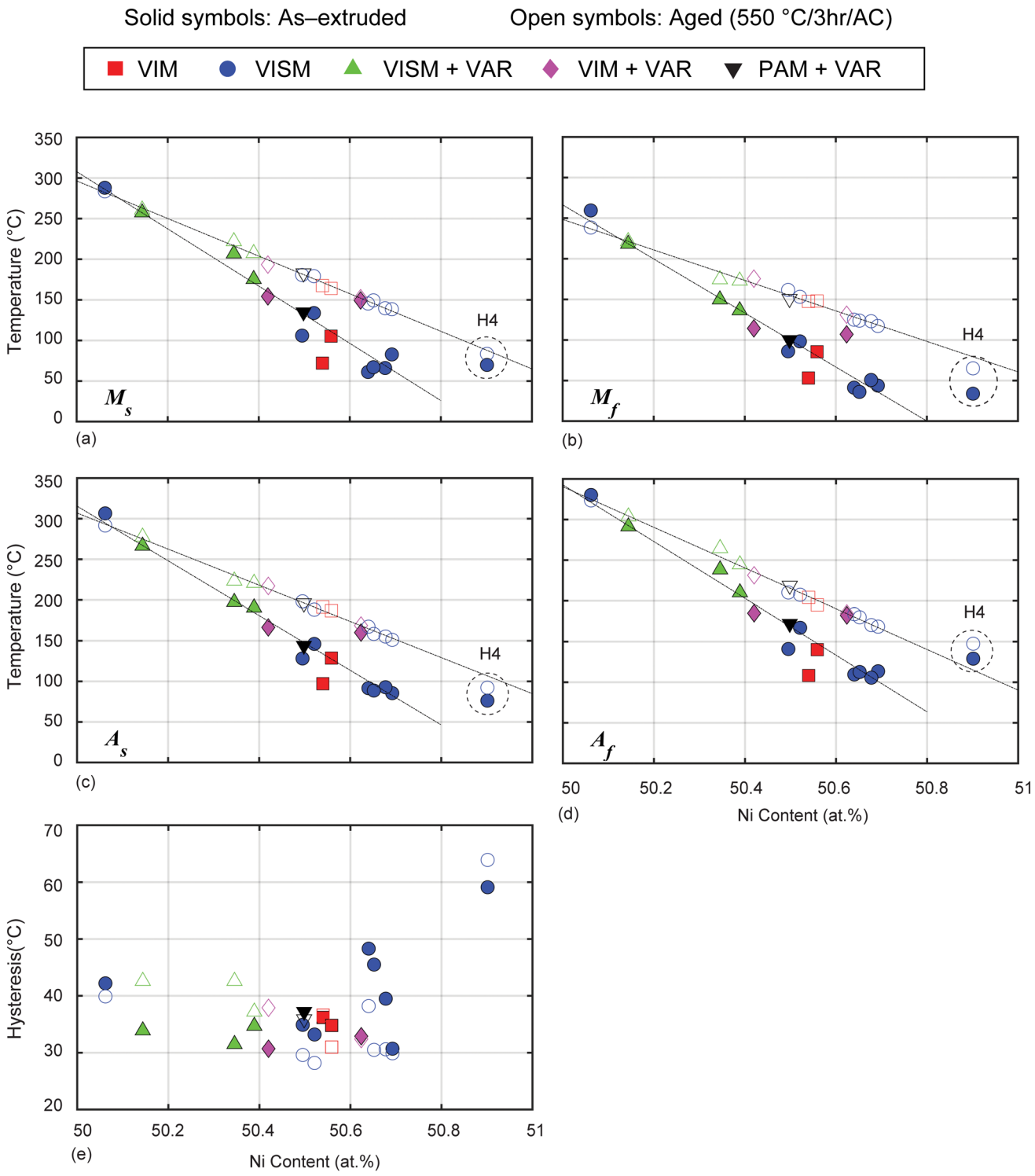

Fig. 44 Transformation temperatures as a function of adjusted Ni content for alloys in the as-extruded (*solid symbols*) and aged conditions (*open symbols*). **a** Martensite start (M_s), **b** martensite finish (M_f), **c** austenite start (A_s), **d** austenite finish (A_f), and **e** thermal hysteresis corresponding to the last thermal cycle of the DSC data. The process types are *1* vacuum induction melting (VIM *filled red square, open red square*), *2* vacuum induction skull melting (VISM *filled blue circle, open blue circle*), *3* vacuum induction skull melting + vacuum arc remelting (VISM + VAR *filled green triangle, open green triangle*), *4* VIM + VAR *filled pink diamond, open pink diamond*, and *5* plasma arc melting + vacuum arc remelting (PAM + VAR *filled inverted black triangle, open black inverted triangle*) (Color figure online)

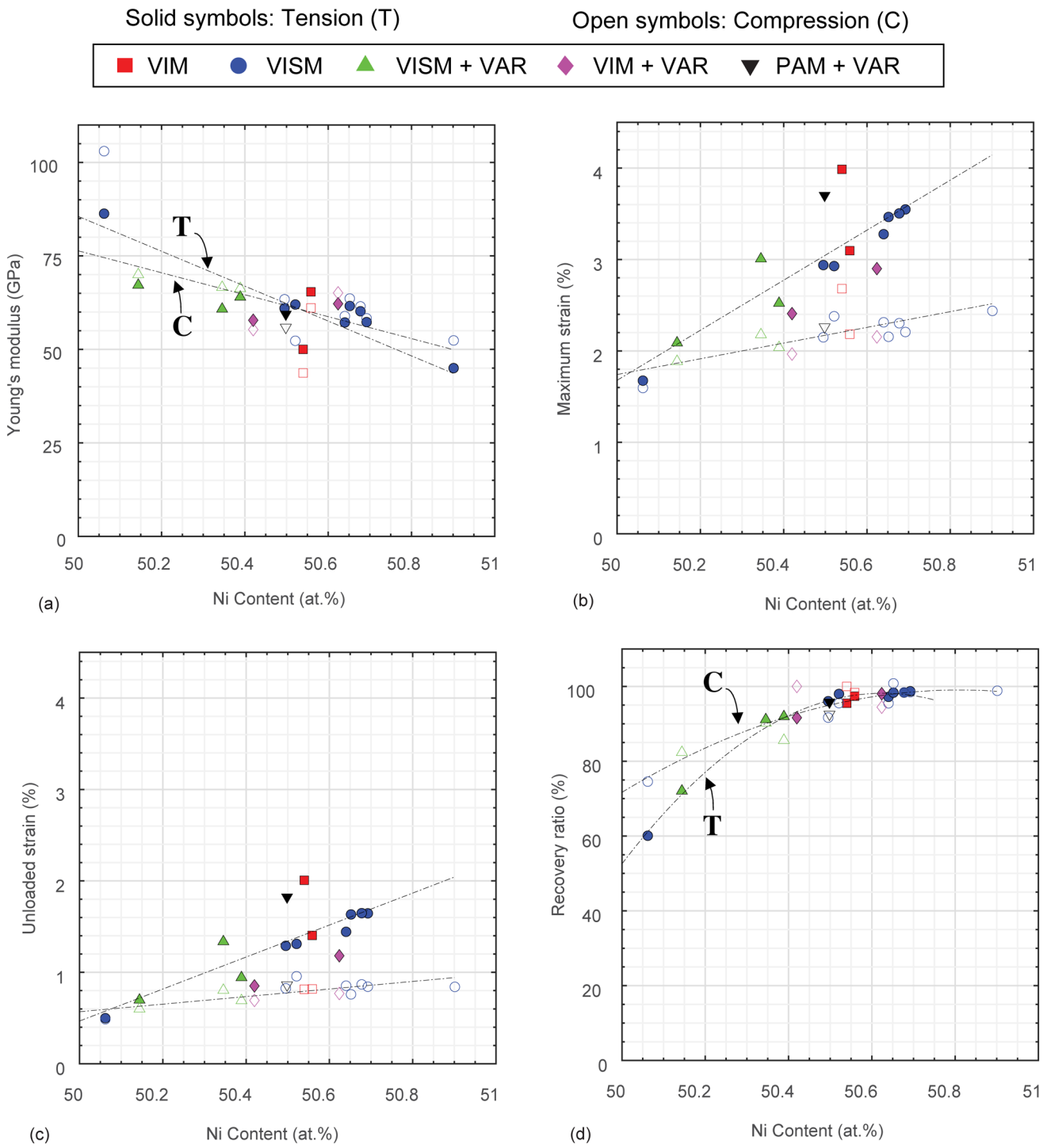

Fig. 45 Room-temperature isothermal data as a function of adjusted Ni content for alloys aged at 550 °C for 3 h and air cooled in tension (*solid symbols*) and compression (*open symbols*). **a** Young's Modulus, **b** the maximum loading strain (strain at the highest stress of 1 GPa or failure), **c** unloaded strain (strain after unloading to 0 MPa), and **d** recovery ratio (percent strain recovered after heating and cooling). The process types are *1* vacuum induction melting (VIM *filled red square, open red square*), *2* vacuum induction skull melting (VISM *filled blue circle, open blue circle*), *3* vacuum induction skull melting + vacuum arc remelting (VISM + VAR *filled green triangle, open green triangle*), *4* VIM + VAR *filled pink diamond, open pink diamond*, and *5* plasma arc melting + vacuum arc remelting (PAM + VAR *filled inverted black triangle, open black inverted triangle*) (Color figure online)

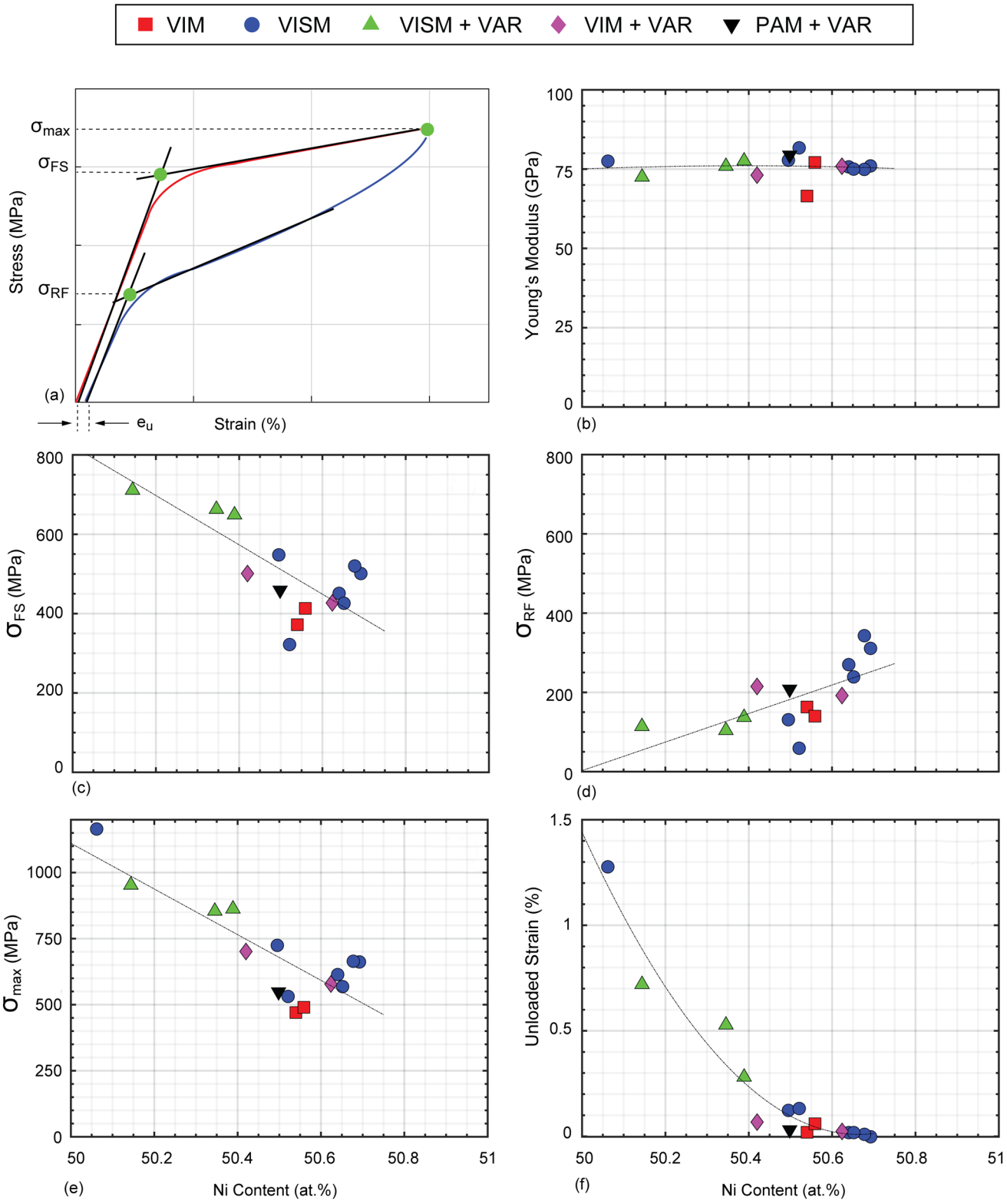

Fig. 46 High-temperature isothermal data in tension as a function of adjusted Ni content for alloys aged at 550 °C for 3 h and air cooled. **a** Graphical representation of the reported variables, **b** Young's Modulus, **c** the onset stress of the forward transformation start (σ_{FS}), **d** the stress of the reverse transformation finish (σ_{RF}), **e** stress at the maximum loading strain of 3% (σ_{max}), and **f** the unloaded strain (strain after unloading to 0 MPa). The process types are *1* vacuum induction melting (VIM *filled red square*), *2* vacuum induction skull melting (VISM *filled blue circle*), *3* vacuum induction skull melting + vacuum arc remelting (VISM + VAR *filled green triangle*), *4* VIM + VAR *filled pink diamond*, and *5* plasma arc melting + vacuum arc remelting (PAM + VAR *filled inverted black triangle*) (Color figure online)

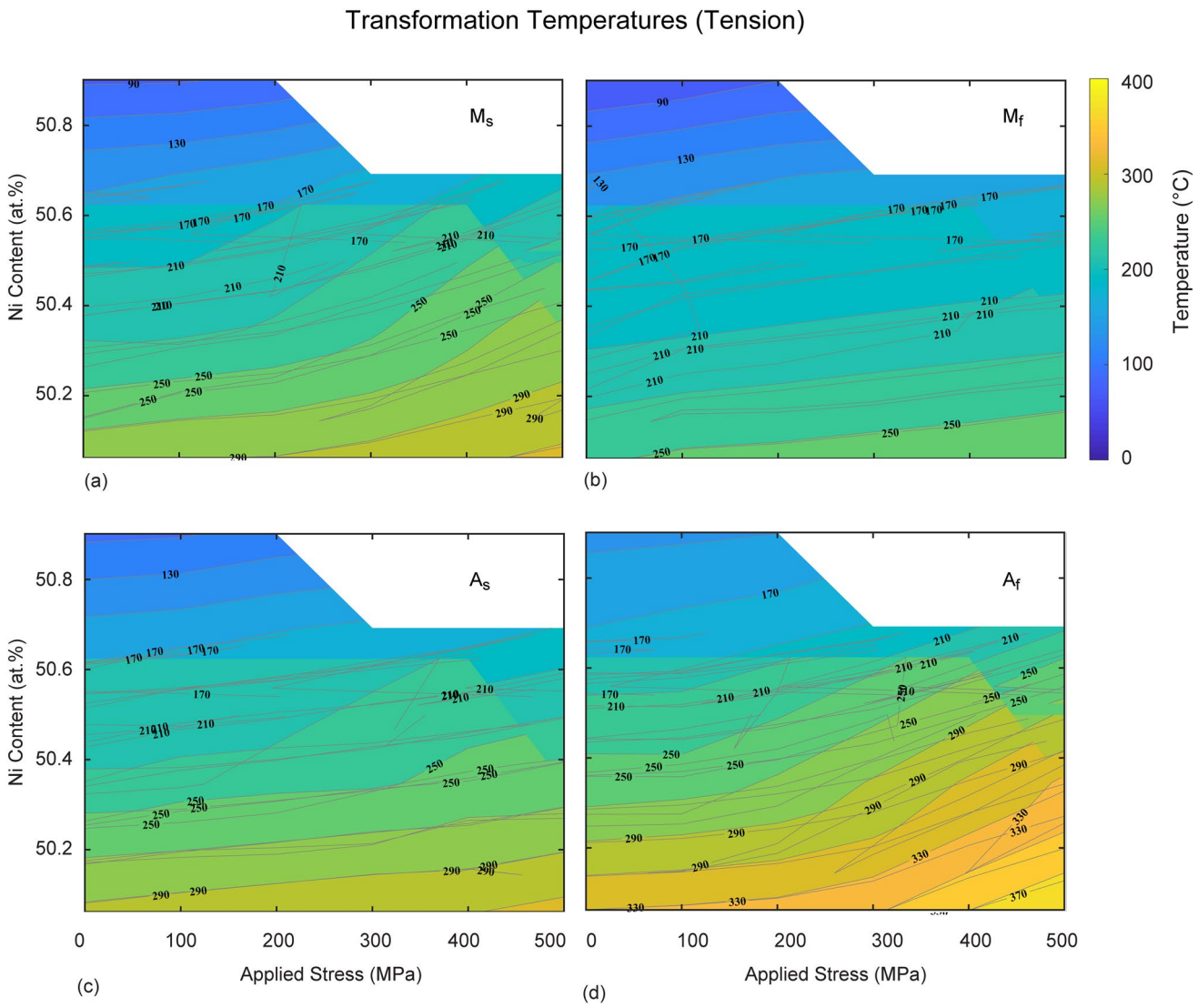

Fig. 47 Effect of adjusted composition and applied stress on the transformation temperatures for alloys aged at 550 °C for 3 h and air cooled, tested in tension

of Ni in both tension and compression, with no discernible difference between the two testing modes (within the data scatter). As the Ni content increases, it is understood that the M_f decreases and effectively approaches the test temperature of ~ 25 °C. This behavior (i.e., decreasing modulus when approaching the transformation temperature) can also be clearly seen in dynamic Young's moduli of similar alloys as a function of temperature [63, 85]. As a result, the Ti-rich or near-stoichiometric compositions exhibit a higher modulus than the more Ni-rich counterparts, given that their M_f is further away from the test temperature.

The maximum (Fig. 45b) and the unloaded strains (Fig. 45c) increased with added Ni, with a steeper increase apparent in the tensile data. At the 1 GPa stress (target stress on loading), higher strains were achieved at higher Ni content as the hardening behavior changed. The Ni-rich alloys underwent the majority of martensite reorientation with low or no susceptibility to plastic deformation, resulting in a higher maximum strain and higher unloaded strain. This is not surprising given that the higher Ni alloys benefit from both solid solution and precipitation strengthening effects that help resist against plastic deformation. Additionally, it is speculated that local stresses around the precipitates can affect the reorientation process by providing additional back stress to promote such an effect. It can also be seen that in the higher Ni alloys, there was more tension–compression anisotropy (i.e., a higher maximum strain and unloaded strain results in tension compared to compression) in the isothermal response (see H3 and H8 in Fig. 24). This is more evidence of martensitic reorientation,

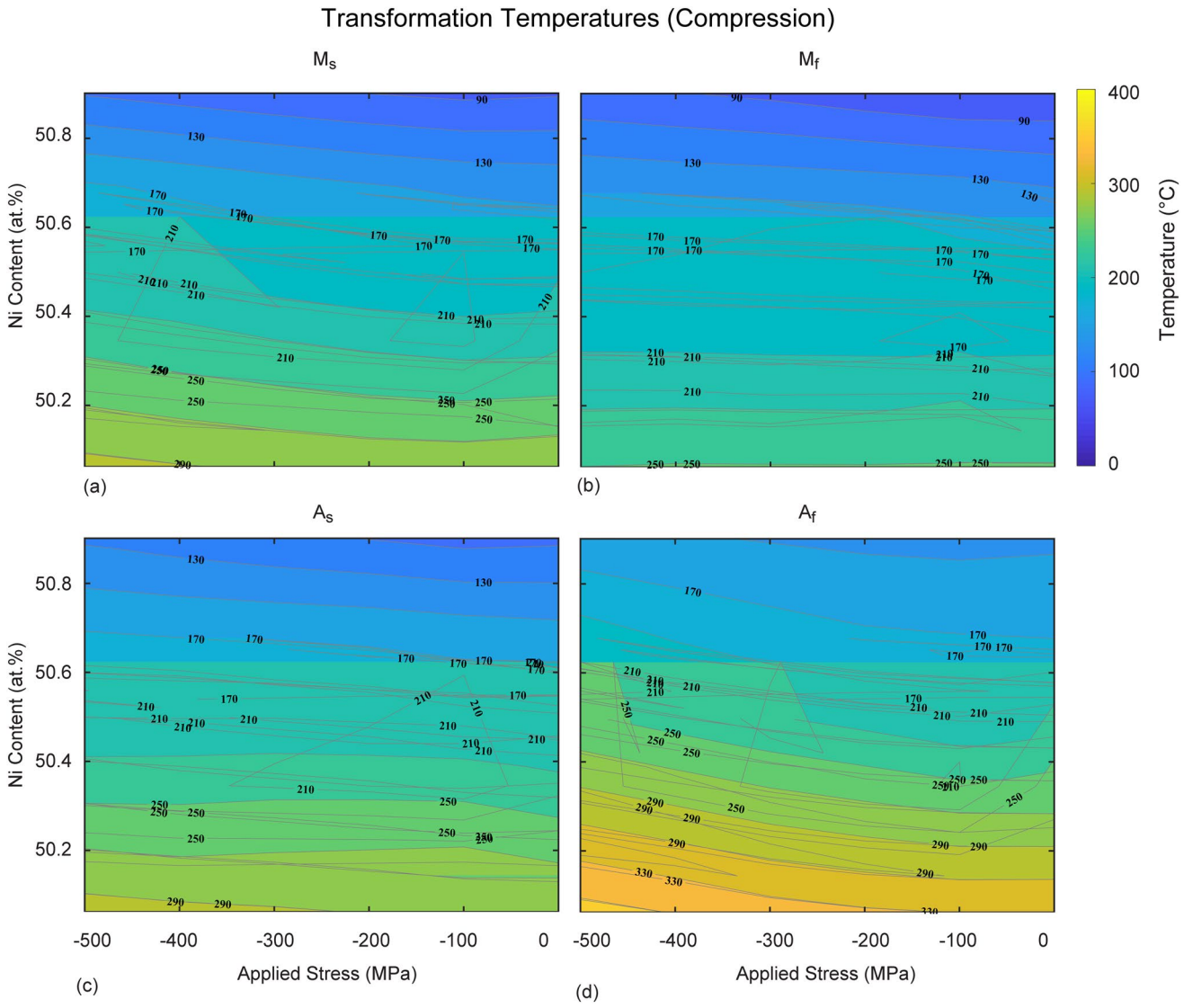

Fig. 48 Effect of adjusted composition and applied stress on the transformation temperatures for alloys aged at 550 °C for 3 h and air cooled, tested in compression

as crystallographically there is higher transformation strain capability in tension than in compression [86]. Along with the expected martensite reorientation process, the strain hardening in the Ni-lean alloys was affected by contributions of plastic deformation. This is a result of the lack or fewer precipitates, which did not effectively strengthen against permanent deformation. Hence, the Ni-lean alloys exhibited more plastic deformation, which resulted in less strain through martensite reorientation, and results in a more isotropic response in tension and compression (see H7, H13 in Fig. 24). This observation is further elucidated by the recovery ratios of Fig. 45d, where lower ratios are obtained in the Ni-lean alloys (i.e., permanent deformation), but the ratios are near 100% at the higher Ni content (i.e., full recovery upon heating).

For deformation of the austenite phase (Fig. 46), the elastic modulus was relatively uniform as a function of Ni content for all alloys in the range observed, with an average modulus of 75 GPa. Unlike the testing in the martensite phase, these tests were performed at a relatively constant temperature offset from the A_f (A_f + 10–35 °C), hence the temperature effect on the modulus does not come into play. The onset stress of the forward transformation start (σ_{FS}) decreases with added Ni (Fig. 46c), while the stress of the reverse transformation finish (σ_{RF}) increases (Fig. 46d). This behavior also suggests that the stress hysteresis ($\sigma_{FS} - \sigma_{RF}$) decreases with added Ni, as can be seen in Fig. 26—for example, H7 (Ni lean), H12 (higher Ni), and H8 (most Ni-rich). Figure 46e depicts the maximum stress achieved after loading to the target 3% strain. Commensurate with

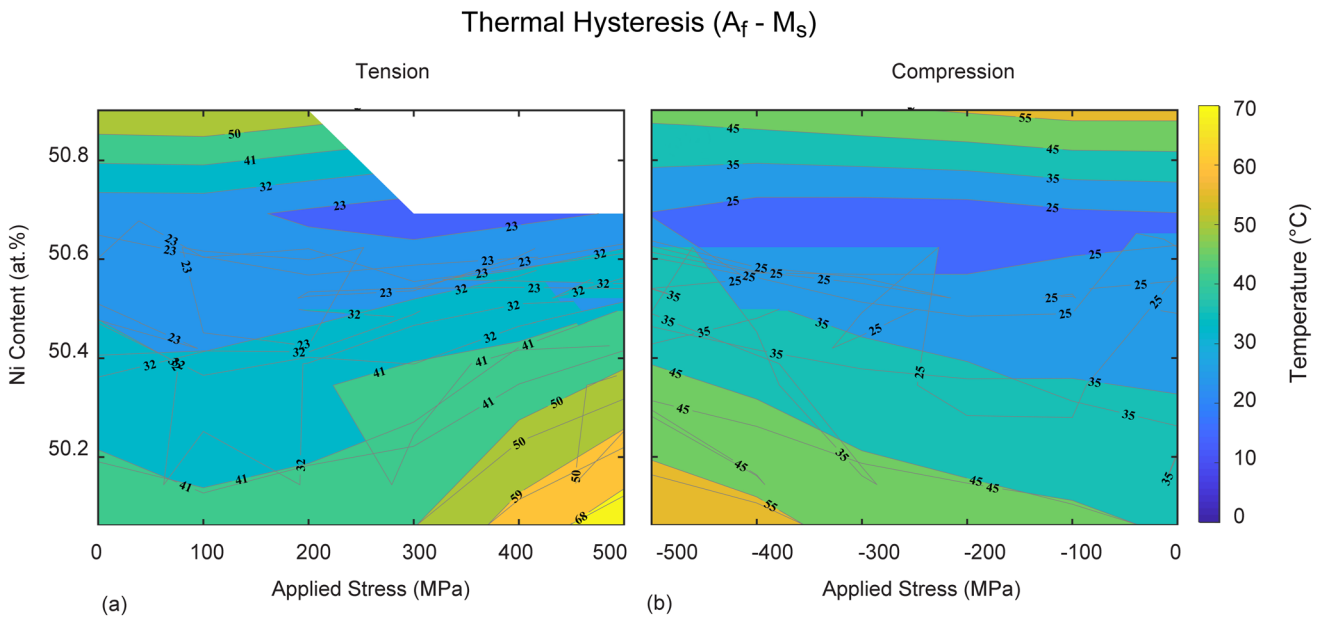

Fig. 49 Effect of adjusted composition and applied stress on the thermal hysteresis for alloys aged at 550 °C for 3 h and air cooled, tested in **a** tension and **b** compression

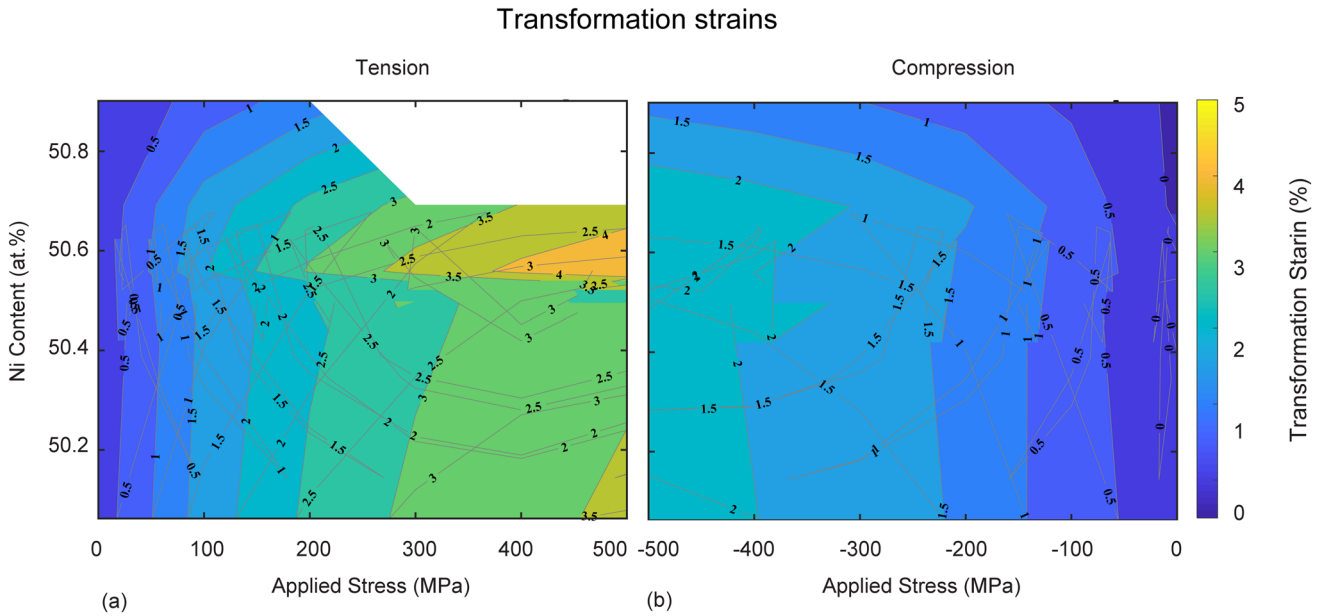

Fig. 50 Effect of adjusted composition and applied stress on the transformation strains for alloys aged at 550 °C for 3 h and air cooled, tested in **a** tension and **b** compression

the drop in the onset stress, the slope of the stress-induced martensite plateau of the first loading cycle decreases with increasing Ni content, and since no re-hardening behavior is seen before the 3% limit, the maximum stress reached at 3% strain also decreases with the addition of Ni. Finally, the unloaded strains (Fig. 46f), also an indication of the residual strains, are highest for the Ti-rich or Ni-lean compositions, due to the lack of precipitation strengthening and the early onset of plastic deformation. The unloaded strains decrease asymptotically to zero with increasing Ni content.

Finally, the thermomechanical responses as measured from the UCFTC tests shown in Figs. 30, 31 are summarized in 3D contour maps where the x-axis represents the applied stress, the y-axis represents the adjusted Ni content, and the

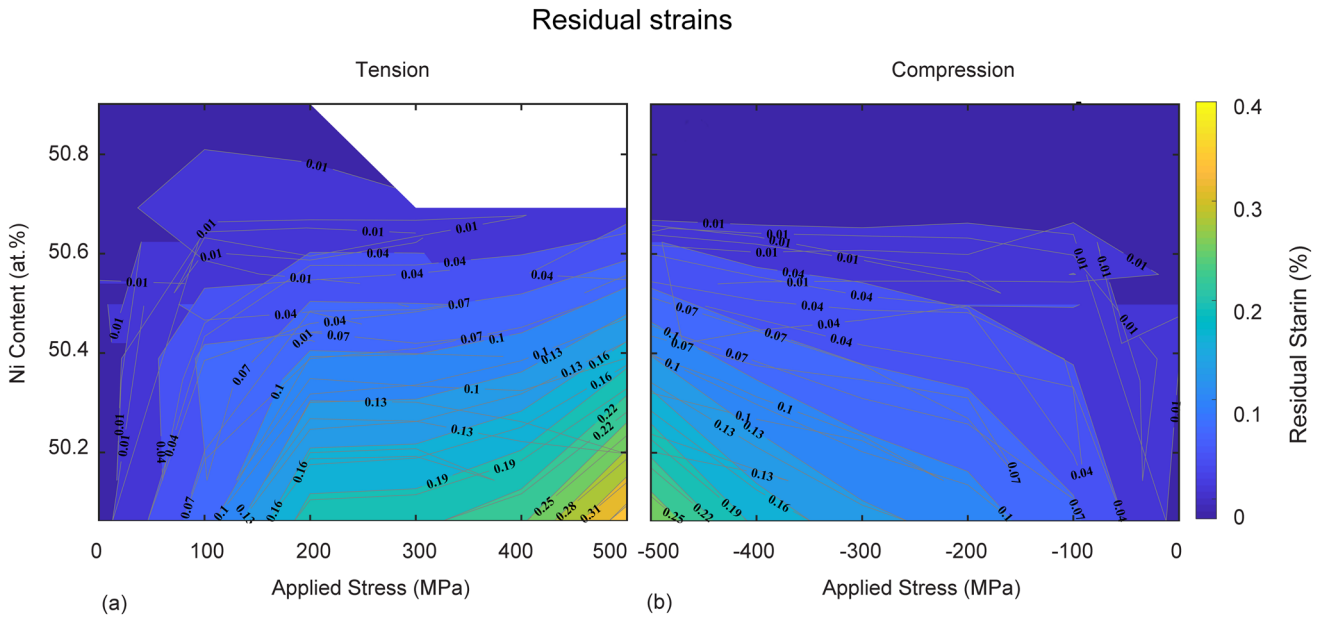

Fig. 51 Effect of adjusted composition and applied stress on the residual strains for alloys aged at 550 °C for 3 h and air cooled, tested in **a** tension and **b** compression

contours represent the data pertinent to transformation temperatures in tension (Fig. 47), transformation temperatures in compression (Fig. 48), thermal hysteresis (Fig. 49), transformation strains (Fig. 50), and residual strains (Fig. 51). These maps are very helpful and can be used to quickly select an alloy with the desired properties for a given application. Transformation temperatures, as expected, showed a gradual decrease with added Ni and an increase with added stress. The effect of stress on the temperatures was more pronounced in tension (Fig. 47) compared to compression (Fig. 48) as can be observed by following the contour lines and colors. These contour maps also indicate the range of temperatures that can be obtained within the Ni content shown. Hysteresis (Fig. 49) does not follow a linear trend but rather exhibits a minima around a Ni content of 50.5–50.7 at.% with values around 25 °C (under load).

Similarly, transformation strains (Fig. 50) do not behave monotonically but show maxima at around 50.6 at.% with a magnitude of ~ 4% in tension and ~ 2.5% in compression. The same is true for the residual strains (Fig. 51), where the compositions at and above 50.6 at.% Ni content show the best dimensional stability.

Concluding Remarks

Successful processing and scale up of a polycrystalline Ni–Ti-20Hf (at.%) high-temperature shape memory alloy was demonstrated in this work. Correlations between processing, chemistry, microstructures, and the ensuing thermomechanical responses were elucidated.

- Alloys were produced using melting techniques consisting of vacuum induction melting (VIM), vacuum induction skull melting (VISM), and combinations of vacuum arc remelting (VAR) with either VIM, VISM, or plasma arc melting (PAM). Moreover, five different melt shops were used to assess the variability from lot to lot, with repeats yielding 18 distinct heats.
- The NiTi-20Hf alloy was produced in heats from 0.4 to 250 kg, with the intent to demonstrate scalability from laboratory to industrial sizes and to substantiate commercial viability. The alloy was successfully produced in large quantities in collaboration with industrial partners following best practices described in this work.
- Hot working in this study was limited to extrusion, and the best-practice process parameters such as extrusion temperatures (900–950 °C), ram speeds, extrusion factors, and lubrication are highlighted.
- Chemistries, impurities, and inclusions were identified as a function of melting method. Chemistries measured using ICP were for the most part within experimental error of the target compositions, but variations in properties were observed, indicating discrepancies in the actual compositions. The variations can be associated with the melting techniques (e.g., elemental evaporation, reactions with crucibles, loss of elements to the skull, etc.). Although most alloys contained acceptable levels of impurities (based on NiTi standards), reduction of such

levels can be further improved by selecting the proper melting method and parameters. In general, inclusions were found to be HfC (e.g., in the VIM process), HfO_2 (e.g., in VISM and PAM processes), and $(TiHf)_4Ni_2O_x$ type oxides (e.g., in Ti-rich or stoichiometric formulations).

- Aging Ni-rich alloys at 550 °C for 3 h yielded a microstructure with finely distributed, nanometer-size H-phase precipitates in the range of 15–30 nm. This phase was characterized via X-ray diffraction and transmission electron microscopy to elucidate its features and clarify frequent ambiguities.
- Thermophysical properties of these alloys were presented, including density, thermal diffusivity, specific heat, thermal conductivity, thermal expansion, electrical resistivity, and melting point. Most of these measurements were performed during heating and cooling cycles, capturing the martensite region, the austenite region, and the dual phase region in between. These properties were for the most part independent of the processing technique used and insensitive to small deviations in composition, unlike the transformation dependent properties.
- Isothermal mechanical properties including elastic moduli, onset stresses, and residual strains were reported for the martensite and austenite phases. Recoverability and superelastic behavior were shown as a function of test temperature. In general, aged alloys fully recovered after loading to 1GPa in the martensite and exhibited at least 3% superelastic strains when tested above the austenite finish temperatures.
- Transformation properties were documented for all the aged alloys, including transformation temperatures, hysteresis, actuation strains, transformation strains, and residual strains. A range of activation temperatures (A_f) from 100 to 350 °C were obtained depending on actual composition. In optimal alloys, actuation strain exceeding 4% (in tension), with near-perfect dimensional stability was achieved.
- Compositional adjustments were applied to the Ni content by correcting the measured chemistries using the transformation temperatures of carefully melted and verified buttons. The adjusted values were used to produce property plots as a function of corrected Ni content that can be used as a guideline for design and alloy selection within the family of NiTi-20Hf alloys. However, from a functional standpoint, the optimum composition seems to be closer to $Ni_{50.5}Ti_{29.5}Hf_{20}$ than the original target of $Ni_{50.3}Ti_{29.7}Hf_{20}$ typically studied.

In conclusion, these results clearly demonstrate the viability of commercially producing large quantities (250 kg) of Ni–Ti-20Hf (at.%) with predictable compositions, thermophysical properties, thermomechanical properties, and transformation and actuation properties. In addition, each melting process described in this study can be used to produce acceptable NiTiHf shape memory alloys. The various processes have slightly different effects on the composition and impurity contents of the resulting alloy, but by tailoring the initial feedstock composition and purity, controlling melting parameters, and using good melting practices, the compositional variations and impurities can be minimized.

Acknowledgments Funding from the NASA Aeronautics Research Mission Directorate (ARMD) Transformational Tools and Technologies (TTT) project is gratefully acknowledged. The authors thank S. A. Padula II, T .J. Halsmer, D. A. Scheiman and D. F. Johnson for providing some experimental assistance; J. A. Buehler for metallography; T. J Ubienski and D. J. Brinkman for sample machining; and A. H. Veverka and G. E. Feichter for alloy fabrication. The authors also thank S. Reed from Flowserve Corporation for induction skull melting, and J. Slater and K. Fezi from Fort Wayne Metals for plasma melting and processing. The authors are also grateful to many organizations that contributed directly or indirectly to some aspects of this work. O. B. thanks A. Young (student intern from University of North Texas) for assistance with some data parsing.

References

1. Ma J, Karaman I, Noebe RD (2010) High temperature shape memory alloys. Int Mater Rev 55(5):257–315
2. Benafan O et al (2019) Recent advancements in rotary shape memory alloy actuators for aeronautics. Shape Mem Superelast 5(4):415–428
3. Calkins FT et al (2020) Shape memory alloy actuated vortex generators. Adv Mater Process 178(3):60–62
4. Karaca H et al (2014) NiTiHf-based shape memory alloys. Mater Sci Technol 30(13):1530–1544
5. Mavroidis C (2002) Development of advanced actuators using shape memory alloys and electrorheological fluids. Res Nondestr Eval 14(1):1–32
6. Angst DR, Thoma PE, Kao MY (1995) The effect of hafnium content on the transformation temperatures of $Ni_{49}Ti5_{1-x}Hf_x$. Shape memory alloys. J Phys 05(C8):747–752
7. Meng X et al (2000) Effect of aging on the phase transformation and mechanical behavior of $Ti_{36}Ni_{49}Hf_{15}$ high temperature shape memory alloy. Scr Mater 42(4):341–348
8. Meng XL et al (2003) Two-way shape memory effect induced by martensite deformation and stabilization of martensite in $Ti_{36}Ni_{49}Hf_{15}$ high temperature shape memory alloy. Mater Lett 57(26–27):4206–4211
9. Meng XL et al (2002) Stress-induced martensitic transformation behavior of a Ti-Ni-Hf high temperature shape memory alloy. Mater Lett 55(1–2):111–115
10. Meng X et al (2006) Effect of aging on martensitic transformation and microstructure in Ni-rich TiNiHf shape memory alloy. Scr Mater 54(9):1599–1604
11. Karaca H et al (2013) Effects of nanoprecipitation on the shape memory and material properties of an Ni-rich NiTiHf high temperature shape memory alloy. Acta Mater 61(19):7422–7431
12. Hornbuckle B et al (2015) Structure–property relationships in a precipitation strengthened Ni-29.7 Ti-20Hf (at%) shape memory alloy. Mater Sci Eng 637:63–69
13. Bigelow GS et al (2011) Load-biased shape-memory and superelastic properties of a precipitation strengthened high-temperature $Ni_{50.3}Ti_{29.7}Hf_{20}$ alloy. Scr. Mater. 64(8):725–728

14. Yang F et al (2013) Structure analysis of a precipitate phase in an Ni-rich high-temperature NiTiHf shape memory alloy. Acta Mater 61(9):3335–3346
15. Santamarta R et al (2013) TEM study of structural and microstructural characteristics of a precipitate phase in Ni-rich Ni–Ti–Hf and Ni–Ti–Zr shape memory alloys. Acta Mater 61(16):6191–6206
16. Han XD et al (1998) A new precipitate phase in a TiNiHf high temperature shape memory alloy. Acta Mater 46(1):273–281
17. Meng XL et al (2006) Phase transformation and precipitation in aged Ti–Ni–Hf high-temperature shape memory alloys. Mater Sci Eng 438–440:666–670
18. Saghaian SM et al (2015) Effects of aging on the shape memory behavior of Ni-rich $Ni_{50.3}Ti_{29.7}Hf_{20}$ single crystals. Acta Mater 87:128–141
19. Evirgen A et al (2018) H-Phase precipitation and martensitic transformation in Ni-rich Ni–Ti–Hf and Ni–Ti-Zr high-temperature shape memory alloys. Shape Mem Superelast 4(1):85–92
20. Evirgen A et al (2012) Effect of aging on the martensitic transformation characteristics of a Ni-rich NiTiHf high temperature shape memory alloy. Funct Mater Lett 5(04):1250038
21. Benafan O, Gaydosh DJ (2017) High temperature shape memory alloy $Ni_{50.3}Ti_{29.7}Hf_{20}$ torque tube actuators. Smart Mater Struct 26(9):095002
22. Benafan O, Gaydosh DJ (2018) Constant-torque thermal cycling and two-way shape memory effect in $Ni_{50.3}Ti_{29.7}Hf_{20}$ torque tubes. Smart Mater Struct 27(7):075035
23. Benafan O et al (2014) Mechanical and functional behavior of a Ni-rich $Ni_{50.3}Ti_{29.7}Hf_{20}$ high temperature shape memory alloy. Intermetallics 50:94–107
24. Benafan O, Noebe RD, Halsmer TJ (2016) Static rock splitters based on high temperature shape memory alloys for planetary explorations. Acta Astronaut 118:137–157
25. Moholt M, Benafan O (2017) Overview of the spanwise adaptive wing. NASA technical report, doc. ID#20170009544
26. Kraft FF, Gunasekera JS (2005) Conventional hot extrusion. ASM handbook. Metalworking 14:421–439
27. Lekston Z et al (2014) Microstructure, phase transformations, and properties of hot-extruded Ni-rich NiTi shape memory alloy. J Mater Eng Perform 23(7):2362–2367
28. Müller K (2001) Extrusion of nickel–titanium alloys Nitinol to hollow shapes. J Mater Process Technol 111(1–3):122–126
29. Lutterotti L et al (1997) Combined texture and structure analysis of deformed limestone from time-of-flight neutron diffraction spectra. J Appl Phys 81(2):594–600
30. ASTM E1409-13 (2013) Standard test method for determination of oxygen and nitrogen in titanium and titanium alloys by inert gas fusion. ASTM International, West Conshohocken
31. ASTM E1019-18 (2018) Standard test methods for determination of carbon, sulfur, nitrogen, and oxygen in steel, iron, nickel, and cobalt alloys by various combustion and inert gas fusion techniques. ASTM International, West Conshohocken
32. ASTM E1461-13 (2013) Standard test method for thermal diffusivity by the flash method. ASTM International, West Conshohocken
33. ASTM E1269 (2011) Standard test method for determining specific heat capacity by differential scanning calorimetry. ASTM International, West Conshohocken
34. ASTM B84-07 (2019) Standard test method for temperature-resistance constants of alloy wires for precision resistors. ASTM International, West Conshohocken
35. ASTM E228-11 (2011) Standard test method for linear thermal expansion of solid materials with a push-rod dilatometer. ASTM International, West Conshohocken
36. ASTM E3098-17 (2017) Standard test method for mechanical uniaxial pre-strain and thermal free recovery of shape memory alloys. ASTM International, West Conshohocken
37. ASTM E3097-17 (2017) Standard test method for mechanical uniaxial constant force thermal cycling of shape memory alloys. ASTM International, West Conshohocken
38. Xu L et al (2015) Production of nuclear grade zirconium: a review. J Nucl Mater 466:21–28
39. Olier P et al (1997) Effects of impurities content (oxygen, carbon, nitrogen) on microstructure and phase transformation temperatures of near equiatomic TiNi shape memory alloys. Le J de Phys IV 7(C5):143–148
40. Sczerzenie F, Vergani G, Belden C (2012) The measurement of total inclusion content in nickel-titanium alloys. J Mater Eng Perform 21(12):2578–2586
41. Noebe R et al (2006) Effect of thermomechanical processing on the microstructure, properties, and work behavior of a $Ti_{505}Ni_{295}Pt_{20}$ high-temperature shape memory alloy. In: Berg B, Mitchell MR, Proft J (eds) Proceedings of the international conference on shape memory and superelastic technologies, May 7–11, Pacific Grove, California, pp.409–426
42. Frenzel J, Neuking K, Eggeler G (2004) Induction melting of NiTi shape memory alloys: the influence of the commercial crucible graphite on alloy quality. Materialwiss Werkstofftech 35(5):352–358
43. Frenzel J et al (2004) High quality vacuum induction melting of small quantities of NiTi shape memory alloys in graphite crucibles. J Alloy Compd 385(1–2):214–223
44. Coda A et al (2012) Characterization of inclusions in VIM/VAR NiTi alloys. J Mater Eng Perform 21(12):2572–2577
45. Kai W-Y et al (2019) Formation mechanism of $Ni_2Ti_4O_x$ in NITI shape memory alloy. Materialia 5:100194
46. Benafan O et al (2012) Microstructural response during isothermal and isobaric loading of a precipitation-strengthened $Ni_{29.7}Ti_{20}Hf$ high-temperature shape memory alloy. Metal Mater Trans 43(12):4539–4552
47. Prasher M et al (2019) Correlative SANS and TEM investigation on precipitation kinetics of H-phase in $Ni_{50.3}Ti_{29.7}Hf_{20}$ high temperature shape memory alloy. J Alloys Compds 779:630–642
48. Coughlin DR (2013) Characterization of stoichiometric and aging effects on NiTiHf high temperature shape memory alloys. Dissertation, Ohio State University
49. Oliveira JP et al (2019) Laser welding of precipitation strengthened Ni-rich NiTiHf high temperature shape memory alloys: microstructure and mechanical properties. Mater Des 162:229–234
50. Pawley G (1981) Unit-cell refinement from powder diffraction scans. J Appl Crystallogr 14(6):357–361
51. Dietzel D et al (2002) Local and depth resolved photothermal characterization of NiTi shape memory alloys. In: Analytical sciences/supplements proceedings of 11th international conference of photoacoustic and photothermal phenomena. Japan Society for Analytical Chemistry, Tokyo
52. Tian QC, Wu JS (2000) Characteristic of specific heat capacity of NiTi alloy phases. Trans Nonferr Metals Soc China 10(6):737–740
53. Pataky GJ, Ertekin E, Sehitoglu H (2015) Elastocaloric cooling potential of NiTi, Ni_2FeGa, and CoNiAl. Acta Mater 96:420–427
54. Faulkner M, Amalraj J, Bhattacharyya A (2000) Experimental determination of thermal and electrical properties of Ni-Ti shape memory wires. Smart Mater Struct 9(5):632
55. Terada Y et al (1995) Thermal conductivity of B2-type aluminides and titanides. Intermetallics 3(5):347–355
56. Goff J (1964) Thermal conductivity, thermoelectric power, and the electrical resistivity of stoichiometric TiNi in the 3 to 300 K temperature range. J Appl Phys 35(10):2919–2927
57. Stanford MK (2012) Thermophysical properties of 60-nitinol for mechanical component applications, NASA/TM 2012-216056

58. Qiu S et al (2009) Measurement of the lattice plane strain and phase fraction evolution during heating and cooling in shape memory NiTi. Appl Phys Lett 95(14):141906
59. Monroe J et al (2016) Tailored thermal expansion alloys. Acta Mater 102:333–341
60. Gehring D, Karaman I (2020) Evolution of anisotropic and negative thermal expansion in rolled equiatomic nickel-titanium martensite. Scr Mater 186:142–146
61. Young A et al (2019) Microstructural and thermomechanical comparison of Ni-rich and Ni-lean NiTi-20 at.% Hf high temperature shape memory alloy wires. Shape Mem Superelast 5(4):397–406
62. Bigelow GS et al (2007) Correlation between mechanical behavior and actuator-type performance of Ni-Ti-Pd high-temperature shape memory alloys. In: Proceedings SPIE, Behavior and Mechanics of Multifunctional and Composite Materials, vol 65262B. https://doi.org/10.1117/12.715252
63. Benafan O et al (2013) Temperature-dependent behavior of a polycrystalline NiTi shape memory alloy around the transformation regime. Scr Mater 68(8):571–574
64. Wang Y et al (1999) The tensile behavior of $Ti_{36}Ni_{49}Hf_{15}$ high temperature shape memory alloy. Scr Mater 40(12):1327–1331
65. Young B et al (2019) Effect of temperature on the fracture Toughness of a NiTiHf high temperature shape memory alloy. Shape Mem Superelast 5(4):362–373
66. Qiu S et al (2011) On elastic moduli and elastic anisotropy in polycrystalline martensitic NiTi. Acta Mater 59(13):5055–5066
67. Bucsek AN, Paranjape HM, Stebner AP (2016) Myths and truths of nitinol mechanics: elasticity and tension–compression asymmetry. Shape Mem Superelast 2(3):264–271
68. Stebner AP et al (2013) Micromechanical quantification of elastic, twinning, and slip strain partitioning exhibited by polycrystalline, monoclinic nickel–titanium during large uniaxial deformations measured via in-situ neutron diffraction. J Mech Phys Solids 61(11):2302–2330
69. Singh N et al (2016) Effect of ternary additions to structural properties of NiTi alloys. Comput Mater Sci 112:347–355
70. Stebner A et al (2011) Neutron diffraction studies and multivariant simulations of shape memory alloys: empirical texture development–mechanical response relations of martensitic nickel–titanium. Acta Mater 59(7):2841–2849
71. Gao X et al (2011) Neutron diffraction studies and multivariant simulations of shape memory alloys: concurrent verification of texture development and mechanical response predictions. Acta Mater 59(15):5924–5937
72. Wollants P, De Bonte M, Roos J (1983) Comments of "the transformation free energy in ordered Fe_3Pt." Scr Metall 17(5):671–672
73. Benafan O, Bigelow GS, Wood L (2019) Ruggedness evaluation of ASTM international standard test methods for shape memory materials: E3097 standard test method for mechanical uniaxial constant force thermal cycling of shape memory alloys. NASA/TM 2019-220029
74. Bigelow G et al (2019) Effect of composition and applied stress on the transformation behavior in $Ni_XTi_{80-X}Zr_{20}$ shape memory alloys. Shape Mem Superelast 5(4):444–456
75. Hamilton RF et al (2004) Stress dependence of the hysteresis in single crystal NiTi alloys. Acta Mater 52(11):3383–3402
76. Padula S II et al (2012) Effect of upper-cycle temperature on the load-biased, strain-temperature response of NiTi. Metal Mater Trans A 43(12):4610–4621
77. Benafan O, Bigelow GS, Scheiman DA (2018) Transformation behavior in NiTi-20Hf shape memory alloys: transformation temperatures and hardness. Scr Mater 146:251–254
78. Prokoshkin S et al (2004) On the lattice parameters of phases in binary Ti–Ni shape memory alloys. Acta Mater 52(15):4479–4492
79. Sehitoglu H et al (2017) Superelasticity and shape memory behavior of NiTiHf alloys. Shape Mem Superelast 3(2):168–187
80. Tong Y, Shuitcev A, Zheng Y (2020) Recent development of TiNi-based shape memory alloys with high cycle stability and high transformation temperature. Adv Eng Mater 22:1900496. https://doi.org/10.1002/adem.201900496
81. Bucsek AN et al (2016) Composition, compatibility, and the functional performances of ternary NiTiX high-temperature shape memory alloys. Shape Mem Superelast 2(1):62–79
82. Prasher M et al (2020) Effect of Hf solute addition on the phase transformation behavior and hardness of a Ni-rich NiTi alloy. Mater Chem Phys 247:122890. https://doi.org/10.1016/j.matchemphys.2020.122890
83. Umale T et al (2019) The effects of wide range of compositional changes on the martensitic transformation characteristics of NiTiHf shape memory alloys. Scr Mater 161:78–83
84. Frenzel J et al (2010) Influence of Ni on martensitic phase transformations in NiTi shape memory alloys. Acta Mater 58(9):3444–3458
85. Duerig T, Pelton A (1994) Ti-Ni shape memory alloys. Mater Prop Handb 1:1035–1048
86. Stebner AP et al (2014) Transformation strains and temperatures of a nickel–titanium–hafnium high temperature shape memory alloy. Acta Mater 76:40–53